Arab American University
Faculty of Graduate Studies

MRI Assessment of Vestibulocochlear nerve disease Diagnosed by Videonystagmography (VNG), and Pure-Tone Audiometry (PTA) Tests

By
Mohammed Abdalghani

Supervisor

Dr. Samer Mohammad Abdel Qader Mhanna

Co-Supervisor

Assoc. Prof. Jonathan McNulty

This thesis was submitted in partial fulfillment of the requirements for the Master`s degree in computed tomography and MRI sciences

02/ 2024

I

Thesis Approval

"MRI Assessment of Vestibulocochlear nerve disease Diagnosed by Videonystagmography (VNG), and Pure-Tone Audiometry (PTA) Tests"

By:

Mohammad Abdul khalik Abul Fattah Abdul Ghani

This thesis was defended successfully on February 10, 2024 and approved by:

Committee members	Signature
1. Asst. Prof. Samer Mhanna: Supervisor	…….
2. Assoc. Prof. Jonathan McNulty: Co- Supervisor	…….
3. Assoc. Prof. Abed AlNasser Assi: Internal Examiner	
4. Assoc. Prof. Hussein ALMasri: External Examiner	

Declaration

I certify that this thesis submitted for the degree of the master is the result of my research, except where otherwise acknowledged, and that the thesis has not been submitted for a higher degree to any other university or institution.

Name: Mohammad Abdul khalik Abul Fattah Abdul Ghani

Signed: 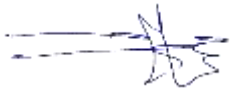

Student ID: 202112985

Date: 19.03.2024

DEDICATION

My dissertation is dedicated to my family and friends. Special thanks to my beloved wife, Fadwa, whose words of support and drive for persistence still sing in my ears. Shahd, Khalid, Tala, Hadeel, and Mutasem my children, have never left my side and are very dear to me.

I also dedicate my dissertation to my numerous friends and Palestinian Association of Medical Radiation Technologists family who have helped me along the way. I shall be eternally grateful to them all, especially Rami Khdour and Mohammed Taha for being by my side during all thesis progress.

I dedicate this work to and all colleagues in Palestine, and to all friends whom not mentioned here.

Acknowledgments

First and foremost, I would like to express my deepest appreciation to my thesis supervisor, Dr. Samer Muhanna for his support, patience, understanding and continuous guidance throughout my Master courses. I would also like to express my gratitude to my co – supervisor, Associate Professor Jonathan McNulty, who is a punctual and excellent scientist. He was always available for me despite his busy schedule. He was always there to support me, even in his busy times, he helped me make my thesis a success.

I have received a lot of support from Dr. Ahmad Abuarrah, Dr. Abdalnaser Assi, and other doctors and scientists, and I appreciate all of them for their support and efforts during my thesis progress.

I would like to express my gratitude to Dr. Taher Hannoun, Dr. Mamdouh Mahfouth, Dr. Issam Mujahed for giving me your valuable time in discussing the interpretation and diagnosis of patients' radiological exams , Dr. Shadi Shalabi for the feedback you gave me about the disease, to Mrs. Alaa Shalabi for taking many hours in explaining all about vestibular function tests she perform, and to all my colleagues who gave every help I asked during my most difficult time of working on the research data and statistical part of my dissertation.

Abstract

Aims and Objectives

The purpose of this study was to investigate the role and sensitivity of magnetic resonance imaging (MRI) in the diagnoses of the vestibular disorders, comparing the MRI to vestibular function tests including videonystagmography (VNG), and pure-tone audiometry (PTA) test, with positive results and reported as a vestibular disorder.

Addiitonally, to determine image quality of MRI sequences used by the two vendors by quantifying the image quality metrics (IQM), including signal-to-noise ratio (SNR) and contrast-to-noise ratio (CNR) and to make comparisons between the different sequences.

Methodology

The sample included 49 patients aged 7 - 77 years, 20 males and 29 females. Of the 49 patients who underwent an MRI exam, 32 had previously had vestibular function tests performed with positive findings.

Three radiologists reviewed the MRI examinations of the patients; in addition to recording the measurements of vestibulocochlear nerve (VCN) diameter. A statistical measure of mean, standard deviation, and range were calculated. Diagnostic reports from the three radiologists were assessed by intraclass correlation coefficient (ICC) for all data results.

The measurement of the vestibulocochlear nerve length was made on balanced fast field echo-150 slices (B_FFE_150 Slices) and fast imaging employing steady-state acquisition (FIESTA) on both sides from the axial images, and the two diameters measured on the sagittal reformatted image formed from the T2-weighted three-dimensional driven

equilibrium techniques (T2W_3D_DRIVE) or FIESTA sequence to calculate the cross sectional area (CSA).

Measurement of SNR was performed by the Difference Method for both in-vivo and phantom, whereas CNR was calculated by estimating the ratio of mean of signal to the SD of the background which represents the noise.

Radiologist Diagnostic Results

Radiologist's diagnostic reports showed the presence of pathology in 53.1% of all cases based on the MRI examinations. The results of the vestibular function tests showed a 58.8% with a central, and a 41.2% have a peripheral vestibular dysfunction. The mean values for VCN length were 19.02mm. The CSA mean for all patients, positive cases, negative instances were 1.50mm², 1.58mm², 1.43mm², respectively.

Result for SNR and CNR

In Phantom measurements of General Electric Healthcare (GE Healthcare) sequences, coronal-T1-FSE-Thin sequence has the highest value for SNR of 85.97 dB, and coronal T2-weighted fast spin-echo (Cor T2-FSE) has the highest CNR of 161.32 dB. Philips Healthcare a higher SNR value for T2-weighted fast field echo (T2-FFE), which is 162.97dB, and fluid attenuated inversion recovery –long repetition time (FLAIR-Long TR) has the highest CNR value, which is 27.59 dB.

In vivo, the study's findings suggest that when the three-dimensional fast imaging employing steady-state acquisition (3D-FIESTA) sequence was utilized for imaging, the GE Healthcare

MRI had the best signal-to-noise ratio (SNR), with an SNR value of 11.21 dB. The T2-weighted fast spin-echo (T2-FSE) sequence, on the other hand, generated the highest contrast-to-noise ratio (CNR) result, measuring 161.32 dB. With an SNR of 17.36 dB, Philips Healthcare MRI device produced the greatest SNR rating when using the T1-weighted fast field echo (T1-FFE) sequence, and fast imaging employing steady-state acquisition (FIESTA) recorded the highest CNR value of 322.26 dB.

Conclusion

The study suggests that parasagittal high resolution T2 weighted (DRIVE, constructive interference in steady state (CISS), and FIESTA) MRI can be used to measure the vestibulocochlear nerve, which is thicker in patients with positive MRI results. MRI is the preferred examination for recognizing vestibular nerve disorders, and most diagnosed disorders match central vestibular dysfunction on VNG test results. The study found that sequences with high SNR and CNR in Philips Healthcare and GE Healthcare MRI provided comparable image quality and excellent diagnostic capabilities. Understanding these sequences is crucial for assessing vestibular function test results and differentiating vestibular disorders. Videonystagmography (VNG) remains a crucial tool within the etiologic diagnosis of patients complaining of vertigo, even within the post-MRI period.

Sequences that have a high SNR and CNR in Philips Heathcare were TI –FFE and FIESTA respectively, but in GE MRI the better sequences for getting a high SNR and CNR were 3D FIESTA and T2-FSE respectively.

Table of Contents

List of Tables

List of Figures

List of Abbreviations

3D_FIESTA: Three-dimensional fast imaging employing steady-state acquisition

3DFSE: Three-dimensional fast spin echo

A\P: Anterior to posterior

ABR: Auditory brainstem response

ADC: Apparent diffusion coefficient

AICA: Anterior inferior cerebellar artery

AP: Anteroposterior

AX T2 FLAIR: Axial T2-weighted fluid attenuated inversion recovery

B_FFE_150 Slices: Balanced fast field echo-150 Slices

BERA: Brainstem evoked response audiometry

B-FFE: 3D balanced fast field echo

BFFE: Balanced fast field echo MRI sequences

CBCT: Cone-beam computed tomography

CISS: Constructive interference in steady state

CN: Cochlear nerves

CNR: Contrast-to-noise ratio

Cor T1 FSE (Thin): Coronal T1-weighted fast spin echo thin slices

Cor T2FSE (Thin): Coronal T2-weighted fast spin echo

CPA: Cerebellopontine angle

CSA: Cross-sectional area

CSF: Cerebrospinal fluid

CT: Computed tomography

dB HL: Hearing loss in decibels

DMAX: The maximum diameter

DMIN: Minimum diameter

DRIVE: Driven Equilibrium

DWI 2MM: Diffusion weighted imaging 2 mm

DWI b1000: Diffusion-weighted imaging at b value of1000

DWI: Diffusion weighted images

EAC: External auditory canal

ECoG: Elelectrocochleography

EH: Endolymphatic hydrops

ENG: Electronystagmography

ENT: An ear, nose, and throat doctor (ENT) specializes

ETL: Echo train length

FLAIR: Fluid Attenuated Inversion Recovery

FLAIR_LongTR: Fluid attenuated inversion recovery –long repetition time

FOV: Field of view

FSE or TSE: Fast or turbo spin echo

FSE: fast spin echo

GRE: Gradient echo

HASTE: Half-shot Fourier TSE

HIPAA Regulations: The Health Insurance Portability and Accountability Act

HSV I: Herpes simplex virus

Hz: Hertz (Hz)

IAA: Internal auditory artery

IAC: Internal auditory canal

IAM: Internal auditory meatus

ICC: Intraclass correlation coefficient

IP addresses: Internet protocol addresses

IQM: Image Quality Metrics

IR: Inversion recovery

ISO system: The International Organization for Standardization

kHz: Unit of frequency equal to 1,000 cycles per second

MD: Ménière's disease

MDCT: Multi-detector CT

MIP: Maximum intensity projection

MPR: Multiplanar reconstruction

MPRs: The multiplanar reconstructions

MR imaging: Magnetic resonance imaging

MRI: Magnetic resonance imaging

ms: Milliseconds

MSCT: Multislice computed tomography

MTC: Magnetization transfer contrast

NEMA: The National Electrical Manufacturers Association

NMV: Net magnetic vector

NSA: Number of signal averages

NSF: Nephrogenic systemic fibrosis

OKN: Optokinetic test

PD: Proton density

Post-gadolinium T1: T1-weighted post-gadolinium contrast media

PTA: Pure-tone audiometry

R\L: Right to left

RARE: Fast acquisition with relaxation enhancement sequence

RF: Radio frequency

ROI: Region of interest

S\I: Superior to inferior

SCDS: Semicircular canal dehiscence syndrome

SD: Standard deviation

SE or CSE: Conventional spin-echo pulse sequence

SNHL: Sensorineural hearing loss

SNR Diff: Difference method to determining SNR

SNR: Signal-to-noise ratio

SNR-STD: SNR- standard deviation

SROI: The signal in the original image

SS_TSE: Single-shot TSE

SSFP: Steady-state free precession MRI

STIR: Short tau inversion recovery

T1 WI: T1- weighted image

T1W: T1-weighted

T1W_FSE: T1-weighted fast spin echo

T1W_SE: T1-weighted spin echo

T2W: T2-weighted

T2W_3D_DRIVE: T2-weighted three-dimensional driven equilibrium techniques

T2W_FFE: T2-weighted fast field echo

T2W_TSE: T2-weighted fast spin-echo

TE: Echo time

THR: Hearing thresholds

TI time: Inversion time

TR: Repetition time

VCN: Vestibulocochlear nerve

Vi: Inferior vestibular

VN: Vestibular neuritis

VNG: Videonystagmography

Vs: Superior vestibular

Chapter 1. Introduction

Magnetic resonance imaging (MRI), is an excellent diagnostic modality for the soft tissue, and to a greater extent in case of the neuroimaging. Using MRI for assessment of the vestibulocochlear nerve(VCN), since the purpose of this study is to focus on the role of magnetic resonance imaging (MRI) in investigating vestibulocochlear nerve disorders and make a comparison with videonystagmography (VNG) and pure-tone audiometry (PTA) tests, which have positive results. The study targets patients who present with diplopia, hearing loss, tinnitus, hoarseness, headache, or otalgia and have confirmed diagnoses.

The main motivation of this work is to highlight the importance of MRI in the diagnosis and management of this kind of disorders in relation to the nervous system. Furthermore, a comparison of the results of the MRI exam for the vestibulocochlear nerve with the videonystagmography (VNG) test, which has positive results and is reported with a vestibular disorder. Also, several measurements of the vestibulocochlear nerve (VCN) were conducted to compare the length and cross-sectional area (CSA) of the VCN in positive (abnormal) and negative (normal) cases.

Objective:

The aim of the study is to investigate the role of magnetic resonance imaging (MRI) in the diagnoses of the vestibular disorders, comparing the MRI to VNG test results, and PTA test. In addition, determining image quality of the different MRI sequences used by the two vendors by quantifying the image quality metrics (IQM), including SNR and CNR and comparing between the different sequences.

Chapter 2. Literature Review and Background

2.1 Vestibulocochlear Nerve Anatomy

The temporal bone is a cranial bone that houses the petrous section of the inner ear's bony labyrinth, which includes the cochlea, vestibule, and semicircular canals (Figure 1). In addition to the bone labyrinth that is filled with fluid called perilymph, the inner ear possesses a membrane labyrinth (Khan & Chang, 2013).

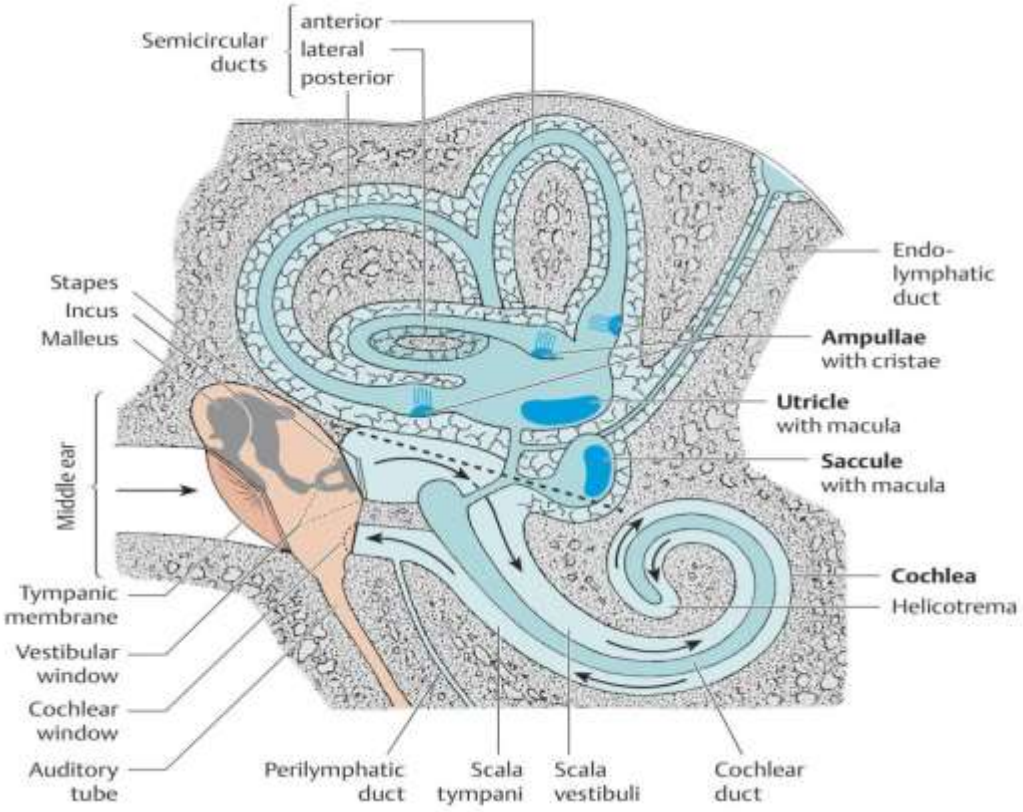

Figure 1. The hearing and balance organs of the vestibular system (Frotscher, 2005).

2.2 Vestibular Ganglion

Scarpa's ganglion, or the vestibular ganglion (Figure 2), is located in the internal auditory meatus (IAM) in the lateral portion and has two divisions, which are the inferior portion and superior portion, and is connected to each other by an isthmus. Scarpa's ganglion is composed of a large number of bipolar cell bodies that work as receivers for the afferent impulses that come from the hair cells of the crista ampullaris and the maculae. The uppermost part concludes with the crista ampullaris of the superior and lateral semicircular ducts, together with the macula of the utricle. The lower segment provides innervation to the macula of the saccule and the crista ampullaris of the posterior semicircular ducts (Khan & Chang, 2013).

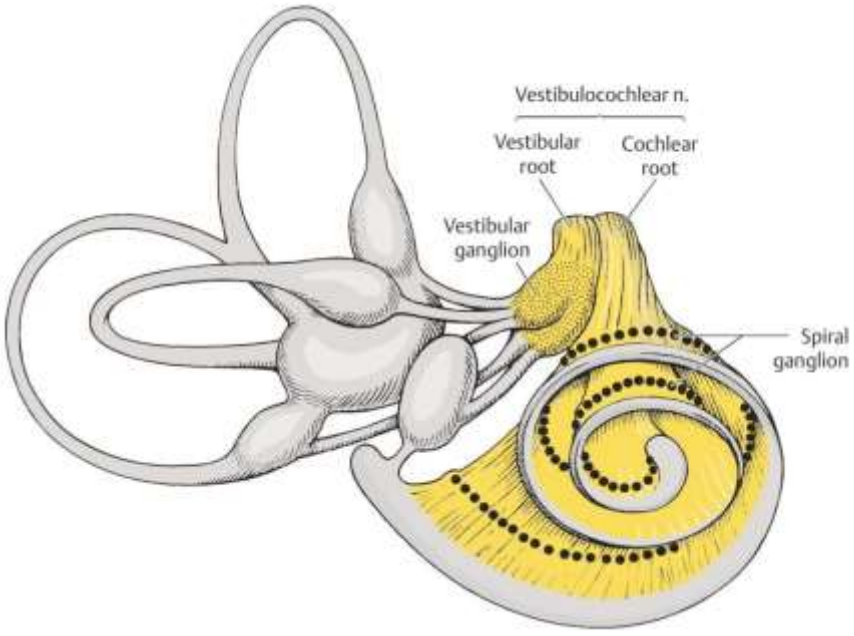

Figure 2. The vestibular ganglion (Frotscher, 2005).

2.3 Vestibular Nerve

The vestibular nerve is formed by the union of the axons of the superior and inferior divisions of the vestibular ganglion, and it subsequently joins the cochlear nerve to form the vestibulocochlear nerve (Figure 3). In the petrous portion of the temporal bone, the internal auditory canal (IAC) serves as a pathway for the vestibulocochlear nerve, facial nerve, nervus intermedius, and labyrinth artery (Khan & Chang, 2013).

The nerve fibers traverse the cerebellopontine angle before entering the brainstem at the pontomedullary junction. Additionally, at this point, the vestibular nerve separates from the cochlear nerve. The ipsilateral vestibular nuclear complex in the pons receives the vast majority of the afferent vestibular fibers. The vermian cortex and the cerebellum's flocculo-nodular lobe are the targets of some of the nerve fibers (Khan & Chang, 2013) .

From the brainstem to the IAC, the facial and vestibulocochlear nerves run together. Acoustic schwannoma may cause a displacement in the direction of the facial nerve (Kim et al., 1998)

.

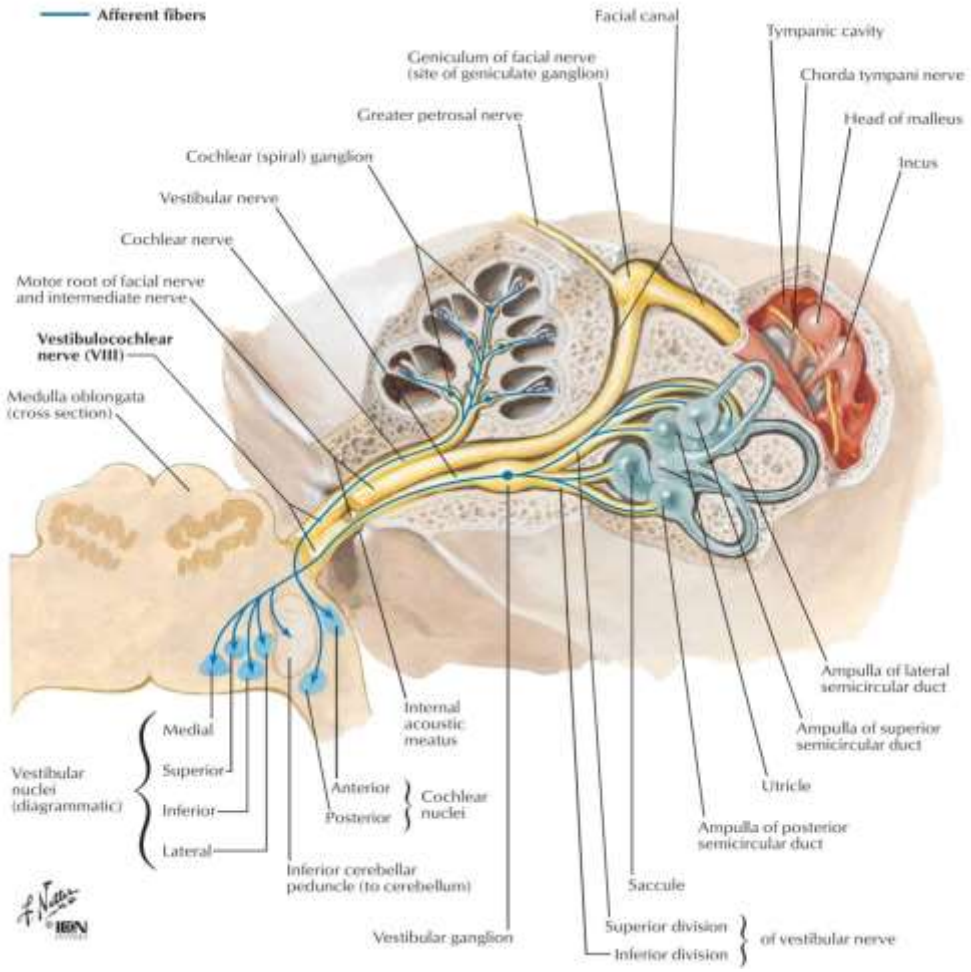

Figure 3. The vestibulocochlear nerve (Netter, 2002).

Both the subconscious balance control system, which connects to the cerebellum, and the conscious balance control system, which begins in the brain and passes through the corpus striatum and thalamus, are linked to the vestibular pathways of the sophisticated and multisensory reflex systems (Benoudiba et al., 2013).

The sensory maculae of the utricle and saccule, as well as the ampullary crest of the ampulla of the three semicircular canals, make up the membranous labyrinth,

which is home to ciliated sensory cells that generate afferent vestibular neuronal signals (Figure 4). The fluid inertia of the endolymph will stimulate the ciliated cells when the head moves linearly (vertically for the utricle and horizontally for the saccule) or during rotatory motion (ampullary crest) (Benoudiba et al., 2013).

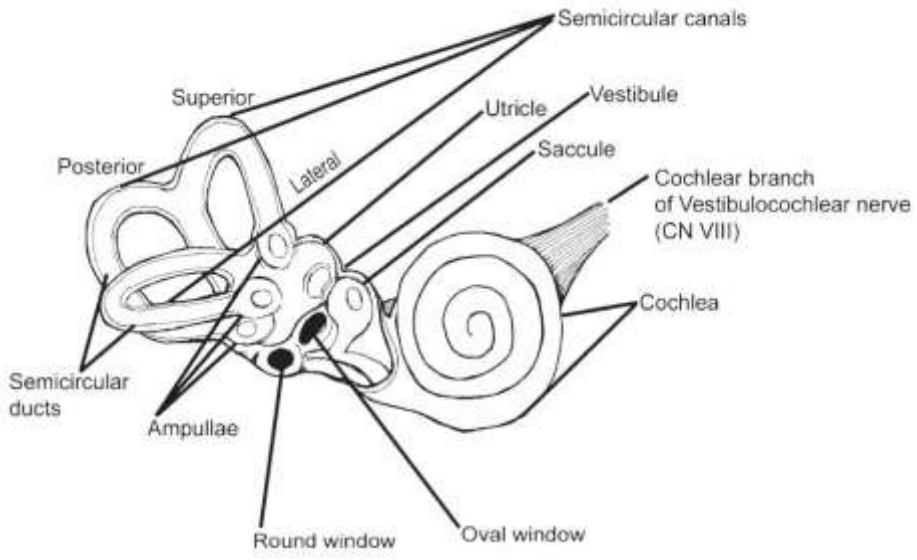

Figure 4. Bony and a membranous labyrinth of the inner ear (Frotscher, 2005).

The vestibular nerve is the result of the fusion of the superior vestibular nerve and the inferior vestibular nerve in the vestibular ganglion. The fibers meet in the rhomboid fossa of the brain stem, connecting the four vestibular nuclei (the superior Bechterew nucleus, the medial, lateral Deiters nucleus, and the inferior). There are four nuclei that receive signals from the vestibular system; these are where the ampullary fibers, saccular fibers, and utricle fibers all terminate (Benoudiba et al., 2013).

Perception of sound through the ear. Many mechanisms, such as speech and singing, cause vibrations in the air, which are referred to as sound waves. These waves or vibrations travel

to the eardrum via the external auditory canal (EAC). The tympanum (tympanic membrane) is what separates the middle ear from the external ear (Frotscher, 2005).

The middle ear is linked to the nasopharyngeal cavity by a tube called the eustachian tube. The vestibulum (the bone cavity in the middle ear) is coated with mucous membrane and filled with air. The foramen ovale and foramen rotundum are orifices in the middle ear's medial wall filled with perilymph. Receiving sound waves induce oscillations in the tympanic membrane, and the malleus, incus, and stapes (the three ossicles) transport the vibrations to the oval window, causing a vibration in the perilymph (Frotscher, 2005).

The inner ear is made up of bony and membrane elements. The vestibule and a bony tube lined with epithelium are located in the bony cochlea. The cochlear duct is made up of vestibuli, tympani, and medium, as well as the organ of Corti. The basilar membrane protects the Corti hair-and-cell spiral organ. The hearing organ receptors are hair cells that transform sound waves into electrical potentials. There are a total of 3,500 inner hair cells arranged in a single row, whereas there are between 12,000 and 19,000 external hair cells distributed across three or more rows. Stereocilia in 100 hair cells have been shown to trigger auditory receptor cells. Tonotopic basilar membrane frequencies rise at the bottom and fall at the top. Peripheral neurons receive input from inner hair cells, and core neurons in the spiral ganglion form the cochlear nerve (Frotscher, 2005).

The spiral ganglion cells give rise to the cochlear nerve, which travels from the IAM via the vestibular system to the brainstem via the cerebellopontine angle and the subarachnoid space. The cochlear nerve divides in two, with each branch traveling to either the ventral or dorsal cochlear nucleus, where the next relay (second neuron of the auditory pathway) is located.

The second neuron sends out impulses along core channels, some of which have additional synaptic relays (Frotscher, 2005).

To reach other relay stations, such as the superior olivary nucleus, the nucleus of the lateral lemniscus, or the reticular formation, some of the neurites from the ventral cochlear nucleus cross the midline within the trapezoid body and make a synapse with another neuron in the trapezoid body itself. The inferior colliculi carry a further synaptic relay onto the next neurons in the route, which in turn project to the medial geniculate bodies of the thalamus, where the acoustic signal was originally processed (Frotscher, 2005).

The major auditory areas of the cerebral cortex are located next to the auditory association areas, where new auditory stimuli are processed, recognized, and compared to previously stored auditory memories. The ability to recognize sounds or understand speech may be compromised if these cortical regions are injured (Frotscher, 2005).

Both the vestibular system and the auditory system receive nerve fibers from the VIIIth cranial nerve, also known as the vestibulocochlear nerve (Lanfermann et al., 2019). The nerve's afferent fibers leave the brainstem at the pons and enter the medulla oblongata at its lateral boundary through the internal acoustic aperture. About 25,000 individual nerve fibers make up the vestibular nerve's two vestibular branches, and their firing rate ranges from 10 to 100 spikes per second. Glutamate, of which there are three main forms (dimorphic, calyceal, and bouton), is the predominant excitatory neurotransmitter of vestibular afferents (McCaslin, 2019).

2.4 Vestibulocochlear Nerve Pathology

2.4.1 Disturbances of Hearing and Balance

Lesions affecting the vestibulocochlear nerve have the potential to adversely affect auditory function, balance, or both simultaneously. Sensorineural hearing loss is a condition that primarily affects the cochlear section of the auditory system, resulting in impaired hearing. On the other hand, vestibular lesions primarily manifest as symptoms of imbalance and vertigo. Two often encountered vestibular illnesses include vestibular neuritis and benign paroxysmal positioning vertigo. The vestibulocochlear nerve, often known as the eighth cranial nerve, is responsible for transmitting both auditory and vestibular information to the central nervous system. Auditory impulses are generated within the cochlear organ, whereas vestibular impulses start in the saccule and utricle, from where they propagate towards the vestibular nuclei (Mumenthaler et al., 2006).

2.4.2 Neurological Disturbances of Hearing

The otologist assumes the responsibility of diagnosing and treating conditions related to conductive hearing loss and disorders affecting the cochlea. The conductive hearing loss is a form of auditory impairment that arises when the root cause is situated within the middle ear or external auditory canal. In contrast, sensorineural hearing loss manifests in the sensory cells of the inner ear or the brain components responsible for auditory perception. Neurological disruptions affecting auditory function can manifest as either unilateral or bilateral impairments, with varying degrees of progression (Swartz, 2008).

Unilateral hearing loss typically arises from an infectious etiology, whereas bilateral hearing loss is predominantly associated with viral or other infectious causes. Tinnitus is a frequently reported symptom, characterized by subjective perception when only the patient can hear it, and objective perception when it can be detected by the examiner using a stethoscope. Pulsatile tinnitus is an infrequent auditory symptom that arises from the presence of a pulsating blood artery in close proximity to the petrous bone (Swartz, 2008).

2.4.3 Disequilibrium and Vertigo

Vertigo is caused by lost regulatory system information and control components or unexpected sensory input. Lesions in many sites produce vertigo. Non-directional vertigo is hard to characterize, while peripheral vestibular system lesions induce directional vertigo. Disruptions of the vestibular organ, vestibulocochlear n., and brainstem vestibular nuclei can cause vertigo and disequilibrium (Swartz, 2008).

Vestibular, optical, exteroceptive, proprioceptive, and performed motion nerve impulses go vern equilibrium. A distinction between vestibular and non-vestibular vertigo is based on a detailed clinical history, episodic or persistent symptoms, and triggering factors. Viral infection can produce acute vestibular vertigo, also called neuritis, neuropathy, or crisis. Sudden rotatory vertigo causes nausea, vomiting, and vestibular side-fall. The vestibular organ is less sensitive to caloric stimulation and heals in days. A trigger labyrinth may remain (Swartz, 2008).

Only particular head postures cause positional and directional vertigo, which are transitory attacks that dissipate fast. The most frequent type, benign paroxysmal positional vertigo

(BPPV), involves severe rotatory vertigo and nausea. Central positional vertigo is a rare head tilt-induced positional vertigo (Swartz, 2008).

The balance control system loses all vestibular input in bilateral damage, creating unsteady stride in the dark or on uneven or soft terrain. The inoperative vestibulo-ocular reflex causes oscillopsia, especially when walking (Swartz, 2008).

2.4.4 Non-Vestibular Vertigo

Vertigo may arise due to malfunctions in non-vestibular balance regulatory systems, visual-induced vertigo, compromised proprioception, cervical vertigo, pathological processes impacting central motor structures, partial impairment of consciousness, psychogenic vertigo, and general medical conditions that transiently reduce cerebral blood flow (Swartz, 2008).

2.4.5 Congenital Deformity of the Internal Auditory Canal

The vestibulocochlear nerve's growth determines the size of the internal auditory canal (IAC). A hypoplastic IAC with just the facial nerve is frequently the result of congenital vestibulocochlear nerve insufficiency. High-resolution MR imaging can show the vestibulocochlear nerve absence/hypoplasia and hypoplastic IACs, which are smaller than 2 mm in diameter.

Cochlear nerve deficit and IAC stenosis are related. Exostoses or osteomas may cause the IAC to narrow, which helps lessen the symptoms of hearing loss and vestibular dysfunction (Swartz, 2008).

2.4.6 Neoplastic and Pseudoneoplastic

The internal auditory canal and the cerebellopontine angle (CPA) are susceptible to cancerous diseases, and there are four types of cancer that are considered the most common:

1. The vestibular schwannoma (acoustic neuroma):

The most prevalent CPA tumor, making up between 60 and 90 percent of all CPA tumors and 6 to 10 percent of all intracranial tumors. They may be intracanalicular in form and occur more frequently in women since pregnancy speeds up the progression of malignancy. Extracanalicular nerve schwannomas can mimic meningiomas, metastases, and exophytic brainstem malignancies by involving only the CPA cistern (De Foer et al., 2010).

2. Meningiomas:

10% of intracranial masses, extra-axial neoplastic tumors caused by arachnoidal cap cells. They originate from the posterior petrous surface or the underside of the tentorium, making them the second most frequent CPA tumor. Due to their distance from the IAC porus and large base, meningiomas are distinct from acoustic tumors. Although a Dural tail is frequently an inflammatory reaction, it is not pathognomonic for meningioma (De Foer et al., 2010).

The most typical symptom of a CPA meningioma is sensorineural hearing loss, however the tumors themselves can be asymptomatic and are frequently found in middle-aged to elderly patients, particularly women. They are uncommon in young patients and are more likely to multiply. Meningiomas can develop in the internal auditory canal or labyrinth, making it challenging to distinguish them from schwannomas (De Foer et al., 2010).

3. Epidermoid tumors:

During the third to fifth weeks of development, as the neural tube closes, epidermoids, which are ectodermal inclusions, arise. Due to desquamation, they comprise approximately 2% to 1.8% of primary intracranial masses and expand slowly. Epidermoids have a propensity to adhere to the surface of the brain, surrounding healthy neuronal and circulatory systems, and can enlarge before showing symptoms. They represent the third most prevalent CPA/IAC mass overall (Strupp et al., 2020).

With 40% to 50% of cases, intracranial epidermoids are the most typical site for CPA/IAC mass. Despite the rarity of malignant transformation, MR imaging can show interior septations and lamellated features (Strupp et al., 2020).

4. Arachnoid cysts:

Arachnoid cysts are subarachnoid lesions characterized by the presence of CSF within a thin membrane wall. They lack connections to the ventricular system, are unilocular, smooth-margined, and expansive. The majority of arachnoid cysts (50-60%) are located in the middle cranial fossa, while only 10% are located in the posterior fossa of the skull. Epidermoid lesions are the hardest to tell apart from arachnoid cysts (Strupp et al., 2020).

2.4.7 Cholesteatoma

Cholesteatomas cause significant damage to the middle ear and adjacent structures and are one of the most invasive lesions. It leads to major complications, including intracranial infections and conductive and sensorineural hearing loss. MRI and CT scans are used to the diagnose of cholesteatoma (Benson et al., 2020).

2.4.8 Meningeal Metastases

Metastatic illness in the cerebellopontine angle region may manifest as a discrete mass located outside the brain parenchyma or as meningeal metastases accompanied by widespread dissemination of cancer cells in the cerebrospinal fluid. These neoplasms have the potential to affect both the pachymeninges and leptomeninges, and they may not exhibit any signs of inflammation. The leptomeningeal neoplasm can manifest as either diffuse or discrete and nodular forms. In cases of nodular illness, it is important to note that it can mimic a primary neoplasm. Metastatic melanoma exhibits a preference for the leptomeninges, and amelanotic tumors may exhibit similar characteristics to schwannoma, but they may seem hyperintense on precontrast T1WI (Strupp et al., 2020).

2.4.9 Lipoma and Mimics

Mal-differentiation of the primitive meninx can cause benign lesions known as CPA/IAC lipomas. Most veins and nerves in the CPA pass through the lesions, so they should not be operated on (Strupp et al., 2020).

2.4.10 Infectious-Inflammatory Pathology

The presence of leptomeninges in direct contact with the vestibularcochlear nerve (VCN) might result in the development of leptomeningeal illness within the internal auditory canal (IAC). Inflammatory diseases, such as meningitis and postmeningitic fibrosis, have the potential to impact the cerebellopontine angle (CPA) and internal auditory canal (IAC) (Strupp et al., 2020).

Sarcoidosis is a condition of unknown origin that manifests as thickening of the meninges and augmentation of nerves, including involvement of the vestibularcochlear nerve (VCN) either as a component of the disease or in isolation (Strupp et al., 2020).

2.4.11 Vascular Loops

Anterior inferior cerebellar artery (AICA) vascular loops are a potential source of auditory and vestibular complaints. Unilateral hearing loss is linked to exposure to AICA loops (Strupp et al., 2020).

2.4.12 Siderosis

Superficial siderosis is caused by recurrent subarachnoid hemorrhage, most commonly as a result of head trauma or vascular tumors, and results in hemosiderin deposition in the leptomeninges. Hemosiderin deposits are a leading cause of sensorineural hearing loss in VCN (Strupp et al., 2020).

2.4.13 Aneurysms

Aneurysms that are specifically located in the cerebellopontine angle (CPA) or internal auditory canal (IAC) region may originate from the anterior inferior cerebellar artery (AICA). These entities are infrequent and have the potential to be misconstrued as vestibular schwannoma. Patients may exhibit symptoms such as headache, specifically in cases of subarachnoid hemorrhage. Also, it is common for individuals whom also report symptoms associated with malfunctioning of the facial and vestibulocochlear nerves (Strupp et al., 2020).

2.4.14 Labyrinthitis

Labyrinthitis is a pathological condition characterized by inflammation in the perilymphatic regions of the inner ear, resulting in both sensorineural hearing impairment and vertigo. The condition may manifest unilaterally, bilaterally, or as a subsequent consequence of meningitis. Bilateral meningogenic labyrinthitis is a condition that manifests as inflammation in both inner ears, and it typically arises as a subsequent consequence of meningitis. The prevalence of this condition is the highest among pediatric populations and is a leading etiology of acquired hearing impairment in childhood. Labyrinthitis can manifest as a viral, autoimmune, bacterial, or luetic infection, potentially leading to the development of otosyphilis. The observed imaging findings encompass the augmentation of fluid-filled cavities inside the labyrinth (Strupp et al., 2020).

2.4.15 Vestibular Neuritis

Acute episodes of rotational vertigo, nausea, and unsteadiness when walking are common in diabetic individuals. Vestibular neuritis (VN), the third most frequent cause of vertigo associated with peripheral dysfunction, is a common presenting symptom in these patients. Herpes simplex virus (HSV I) infection of one or both vestibular nerve branches results in inflammation of the vestibular nerve, which in turn leads to VN (Strupp et al., 2020).

2.4.16 Ménière's Disease (MD)

Ménière's disease (MD) is a multifaceted condition affecting the inner ear, which is believed to arise from a mix of hereditary susceptibility and environmental factors.

Endolymphatic hydrops (EH) is commonly recognized as the underlying pathogenic mechanism for Ménière's disease, resulting in patients exhibiting either inadequate resorption or excessive production of endolymph (Lanfermann et al., 2019) .

2.4.17 Vestibular Migraine

An episode of vasoconstriction in the internal auditory artery (IAA). The artery in concern provides circulatory support for the auditory and vestibular organs, and an abrupt narrowing of the intracranial arterial arteries induced the postulated processes underlying migraines (Lanfermann et al., 2019).

2.4.18 Superior Canal Dehiscence

The inner ear ailment known as superior semicircular canal dehiscence syndrome (SCDS) causes vertigo and hearing loss. There are two fixed windows in the otic capsule organs for transmitting sound, and a third, movable window in some cases. Cholestasma, infection illness, physical trauma, and congenital abnormalities are all potential causes of dehiscence (Lanfermann et al., 2019).

2.5 Assessment of Vestibular Function

The vestibular lesion that affects the labyrinth or vestibular component of the VCN most frequently causes vertigo. Patients generally express systematic or directed dizziness, such as spinning or elevator-like sensations. Nonvestibular dizziness, which can result in giddiness, swaying, or darkness, is less well-defined. The objective symptom of a vestibular lesion is nystagmus, which is a rapid, rhythmic jerking movement of both eyes in the same direction. Nystagmus can occasionally be observed even when the patient looks straight. It might be horizontal, vertical, or rotatory (Mumenthaler et al., 2006).

When the patient stares straight ahead or just when the examiner directing the patient to looking to the side, nystagmus of vestibular origin might be noticed. The physiological end-gaze nystagmus and gaze-evoked nystagmus must be differentiated from it. When a patient stares completely to one side or the other, end-gaze nystagmus develops, and its rapid phase beats in the direction of gaze. It only qualifies as clinically significant if it persists following the maneuver (Mumenthaler et al., 2006).

2.5.1 Audiological Evaluation

Vestibular function testing includes pure tone audiometry (PTA) and auditory brainstem response (ABR) and electrocochleography (ECoG).

2.5.1.1 Pure tone audiometry

This method relies on the use of a pure tone with a frequency of 125, 250, 500, 1000, 2000, 4000, and 8000 Hz, respectively, and these frequencies are within the frequency range of natural human hearing, which ranges from 20 to 20,000 Hz. Where the patient refers to the weakest sound he\she hears (Shaabani, 2022). The result is a graph where the Cartesian system tests frequency in Hz. The horizontal axis represents the frequency (125-8000) in hertz units, and the vertical axis in the graph represents the intensity in dB HL (-10–120). The value of 120 represents the painful sensation and the uncomfortable level. The last intensity heard by the patient at each frequency is plotted, and these values depend on the patient's response in order to obtain an accurate diagnosis. In this examination, sounds are presented in both air and bone conduction (Shaabani, 2022).

The ISO system standardized threshold and color notation, where the red color was adopted for the right ear and the blue color for the left ear; a “circle” was adopted for the right ear and “X” for the left ear to indicate air conduction. and for bone conduction the sign “<” and “>” was used in the unmasked case and the sign “[“ and “]” in the masked case. Hearing thresholds (THR) standards have also been set for normal hearing, which are between -10 and +20 dB on all frequencies. Pure tone audiometry is used to diagnose Meniere's disease, which results from sensorineural hearing loss (Shaabani, 2022).

2.5.1.2 Brainstem evoked response audiometry (BERA)/auditory brainstem response (ABR)

This method is used to record neural activity in the auditory pathways that run from the cochlea to the brainstem (lateral lemniscus). Surface electrodes are used, and the click is used as an acoustic stimulus.
The click is a short (0.1 ms) rectangular stimulus used in this test that measures hearing sensitivity in the frequency range 1 to 4 kHz. When the stimulation is done with a high intensity of 70 to 90 dB in the first 10 ms, there are seven distinct waves that describe the response of the auditory pathway after the acoustic stimulus. These are the first and second waves that describe the proximal and distal auditory nerves, respectively. The third wave describes the cochlear nuclei. The fourth wave describes the superior olivar complex, the fifth wave describes the lateral lemniscus, and the sixth and seventh waves describe the medial geniculate body (thalamus) (Shaabani, 2022).
With a sensitivity of more than 90% and a specificity of about 70–90%, the ABR test provides important diagnostic information on response times, peak periods, and inter-ear differences (Shaabani, 2022).

2.5.2 Vestibulo-Ocular Reflex

2.5.2.1 Electronystagmography (ENG)/videonystagmography (VNG)

An examination that quantifies nystagmus as a specific sign—a defect in the ocular vestibular reflex resulting in vestibular asymmetry leading to nystagmus with a slow phase and a fast phase, the slow phase representing the effect of vestibular stimulation while the rapid phase representing the reflex movement of the eyes to return to their normal position in the orbit, and this phase shows the direction of nystagmus. If the rapid phase is descending, then this means nystagmus is striking to the left. But if the rapid phase is upward, then this means that it is a right beat nystagmus (Shaabani, 2022). Surface electrodes fixed around the eyes horizontally and vertically are used to measure the corneal-retinal potential, and the measurement depends on the direction of nystagmus and the speed of the slow phase (McCaslin, 2019).

The VNG examination includes a number of tests, like:

1. Spontaneous nystagmus: Fixation stability and the presence of spontaneous nystagmus should be monitored.

2. Static positional nystagmus: watch for nystagmus during or after changes in head posture.

3. Rotatory and caloric test: each ear was irrigated with a warm and a cool water so that the vestibular responses could be compared. Semicircular canal function can be tested by rotating the canal or by irrigating it with water/air, respectively (called caloric testing). Its quantitative information about the ear and its sensitivity to vestibular deficits make it important in balance clinics. Each of the horizontal semicircular canals can be evaluated with the help of the caloric test, which assesses caloric responses and fixation suppression.

4. Smooth Pursuit: is a test that involves watching the patient's eye movements while the target moves along a sinusoidal path in the horizontal plane.

5. Saccade: examine the velocity, accuracy, and latency of rapid eye movements from one target location to another.

6. Visual motility test: jerky nystagmus eye movements caused by repetitive objects moving across the subject's visual field and filling at least 80% of the visual field.

7. Hallpike responses: check for nystagmus after a quick change of position from sitting to the head hanging to the right or left.

8. Optokinetic test (OKN): response of eye movement to an optokinetic stimulation.

9. Positional test: records patient symptoms of vertigo and dizziness, as well as the effect of gravity and static body positions on peripheral vestibular system output, which may cause nystagmus.

10. Gaze test: the test aims to detect nystagmus and gaze holding during eccentric gaze, focusing on nystagmus with the head in midline, eyes at center, and horizontal and vertical gaze (Fife et al., 2000).

2.6 Vestibulocochlear Nerve Radiology

2.6.1 Computed Tomography (CT)

To evaluate some illnesses of the inner ear, it is better to combine CT imaging with magnetic resonance imaging. For example, to diagnose dysplasia, it is preferable to use computed tomography to evaluate the bony labyrinth, in addition to magnetic resonance imaging to evaluate the membranous labyrinth (Davidson, 2001).

Computed tomography is used in the diagnosis of temporal bone abnormalities associated with SNHL and the imaging of the auditory pathways that extend from the cochlea to the central pathways in the brainstem. It is also important for the diagnosis of pediatric patients and patients for whom MRI is contraindicated. Computed tomography is used in the evaluation of pathologies that cause SNHL and are most commonly located in the internal auditory canal (IAC), the cerebellopontine angle (CPA), and the membranous labyrinth (Davidson, 2001). A CT scan has a role in detecting bone changes that occur as a result of tumor growth, cancerous masses, and calcifications that appear in certain types of cancerous masses. This type of imaging is also essential in the evaluation of temporal bone trauma (Davidson, 2001).

The developments that took place in the field of computed tomography increased its ability to become an important diagnostic tool for adults and children alike, as multi-detector CT (MDCT) techniques have an accuracy of 0.1 mm in the ability to identify bone tissue, and cone-beam computed tomography (CBCT) technology allows imaging of the temporal bone and reduces exposure to ionizing radiation (Pyykkö et al., 2019).

The development of MDCT technology in the field of number of detector rows, to become for example, 32 detector rows increased its ability to depict normal anatomy and pathological conditions in the temporal bone, in addition to accurately imaging the anatomical structures of the inner and middle ears, because the development of scanners allowed obtaining isotropic voxels (Figure 5). It can be used in multi-level reconstructions of volumetric CT images (Pyykkö et al., 2019).

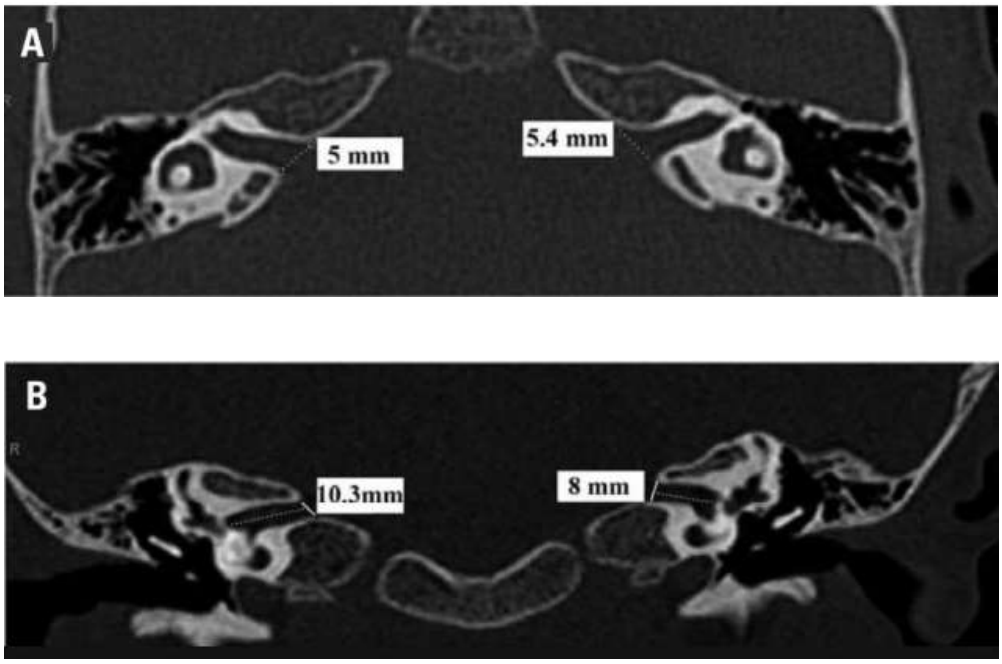

Figure 5. A. Axial multislice computed tomography (MSCT) slice of the temporal bones with normal IAC showing the anteroposterior diameter of the right and left canals; B. Coronal MSCT slice of the same temporal bones showing the length of the IAC of th e right and left canals (El Sadik & Shaaban, 2017).

High-resolution CT is utilized to assess IAC dimensions due of its high sensitivity (Pyykkö et al., 2019). After cochlear implants, CT is used to ensure correct placement and follow-up

of the patient (Pyykkö et al., 2019). The size of the bony canals can be measured, and inflammatory disorders and malignancies can be evaluated with CT scanning (Erkoç et al., 2012).

2.6.2 Magnetic Resonance Imaging (MRI)

MRI is used to identify lesions within the cranial vault, the IAC, and the labyrinth because it has superior tissue contrast, which is superior to soft tissue imaging over CT. MRI allows multiple imaging techniques that are used according to the disease to be diagnosed and the organ to be evaluated, such as CSF, bone, brain tissue, nerves, and blood vessels (Davidson, 2001).

To obtain excellent imaging of the cerebrospinal fluid (CSF) and nerves in the CPA and IAC, high-resolution FSE T2 imaging is preferred, which is a non-contrast technique. Three-dimensional fast spin echo (3DFSE) imaging will be clinically useful for displaying the inner ear, facial, and vestibulocochlear nerves (Nakashima et al., 2002), so it's used to detect meningiomas (Davidson, 2001).

MRI is used to look for vestibular-cochlear nerve diseases, especially in people who suffer from sensorineural hearing loss, vertigo, and tinnitus. To evaluate sensorineural hearing loss using MRI, three sequences are used: the T2-weighted submillimeter axial sequence, the fluid-attenuated or weighted axial reflection recovery (FLAIR) sequence, and the T1-weighted axial sequence (De Foer et al., 2010).

T2 thin-section MRI is utilized to examine the facial nerve and VCNs as they move laterally via the canal in the parasagittal planes to determine their connection and the cause of the disorder (Erkoç et al., 2012).

When examining the inner ear and predicting delicate tissue overgrowth such as vestibular schwannoma, vascular defects, endolymphatic hydrops, abnormalities of the cochlear aqueduct, or when a patient has sensorineural hearing loss, asymmetrical hearing loss, and vertigo, MRI is the technique of choice (Casselman et al., 1997), (Gheorghe et al., 2022). Despite the limitations of MRI in bone imaging because it is lacking of hydrogen atoms, it provides a descriptive view of soft tissues and fluid-filled sections. MRI has drawbacks, including a high cost, the need for anesthesia in children, and the inability to use it during surgeries like cochlear implants (Pyykkö et al., 2019).

2.7 MRI Imaging Contrast Weightings

2.7.1 T1-Weighting

Contrast in a T1-weighted image is created by changes in tissue T1 recovery times. TR influences contrast. The shorter the TR, the greater the exaggeration of variations in tissue T1 timings, which increases T1 weighting. T1 relaxation times for fats are short, but T1 relaxation times for water are long. As a result, when TR is short, fat regains the majority of its longitudinal magnetization while water loses substantially of its longitudinal magnetization. As a result, tissues with a high percentage of fat produce a strong signal and appear bright, whereas tissues with a high percentage of water produce a weak signal and appear dark. T1-weighted images are utilized to better show anatomy and to visualize

illnesses following contrast enhancement with specific materials (Westbrook & Talbot, 2018).

2.7.2 T2- Weighting

Contrast in a T2-weighted image is caused by changes in T2 decay times in tissues. When the TE is long, variations in T2 times between tissues are magnified. Because fats have short T2 decay durations and water has lengthy T2 decay times, fat loses much of its coherent transverse magnetization during the TE period, whereas water does not (Westbrook, 2016). As a result, tissues with a high percentage of fat seem dark, whereas tissues with a high percentage of water, such as CSF in the brain, appear bright (Toga, 2015).

The T2-weighted image is determined by the T2 decay times, which are determined by the strength of the magnetic field. To achieve good contrast with T2, the TE should be lengthy, and the TR should be extended to limit the effects of T1. T2-weighted images are utilized to demonstrate disorders such brain lesions (Westbrook & Talbot, 2018).

2.7.3 Proton Density (PD) Weighted Image

Differences in tissue proton density (the quantity of hydrogen protons in the tissue) cause contrast in the proton density-weighted image. This contrast can be produced by selecting a long TR and a short TE, which reduces the impacts of T1 and T2 (Westbrook & Talbot, 2018). Tissues that have a high proton density seem bright, whereas tissues that have a low proton density appear dark. In neuroradiology MRI, proton density-weighted imaging is not employed (Westbrook, 2016).

2.8 MRI Imaging Sequences

2.8.1 Spin-Echo Pulse Sequence

Pulse sequences are made up of a succession of radio frequency pulses with gradients and overlapping time intervals. Conventional spin-echo pulse sequence (SE or CSE) are the most often used MRI sequences for producing T1-, T2-, or proton intensity-weighted images. An excitation pulse with a 90-degree angle is employed first, followed by a rephasing pulse with a 180-degree angle, followed by an echo. The receiving coil receives and measures the echo signal (Westbrook & Talbot, 2018).

Fast or turbo spin echo (FSE or TSE) (fast acquisition with relaxation enhancement (RARE) sequence) is a pulse sequence that is much faster than conventional spin echo because it performs more than one phase encoding for each TR, and reducing scanning time by a factor equal to the turbo factor or ETL. Single-shot TSE (SS_TSE) or half-shot Fourier TSE (HASTE) are used to acquire images in a single breath (Westbrook & Talbot, 2018).

The DRIVE sequence gives a high signal intensity in water. In this sequence an additional pulse is given at the end of the TR period, which works to push any remaining magnetization in the transverse plane to the longitudinal plane. Since water has a long T2 decay period, tissues that contain a high percentage of water have magnetization. A residual cross at the end of each TR makes water the dominant signal in this sequence (Westbrook & Talbot, 2018).

A 180° inverted pulse is employed in the fast inversion recovery (IR) sequence to invert the NMV by 180° to full saturation. A 90° excitation pulse is applied at TI time, followed by

many 180° pulses to produce several phase-coded echoes with varying gradient slopes. Because many lines of K-space are filled at each TR, scanning time is reduced. Fast IR enables tests to be completed in a short period of time, in addition to the possibility of suppressing the signal from different tissue types (Westbrook, 2016).

STIR is an inversion recovery sequence in which a short TI, such as 100-180 ms, is used for fat signal suppression, with the TI value set to match to the time it takes for the fat vector to recover from full inversion to the transverse plane, with no corresponding longitudinal magnetization of the fat (Westbrook & Talbot, 2018).

FLAIR (Fluid Attenuated Inversion Recovery) employs the same method as the STIR sequence and is used to suppress the high signal of the CSF in T2-weighted images, where a TI ranging from 1700 to 2200 ms is used, which cancels the longitudinal magnetization in the CSF so that when the RF excitation pulse is given at an angle of 90 degrees, it will not create a transverse magnetization to give a signal, and this method allows the pathology adjacent to the CSF to be seen more clearly (Westbrook & Talbot, 2018).

2.8.2 Gradient Echo Sequence

Based on a frequency-coding gradient, a gradient echo sequence accelerates the magnetic moments of fast cycles while decelerating slow cycles. A pulse with a negative gradient eliminates the magnetic moments of rotation. .As a result of the T2* effects, such as increased noise and magnetic susceptibility, T2-weighted gradient echo images are referred to as T2*-weighted images (Westbrook & Talbot, 2018).

In addition to a tiny flip angle and a TR long enough to prevent saturation, a lengthy TE is utilized to allow maximal dephasing before the signal is created, resulting in maximum T2* effects (Westbrook, 2016).

The steady state sequence is generated by employing a repetition time (TR) that is shorter than the tissue relaxation times (T1 and T2). This enables the accumulation of transverse residual magnetization over a period of time. The steady-state acquisition sequence (balanced gradient echo) maintains longitudinal magnetization, and saturation is avoided by altering the phase angle of each RF excitation pulse at each TR (Westbrook, 2016).

By sensitizing motion with strong gradients, diffusion weighted images (DWI) are obtained. On either side of a 180° RF spin echo sequence, two equal gradients are delivered. Normal tissues with free random motion (high ADC) exhibit signal attenuation, whereas tissues with restricted diffusion (low ADC) exhibit strong signal. The amount of attenuation is determined by the amplitude and direction of the gradients (Westbrook & Talbot, 2018).

2.9 MR-Image Quality

A high resolution MRI procedure must be employed in order to identify the required structures and detect VSs within the canal and the labyrinth (Schulze et al., 2017). Therefore, signal-to-noise ratio (SNR), Contrast-to-noise ratio (CNR), and spatial resolution are important factors in imaging (Sakata et al., 2005) .

To demonstrate anatomy and pathology, MRI relies on a variety of different parameters that are chosen in the imaging console, called a protocol "set of rules" . The characteristics that the protocol aims to achieve in images are a high signal-to-noise ratio (SNR), a good contrast-

to-noise ratio (CNR), high spatial resolution, and a short scanning time (Westbrook & Talbot, 2018).

2.9.1 SNR

SNR is defined as the ratio between the amplitude of the received signal (the voltage induced in the receiving coil) and the average amplitude of the background noise (randomly placed frequencies in space and time). The signal is cumulative and predictable since it happens at or near the Larmor frequency and at or near time TE, while the noise is sporadic in time and space and occurs at all frequencies. The goal of increasing SNR is to increase the signal contribution relative to the noise contribution. The magnetic field strength, coil type and position, TR, TE, flip angle, Number of signal averages (NSA), receive bandwidth, and voxel size are all adapted to improve SNR (Westbrook & Talbot, 2018).

2.9.2 CNR

The CNR is the difference in the SNR ratio between two nearby locations, and it determines the eye's ability to differentiate between areas with strong and low signal. The same factors that affect SNR also control image contrast, and it is possible to increase it by doing the following: using T2 weighting, which has a high signal due to the use of a long TE that makes it able to differentiate between pathology and normal tissue; administration of contrast agents; magnetization transfer contrast (MTC); flow-related techniques that produce a signal only from nuclei with certain characteristics have a good CNR to distinguish these nuclei from others (Westbrook & Talbot, 2018).

2.9.3 Spatial Resolution

The spatial resolution is based on the voxel size, with high resolution being achieved by small voxels and low resolution by big voxels due to partial voluming. The size of a voxel can be modified by changing the slice thickness, field of view, or image matrix number. The spatial resolution improves with thinner slices and degrades with thicker ones. The SNR drops off significantly as voxels getting smaller (Westbrook & Talbot, 2018).

2.9.4 Scan Time

The length of time needed to finish data acquisition or fill k-space is known as the scan time, and it is influenced by variables in the scan protocol. It is proportional to the TR, the phase matrix, and the NSA. Optimizing scan timings is essential because extended scan times raise the risk of patient movement, which can cause image degradation (Westbrook & Talbot, 2018).

2.10 VCN MR-Imaging Techniques

To evaluate the temporal bone and parenchymal structures of the posterior fossa and CSF cisterns, standard MRI techniques are used that include multiplanar thin section T1-weighted images (T1 WI) without and with contrast enhancement,T2 fast spin echo (FSE) sequences, and T2 FSE high resolution which depends on the contrast of the intrinsic fluid-filled tissue in the membranous labyrinth and the IAC to diagnose the inner ear and the IAC (Davidson, 2001).An imaging procedure that includes the following sequences is used to evaluate sensorineural hearing loss (SNHL):

FLAIR whole-brain sequence to look for probable central cerebral or brainstem disease. Heavy-weight T2, which consists of a TSE-T2 sequence, a 3D FSE-T2 sequence, a driven equilibrium (DRIVE) sequence, and a fast imaging using steady state acquisition (FIESTA) sequence. In addition to assessing the intensity of the fluid signal in the membranous labyrinth, submillimeter axial sections also aid in the evaluation of the vestibulocochlear nerve and its branches (De Foer et al., 2010).

Axial thin slice (2mm or less) T1 weighted sequence using spin echo (SE) or TSE/FSE, or 3D gradient echo (GRE) T1 sequence (De Foer et al., 2010). Even though 3DFSE is effective for examining the inner ear as well as the facail and vestibulocochlear nerves, scanning takes a long time. As an alternative to the preceding sequence, 3DFRFSE uses a shorter TR and scans quickly. Because it offers high-resolution T2WI, this sequence is ideal for examining patients with lesions in the inner ear as well as the facail and vestibulocochlear nerves (Nakashima et al., 2002).

The imaging protocol should include T1-weighted sequences with and without enhancement, as well as FLAIR, diffusion-weighted, high-resolution T2-weighted (DRIVE, CISS, FIESTA) sequences on the IAM and anterior and posterior labyrinthine regions. This is done so that the numerous anatomical structures and brain nerve connections related to hearing and balance can be imaged (Benoudiba et al., 2013).

High-resolution T2 can obtain contrast in fluid and nerves without the use of gadolinium chelates, while contrast-enhanced T1 of the inner ear and CPA can assess hearing loss and neuritis. Gadolinium is injected, and multi-planar reconstruction is used to diagnose and

describe small lesions as well as look for small changes in the nerve morphology. However, T2 can only detect the disease if the surrounding water has changed the morphology of the tissues. T1-weighted sequences is the gold standard for diagnosing and monitoring vestibular schwannomas and meningiomas (Ciftci et al., 2004).

DRIVE (Philips Healthcare) is the same as 3DFRFSE (3D Rapid Recovery Fast Spin Echo, General Electric Medical Systems). DRIVE is a T2 contrast that decreases TR and lessens the impact of flow voids, and it increases the CSF signal compared to TSE without DRIVE. The inner ear and vestibulocochlear nerve are tested in this sequence. Loss of fluid-emitted signal due to flow voids, saturation, and magnetization transfer effects is the primary disadvantage of the heavy T2. While 3D TSE sequences can get around these problems, they need long scanning times. The cochlea, vestibule, semicircular canals, facial nerve, and vestibulocochlear nerve can all benefit from higher quality imaging via DRIVE (Ciftci et al., 2004).

High soft-tissue and spatial resolution is achieved with three-dimensional steady-state free precession sequences, despite the nerves' relative thinness (Dalaqua et al., 2021).

The evaluation of the cranial nerve's displacement and deformation, along with the accurate determination of the point of contact in reference to the root entrance zone, can be accomplished by the utilization of a restricted set of three-dimensional image reconstructions (Heine et al., 2002).

The conventional magnetic resonance imaging (MRI) technique commonly used for assessing head and neck malignancies typically involves both non-contrast and contrast-enhanced scanning. However, this approach has limitations in visualizing the peripheral branches of cranial nerves with sufficient clarity (Wu et al., 2020).

2.11 Radiological Anatomy and Relation Anatomy of VCN

The facial and vestibulocochlear nerves both originate from the lateral portion of the lower border of the pons and cross the cistern of the pontine angle at an oblique angle. They continue along the length of the internal auditory canal after passing through the internal auditory meatus, Figure 6 shows the relationship between these two nerves along their course (Sheth et al., 2009).

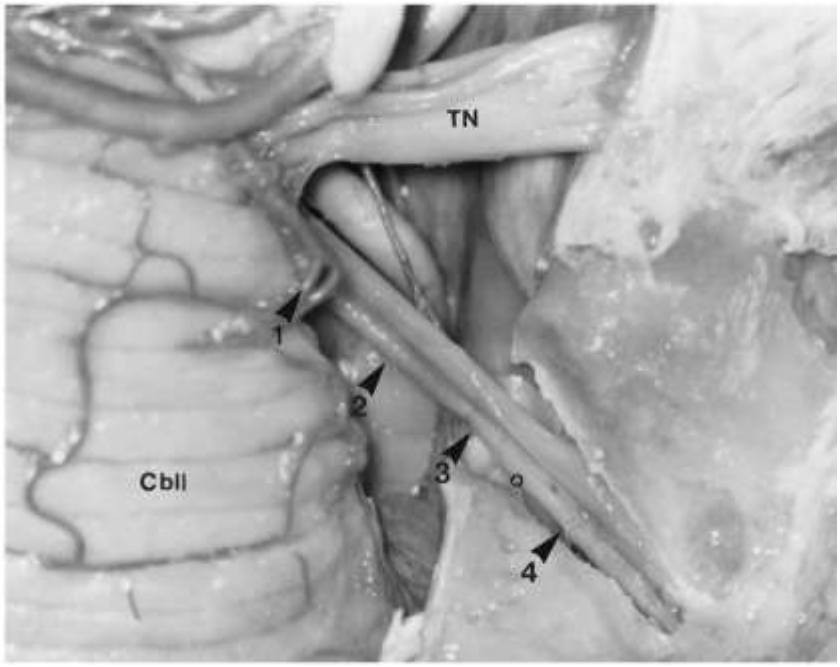

Figure 6. The relationship between the facial nerve and the vestibulocochlear nerve is at four levels: 1, the first level, which is near the brain stem; 2, the second level in the middle part between the brainstem and the porus acusticus. 3, the third level in the porus acusticus. and 4, the fourth level in the middle part of the IAC. Cbll, cerebellum; TN, trigeminal nerve (Kim et al., 1998).

After passing via the internal auditory canal, the facial nerve begins to travel over a difficult course inside the petrous bone before entering the facial canal via the fallopian canal and leaving the skull's base via the stylomastoid foramen. The cochlea, upper vestibular, and lower vestibular are separated from the vestibulocochlear nerve as it enters the internal auditory canal. There are four nerves visible inside the internal auditory canal at this level as a result of these branches passing next to the facial nerve there (Figure 8) (Kim et al., 1998). In order to identify cochlear nerve aplasia, magnetic resonance imaging is utilized to identify the nerves within the internal auditory canal using SSFP oblique sagittal images (Figure 7),

however, axial SSFP imaging allows only viewing two of the four nerves within the IAC (Sheth et al., 2009).

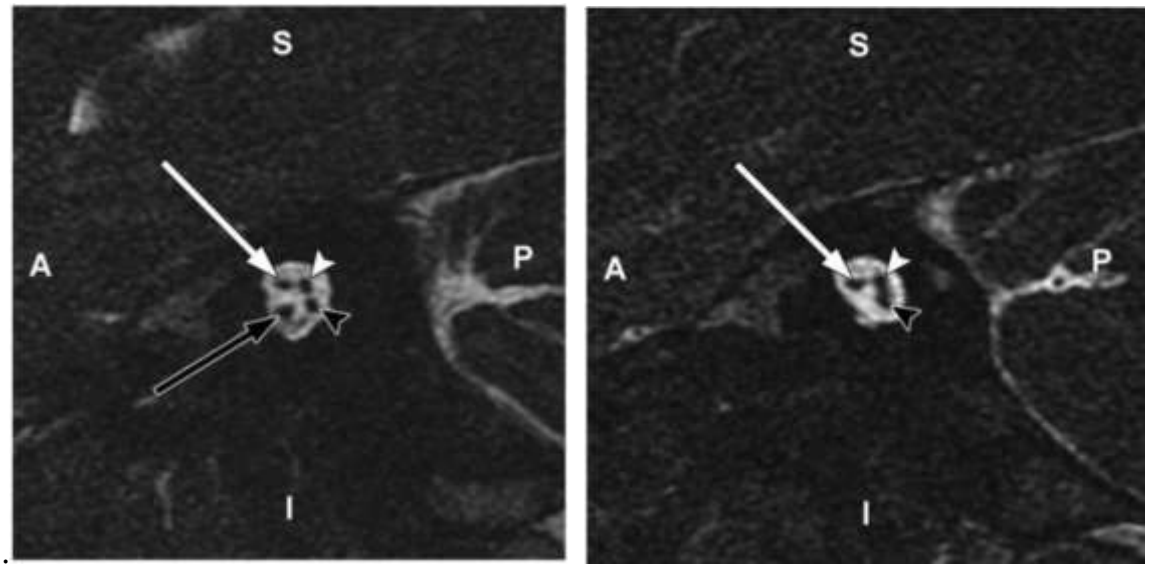

A B

Figure 7. Sagittal oblique SSFP cross-sectional MR images obtained in planes perpendicular to the left and right IAC. The left (A) and right (B) show the main branches of the facial and vestibulocochlear nerves in IAC. Directions are located using S, the superior aspect of the canal; I, the inferior aspect; A, the anterior aspect of the canal; and P, the posterior. In both A and B, the white arrow represents the facial nerve, the black arrow represents the cochlear nerve, the white arrowhead represents the superior vestibular, and the black arrowhead represents the inferior vestibular. In image B, the black arrow that represents the cochlear nerve is absent, and this means cochlear nerve aplasia disease (Sheth et al., 2009).

For those with normal hearing, the cross-sectional surface area of the facial nerve is 0.83 mm², and the cross-sectional surface area of the cochlear nerve is 1.07 mm² (Naguib et al., 2017).

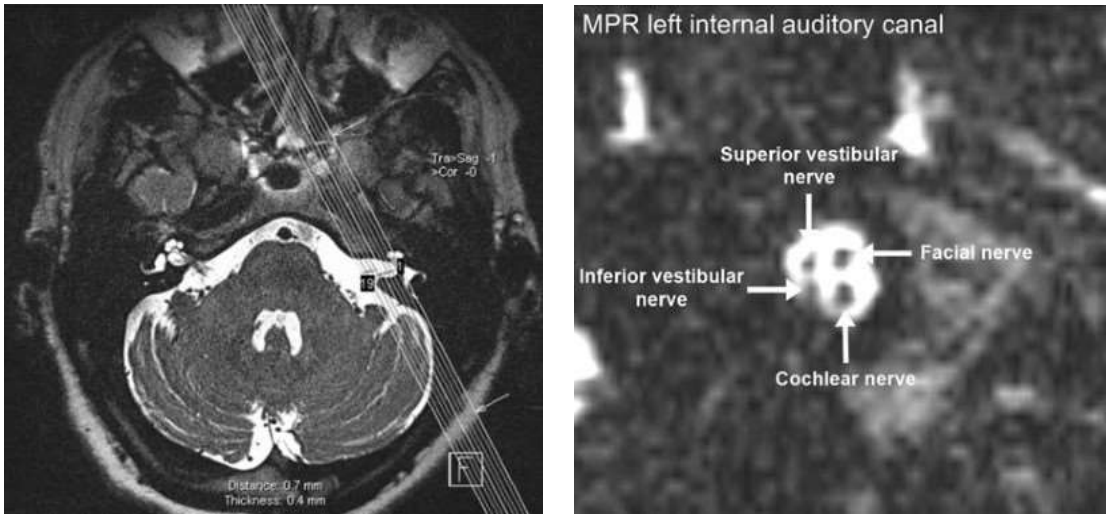

A B

Figure 8. Axial high-resolution T2 weighted MRI at the level of IAC. The left (A) show the orientation of the parasagittal multiplanar reconstruction (MPR) of the IAC and right (B) show the cochlear, facial, and superior and inferior vestibular nerves (Naguib et al., 2017).

Enlargement of the vestibulocochlear nerves may occur due to some diseases, like MD (Meniere's disease) (Henneberger et al., 2017). The canal's anterosuperior, anteroinferior, and posterosuperior portions are occupied by the facial nerve, cochlear nerve, and vestibular nerve, respectively. It is simple to identify between the two sections of the vestibular nerve (the superior and inferior nerves) because the lower vestibular nerve is smaller, rounder, or more oval than the upper vestibular nerve and has some fibers that connect to the cochlear

nerve. But in the lateral part of the IAC, these four nerves appear round in shape when an MRI images are the cross sections(Figure 9) (Kim et al., 1998).

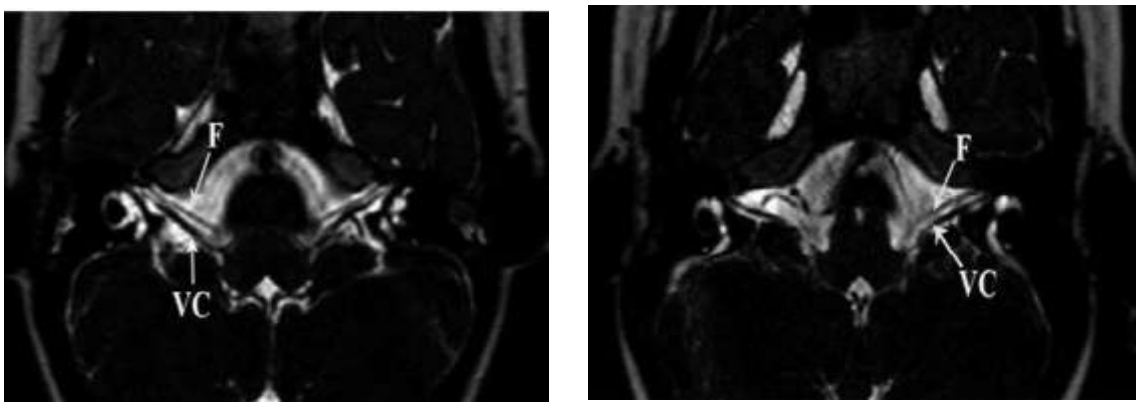

A B

Figure 9. Axial balance fast field echo (BFFE) T2- weighted images. The left (A) show the right side and right (B) show the left side, both images illustrate the relationship between facial nerve (F) and vestibulocochlear nerve (VC) (El Sadik & Shaaban, 2017).

The vestibulocochlear nerve runs in the posterior-inferior direction to the facial nerve (Figure 10), and as it emerges from the brainstem, it often appears rectangular or crescent-shaped. However, it is not completely divided into its four parts (superior, inferior, vestibular, and cochlear nerves) except in the most lateral portion of the IAC (Kim et al., 1998).

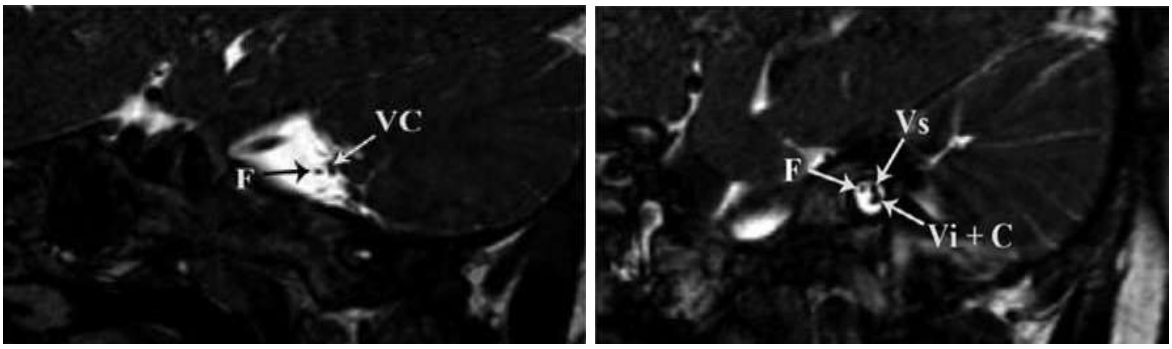

A B

Figure 10. Sagittal oblique BFFE T2-weighted section of the same temporal bone. The left (A) showing facial nerve (F) at the level of cerebellopontine angle, (B) showing (facial (F), superior vestibular (Vs), inferior vestibular (Vi), and cochlear (C) nerves) inside IAC (El Sadik & Shaaban, 2017).

Chapter 3. Materials and Methods

The Institutional Review Board of Arab American University in Palestine granted approval for this descriptive, retrospective, cross-sectional study. A Data Usage Agreement (DUA) was signed with tow health care providers in Tulkarm and Bethlehem cities for purposes of the "HIPAA Regulations" codified at Title 45 parts 160 through 164 of the United States Code of Federal Regulations, as amended from time to time. All patient records or MRI exams were previously deidentified and anonymized by the health care providers so that all the following personal information "Prohibited Identifiers" were removed: individuals' names, country of residence, zip codes, mailing addresses, phone or fax numbers, serial numbers, IP addresses, social security numbers, certification and licensing numbers, biometric identifiers, and full-face or comparable photographs (Simplification, 2006).

The sample included 49 patients aged 7 - 77 years, 20 male and 29 female. 32 out of 49 of these patients had undergone balance and vestibular function tests, 18 of them had a videonystagmography (VNG), 10 patients had pure tone auditory (PTA), and the 2 others had auditory brainstem response (ABR) , all results of the afore mentioned examinations were positive.

31 patients underwent MRI exam by a 1.5 Tesla Philips Healthcare scanner with the coil (16 Channel Sense NV Coil Manufacturer: Philips Modality: Closed MRI); the other 18 by a 1.5 Tesla GE Healthcare scanner with the coil (GE Signa MRI 16 CH Head Neck 16 Channel Coil Manufacturer: GE Modality: Closed MRI), Table 1 illustrate sample characteristics.

The total sample of the 49 patients included also 19 patients who underwent clinical examinations due to the presence of symptoms such as vertigo, headache, dizziness, imbalance, disorientation, blurred vision, and other symptoms that may be related to diseases of the eighth nerve, Table 2 lists the symptoms in the sample; headache was the most common.

Table 1: Sample characteristics.

Gender		Vestibular Function tests			MRI machine company	
Male	Female	VNG	PTA	ABR	Philips Healthcare	GE Healthcare
20	29	20	10	2	31	18

Table 2: Symptoms of a vestibular balance disorder.

Vertigo	SNHL	Headache	Dizziness	Blurred vision	Disorientation
30	18	38	28	12	28

All patients were transferred either by ENT medical center or by neurology medical center and were suspected to have vestibular disorders between 2020 and 2023. Of the 49 patients underwent the study, 18 patients with sensorineural hearing loss (SNHL).

The number of patients who had an IAC or CPA MRI on a 1.5T scanner (Philips Healthcare scanner) were 31 patients with the following sequences: B_FFE_150 Slices, DWI_og 2mm, FLAIR_LongTR, T1W_SE, T2W_3D_DRIVE, T2W_FFE, and T2W_TSE (Table 3).

Table 3: IAC protocol (Philips Medical Systems -Ingenia 1.5T MRI).

Parameters / Sequence	TR	TE	Slice Thickness	Slice Gab	FOV	Flip Angle	Phase	Matrix
T1W_SE	645	15	2	1	230	69	R|L	336
T2W_TSE	350 - 650	15	5 mm	1 mm	230	69	R|L	336
T2W_FFE	3000 - 5000	100	5 mm	1 mm	230	90	R|L	560
T2W_3D_DRIVE	1500	250	1.1 mm	-0.7	130	90	R|L	256
B_FFE_150 Slices	7.1	3.5	1.1 mm	0.5	160	60	R|L	380
DWI 2MM	1400-6000	74	2	0	230	90	AP	240
FLAIR_Long TR	6000	120	3	0.5	230	90	AP	256

Table 4: Mastoid protocol (GE MEDICAL SYSTEMS - Brivo MR355 1.5T MRI).

Parameters / Sequences	TR	TE	Slice Thickness	Slice Gab	FOV	Flip Angle	Phase	Matrix
T1W_FSE	502	17.18	3	3.3	24	160	R\L	320
STIR	3364	42	3.2	0.3	23	160	A\P	288
Apparent Diffusion Coefficient , ADC	5917	101.7	5	5.5	24	90	R\L	128
3D_FIESTA	7	250	0.6	1	20	65	A\P	320
DWI 2MM	7000	74	5	1	24	90	R\L	128
Cor T1 FSE (Thin)	466	15	2.5	0.3	18	160	S\I	288
AX T2 FLAIR	9000	140	5	0	24	160	A\P	320
Cor T2FSE (Thin)	3173	95	2.5	0.3	18	160	S\I	288

The other 18 patients have had mastoid MRI by a 1.5 GE scanner and the following sequences have been performed: 3D_FIESTA, Apparent Diffusion Coefficient (ADC), DWI 2MM, STIR, T1W_SE, and T2W_FSE (Table 4).

The measurement of the VCN length was made on B_FFE_150 Slices (FIESTA) in both sides was made on the axial image, and the two diameters was made on the sagittal reformatted image formed from the T2W_3D_DRIVE sequence in Philips and FIESTA in GE MRI images (Figures 28, 29). The widest diameter of the VCN in the internal acoustic canal was recorded.

In order to conduct VCN measurement, the three radiologists were intentionally kept blind of the clinical condition of the patients being evaluated. The images were then imported into the RADIANT software. In accordance with the previous study conducted by Naguib et al., all reconstructions were performed using either the isotropic T2W-3D-DRIVE sequence or 3D-FIESTA of the IAM. Subsequently, MPR was performed in the parasagittal orientation, which is perpendicular to the long axis of the internal auditory canal (also perpendicular to the long axis of the VCN). The display parameters, such as windowing or centreing, continued to be unchanged throughout the process, ensuring consistent and precise estimation in all patients. In the MPR images, the area of interest (ROI) was drawn along the perimeter of the VCN. Subsequently, the measurements were acquired, and the cross-sectional area of VCN was quantified in square millimeters (Naguib et al., 2017).

3.1 Methods of SNR Measurement

In this study, a methodology was used that relied on calculating the average signal value within a specific region of interest (ROI) in order to estimate the signal component, in order to know the amount of noise that may affect the diagnostic value of the MRI images, and

thus calculate the average of any irregularity in the image intensity. In order to judge the image quality of the MR scanning.

Many techniques have been documented in the academic literature for measuring signal-to-noise ratio (SNR) in MR imaging, so that these methods differ from each other in the way in which noise estimates are established.

For the calculation of the signal-to-noise ratio (SNR), the following approaches are the most, which could be used:

1. The single image signal-to-noise ratio (SNR) of the whole two times field of view (FOV) image may be determined by utilizing the mean of a background region as an estimate of the noise. Two separate estimations can be obtained, one from image A and another from image B.
2. The signal-to-noise ratio (SNR) of the whole image with a two times field of view (FOV) may be determined by calculating the standard deviation of a background region and using it as an estimate of the noise. This process yields two identical estimates, as described in the first scenario.
3. There are three distinct differences in the images. One possible estimate of the signal-to-noise ratio (SNR) for the whole two times field of view (FOV) image may be obtained by analyzing the data from the "A-B" region of interest.
4. Two full images are used, such as A and B, and the decimated images are taken A2, A1, B1, B2. Then the decimated images are used to calculate the SNR by testing the

correlation coefficient of the noise in a custom computerized way so that we can determine the average value of the background area as an estimate of the noise.

5. The standard deviation of the background area is used to evaluate and estimate the value of noise, so it is measured in the decimated image to express the SNR as a first estimate. The second estimate is the difference of images signal-to-noise ratio of the decimated image, which is calculated using two different methods. The preferred approach for measuring the signal-to-noise ratio (SNR) is denoted as "A1-A2" and "B1-B2".
6. The concept of "difference of unrelated images" refers to the comparison and contrast between two or more images that do not possess any inherent connection or similarity.
7. The signal-to-noise ratio (SNR) of the decimated image may be estimated using four different approaches: "A1–B1," "A1–B2," "A2–B1," and "A2–B2."
8. The National Electrical Manufacturers Association (NEMA) offers an alternative option. Similar to the third method, this approach utilizes the differences between adjacent pixels in a noisy image to mitigate potential problems such as drift and motion. It provides a single estimation (Steckner et al., 2009), (Reeder, 2007).

The SNR has been measured using a variety of techniques. They can be divided into approaches that use a single image, a pair of images, or a collection of numerous images. SNR calculations based on two ROIs in a single image (one in the tissue of interest and one elsewhere). in the background of the image , in air, or outside the object being imaged) can be divided into techniques using the background intensity's standard deviation (SD) and techniques using the background intensity's mean value . These two methods for two regions

are referred to as SNR-STD and SNR-Mean, respectively. Both, with the appropriate conversion factors gleaned from noise statistics.

Approaches produce the same outcomes. The "difference method," which is based on the assessment of a difference image of two repeated (identical) acquisitions, is a different approach to determining SNR; this method is known as SNR Diff.

3.1.1 Difference Method

Price et al. (1990) and Fairbank et al. (1999) explained that this method can be applied using only two images without the need for a large number of images. This methodology involves obtaining an estimate of the average signal by analyzing a limited region of interest (ROI) within the merged images. In addition, noise is obtained by determining the standard deviation of image differences from the same ROI.

The estimation process involves calculating the difference between two image sizes in an area characterized by a high signal, and this estimation process preserves the Gaussian noise statistics.

Reeder et al. (2005) gave a method for calculating the local SNR within a ROI in two images, S1 and S2. Specifically, the SNR is determined by dividing the signal in the original image (SROI), by half the average signal obtained from the ROI in the sum image as in equation (1).

$$\mathrm{SNR}_{\mathrm{ROI}} = \frac{S_{\mathrm{ROI}}}{\sigma_{\mathrm{ROI}}} = \frac{\mathrm{mean}(\mathbf{S}_1+\mathbf{S}_2)|_{\mathrm{ROI}}}{\sqrt{2}\,\mathrm{std}(\mathbf{S}_1-\mathbf{S}_2)|_{\mathrm{ROI}}} \qquad (1)$$

The equation S1+S2 represents the mean of the ROI in the original image, whereas S1-S2 represents the mean of the ROI in the difference image. Additionally, the standard deviation of the noise in the original image corresponds to the standard deviation in the ROI of the difference image. The factor of two is derived from the observation that when two images are combined by addition or subtraction, the resulting signal's variance is equal to the total of the variances of the noise present in each image. It is worth noting that variance may be calculated as the square of the standard deviation. If the magnitude of noise fluctuations within the specified area is minimal, it becomes feasible to obtain a precise assessment of the SNR at a local level.

To calculate the SNR, we have used the plugin image calculator function in the freely image-processing program ImageJ 1.54f (Wayne Rasband and contributors. National Institutes of Health, USA. Java 1.8.0_322 (64-bit). 31 MB of 5773MB (<1%)), by which the two functions; subtraction and adding are used to achieve the target of our study (Reeder, 2007).

Example:

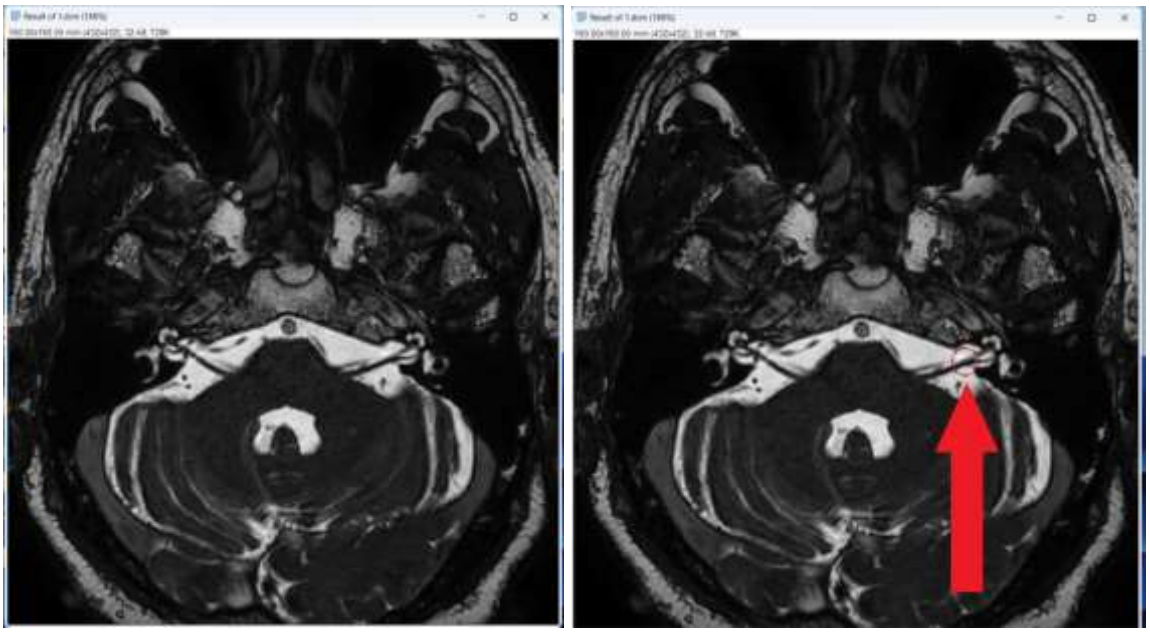

(A) (B)

Results

File Edit Font Results

	Area	Mean	StdDev	Median
1	43.347	2629.919	1262.083	3285.857

(C)

Figure 11. The left image (A) is an axial cross-sectional MR image created by adding two images by the ImageJ program. The right image (B) places the ROI marked with a red arrow on image A. (C) The table shows the results of intensity (mean) and noise (StdDev).

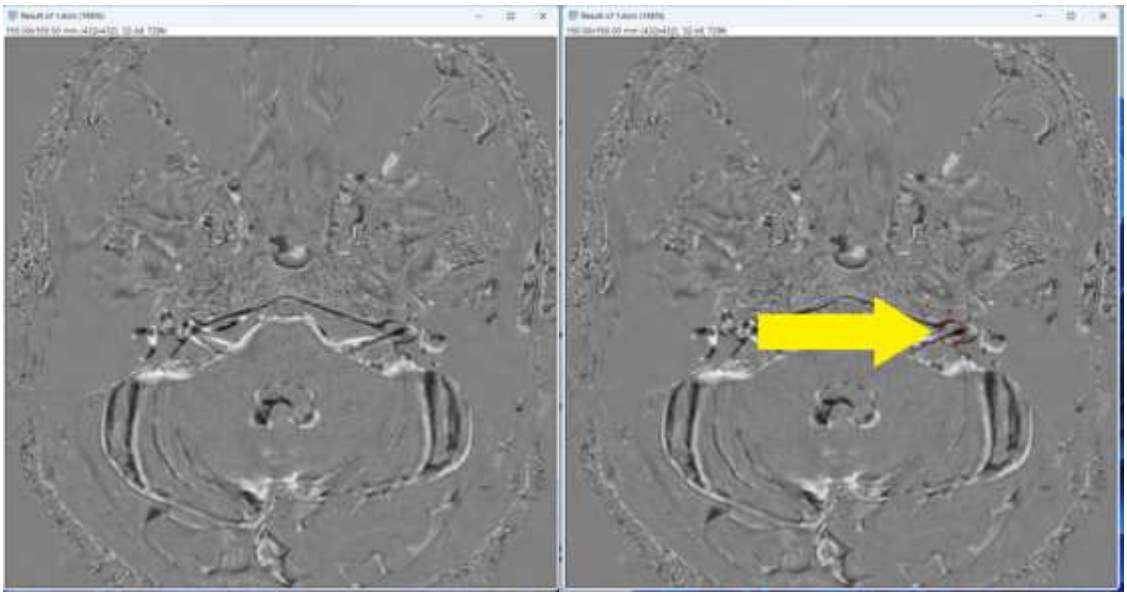

(A) (B)

Results

File Edit Font Results

	Area	Mean	StdDev	Median
1	43.347	2629.919	1262.083	3285.857
2	43.347	-142.128	309.082	-52.714

(C)

Figure 12. The left image (A) is an axial cross-sectional MR image created by subtracting two images by the ImageJ program. The right image (B) places the ROI marked with a yellow arrow on image A. (C) The table shows the results of intensity (mean) and noise (StdDev).

Mean of (SI (1) + SI (2)) = 2629.9

SD of (SI (1) - SI (2)) = 309.08

$$\mathrm{SNR}_{\mathrm{ROI}} = \frac{S_{\mathrm{ROI}}}{\sigma_{\mathrm{ROI}}} = \frac{2629.9}{1.41 * 309.08}$$

$$\mathrm{SNR}_{\mathrm{ROI}} = \frac{S_{\mathrm{ROI}}}{\sigma_{\mathrm{ROI}}} = \frac{2629.9}{435.8}$$

SNR = 6.03on T2W_3D_DRIVE or FIESTA was measured and recorded in, in addition to measuring the length of the nerve (on B FFE or FIESTA)

This methodology is sometimes referred to as the "difference method". One notable benefit of the difference approach is the requirement of only two-images, thereby enabling practical in vivo measurements of SNR. In order to get reliable SNR estimations, it is imperative that the signal remains consistent across the two images, similar to the multiple acquisition approach. Fluctuations in the signal might lead to erroneous SNR measurements. One primary drawback associated with this approach is the comparatively reduced effective spatial resolution, which leads to the smoothing out of SNR changes over the ROI. In the majority of clinical applications, the utilization of modest regions of interest (ROIs) mitigates any potential issues. Indeed, Gizweski et al. (2005), who employed a “sliding ROI” technique in combination with the difference method to produce a low-resolution SNR image, have undertaken the exploration of this notion. Both the local SNR and the dimensions of the ROI influence the accuracy of the SNR estimations inside the ROI. The error in estimating the SNR using the difference technique may be derived as per the findings of Reeder et al. (2005).

The error is determined by the size of the region of interest ROI in terms of pixels, denoted as NROI. An estimated error of ±4 can be observed in the SNR measurement at an SNR value of about 20 decibel (dB), corresponding to a 20% mistake. This error is encountered while employing a ROI consisting of 50 pixels.

The enlargement of the ROI leads to a reduction in its area, which in turn can mitigate fluctuations in the local SNR.

The utilization of tiny regions of interest (ROIs) is crucial in this methodology due to the potential for erroneous estimates of the g-factor when a ROI encompasses a pronounced transition in the g-factor, so we perfprmed a 3 pixels ROI in the measurments.

3.2 Methods of Contrast to Noise Ratio (CNR) Measurement

Contrast and noise are fundamental metrics employed in the assessment and characterization of image quality in a unit of decibel (dB). These metrics serve as widely accepted descriptors for evaluating the overall fidelity and clarity of an image.

The CNR measure is employed for the assessment of contrast deterioration and serves as an approximation of the level of noise present in the image. The CNR is mathematically expressed as the quotient of the discrepancy in the signal intensities observed in two distinct locations of interest, divided by the level of background noise. This relationship is represented by equation (2).

The contrast-to-noise ratio (CNR) is calculated using the formula (2):

$$\mathrm{CNR} = \frac{\mathrm{SI(n)} - \mathrm{SI(b)}}{\mathrm{Noise}} \qquad (2)$$

In this equation, $SI(n)$ represents the signal intensity of nerve area (n), $SI(b)$ represents the signal intensity of brain region (b), and N represents the background noise (Magnotta et al., 2006).

The viewed image quality is determined by the contrast between the real detected signal, which represents the true patient anatomy, and the undesirable signals that are randomly overlaid. Enhanced image quality is achieved by an increased disparity between these two factors, specifically a heightened signal-to-noise ratio (SNR). Therefore, it is customary to construct and store sequences in our scanners in order to get a satisfactory signal-to-noise ratio (SNR) for addressing the clinical inquiries at hand. In instances where an image exhibits a deficiency in signal-to-noise ratio (SNR), radiographers should possess the ability to promptly and intuitively identify this issue and choose the most suitable course of action to enhance the image quality. Typically, this involves making a trade-off between image resolution and scan duration in order to achieve improvement.

However, the Contrast to Noise Ratio (CNR) is not as well known. In addition to providing a metric for image quality, it aims to characterize the capacity to discern adjacent structures composed of different tissue types, specifically their disparity in signal-to-noise ratios (SNRs).

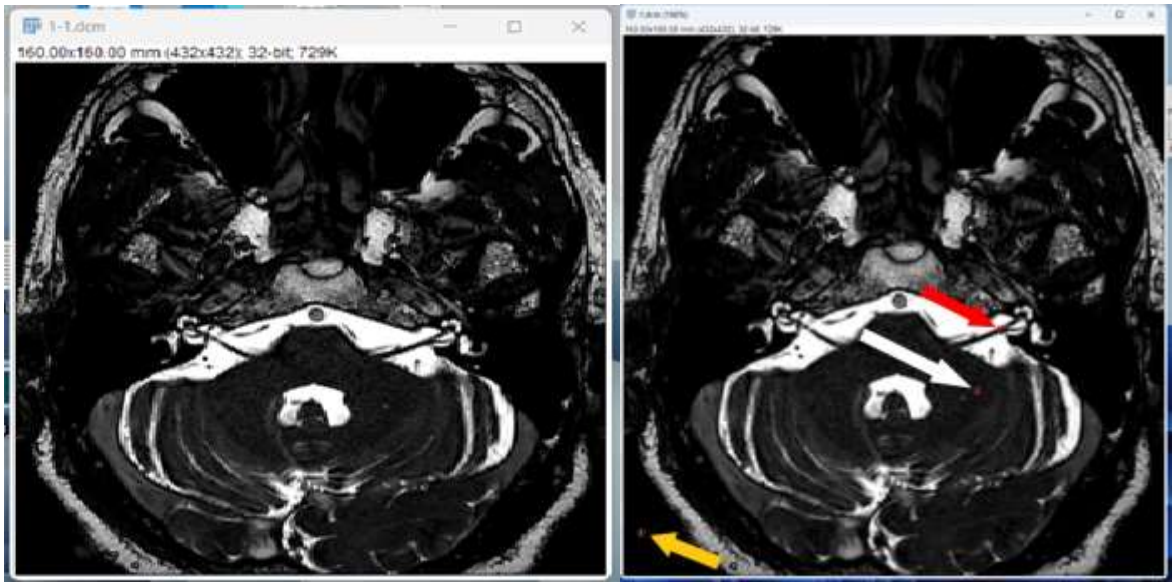

(A) (B)

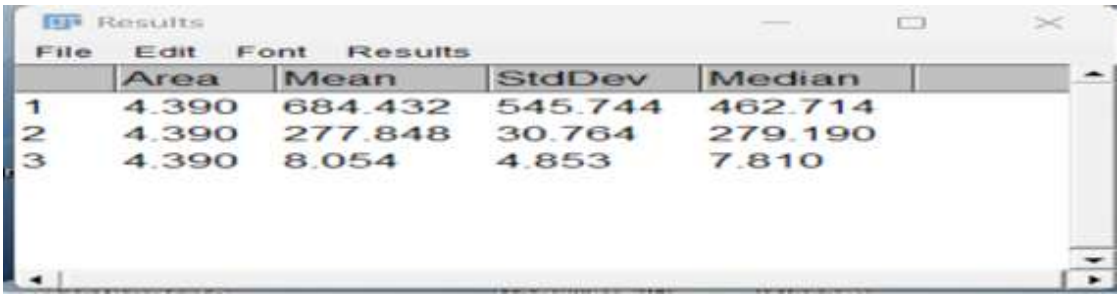

(C)

Figure 13. The left image (A) of the axial cross-sectional MR image shows the VCN. The right image (B) places three ROIs on image (A), one on the VCN with the red arrow, the second marked with a white arrow on the brain tissue, and the third marked with a yellow arrow on the image background. (C) The table shows the results of intensity (mean) and noise (StdDev) for the three determined regions.

Determining contrast-to-noise in an MR image requires an estimate of the contrast (difference in signal between two tissues or materials) and an estimate of the noise.

The signal in each of two tissues or materials (x and y) is estimated* from the mean value in a region of interest representing each tissue or material. The contrast (C) is the difference between those values:

- SI (n) = mean (tissue of the nerve) = 684.432
- SI (b) = mean (tissue of the brain) = 277.848
- C = SI (n) – SI (b)

  = 684.432 - 277.848 = 406.584

The noise (N) is estimated as the standard deviation from a region in the background where there is no signal:

- N = STD (region in background noise)

Contrast-to-noise ratio (CNR) is just the ratio of the estimated contrast and noise:

- CNR = C/N

  = 406.584/4.853 = 83.78 dB

The multiplanar reconstructions (MPRs) were conducted separately by three experienced radiologists with over 5 years of expertise in magnetic resonance imaging (MRI). The

reconstructions were conducted with the 3D application of the RadiAnt DICOM Viewer ®, multiplanar reconstruction (MPR) was conducted in the parasagittal plane, which was oriented perpendicular to the longitudinal axis of the internal auditory canal, as well as perpendicular to the longitudinal axis of the vestibulocochlear nerve (VCN). In order to maintain consistent and precise assessments across all patients, no modifications were made to the display parameters, including the window or center settings. These display characteristics were fixed for all images.

The process of image review was conducted by the same radiologists and all of them from a different region and blinded to each other and to other patient medical records. The radiologists were unaware of the clinical facts pertaining to the patient. In order to conduct an evaluation, the magnetic resonance (MR) images were examined.

Both the maximum (DMAX) and minimum (DMIN) axis on the cross-sectional surface area of each nerve on axial view on T2W_3D_DRIVE or FIESTA was measured and recorded in, in addition to measuring the length of the nerve (on B FFE or FIESTA) image which recorded in units of millimeters. The three radiologists performed further diagnostic analysis of MRI exams separately. We have done a statistical measure of mean, standard deviation, and range, and then computed the measurements and diagnostic reports of vestibulocochlear nerves.

Chapter 4. Results

4.1 Sample Characteristics

A sample of 49 patients who had undergone an IAC MRI examination to diagnose the inner ear was obtained, with a mean age of 36.18 years and a median age of 32.00. ENT physicians referred 32 of this sample for an MRI scan based on the preliminary results of the VNG,PTA, and ABR exams, which revealed vestibular or auditory system disorders. ENT specialists referred 17 patients from the sample for an MRI evaluation only based on symptoms and clinical diagnosis.

4.2 Observers Result

Three observers used the MR images to identify the diseases that were present in a total of 49 MRI scans. The following illnesses were represented by 14 number signs in the IBM SPSS version 20 statistic program: normal; sinusitis; labyrinthitis; otitis media; mastoiditis; cholesteatoma; an empty sella turcica; a simple cyst; an infarction; inflammatory illness; little mucosal thickening of the antrum. The descriptive statistic was calculated using the IBM SPSS version 20 statistical tool, and the intraclass correlation, also known as the intraclass correlation coefficient (ICC), was calculated to evaluate the consistency or reproducibility of the three observers.

Table 5: Statistical analysis results for the three observers.

	Mean	Minimum	Maximum	Range	Maximum / Minimum	Variance	N of items
Item means	1.27	0.61	2.33	1.71	3.8	0.84	3

The differences between the means for the observers were calculated; Table 6 shows the high mean value is 2.34 for observer number 3, and the lowest mean value is 0.61 for observer 1.

Table 6: Comparison between mean and standard deviation (Std. Deviation) for the three observers.

Observers	Mean	Std. Deviation
Observer 1	0.61	1.60
Observer 2	0.89	1.99
Observer 3	2.33	3.76

The inter-observer correlation was also calculated, and Table 7 shows the correlation between the three observers.

Table 7: Inter-item correlation for the three observers.

	Observer 1	Observer 2	Observer 3
Observer 1	1	0.79	0.26
Observer 2	0.79	1	0.31
Observer 3	0.26	0.31	1

Table 8: Intraclass correlation coefficient.

	Intraclass correlation	95% confidence interval		F test with true value 0			
		Lower Bound	Upper Bound	Value	df1	df2	Sig

Single measures	.309a	0.132	0.493	2.342	48	96	0
Average measures	.573c	0.314	0.745	2.342	48	96	0

Two-way mixed effects model where people effects are random and measures effects are fixed.

a. The estimator is the same, whether the interaction effect is present or not.

b. Type C intraclass correlation coefficients using a consistency definition. The between-measure variance is excluded from the denominator variance.

c. This estimate is computed assuming the interaction effect is absent, because it is not estimable otherwise.

4.3 Result of MR images

The diagnosing result for MR images for all cases that performed vestibular function tests shows many diseases; Table 9 shows the diseases that were diagnosed by each radiologist and their percent degree.

Table 9: Diagnosing diseases in MR images and their percentages.

MRI diagnoses	Frequency	Percent	Valid percent	Cumulative percent
No pathology seen	15	46.9	46.9	46.9
Sinusitis	7	21.9	21.9	68.8
Labyrinthitis	2	6.3	6.3	75

Mastoiditis	2	6.3	6.3	81.3
Cholesteatoma	1	3.1	3.1	84.4
Empty sella turcica	1	3.1	3.1	87.5
Microvascular disease	1	3.1	3.1	90.6
White matter disease, Dysmyelinating disorders	2	6.3	6.3	96.9
Mild mucosal thickening of the antrum	1	3.1	3.1	100
Total	32	100	100	

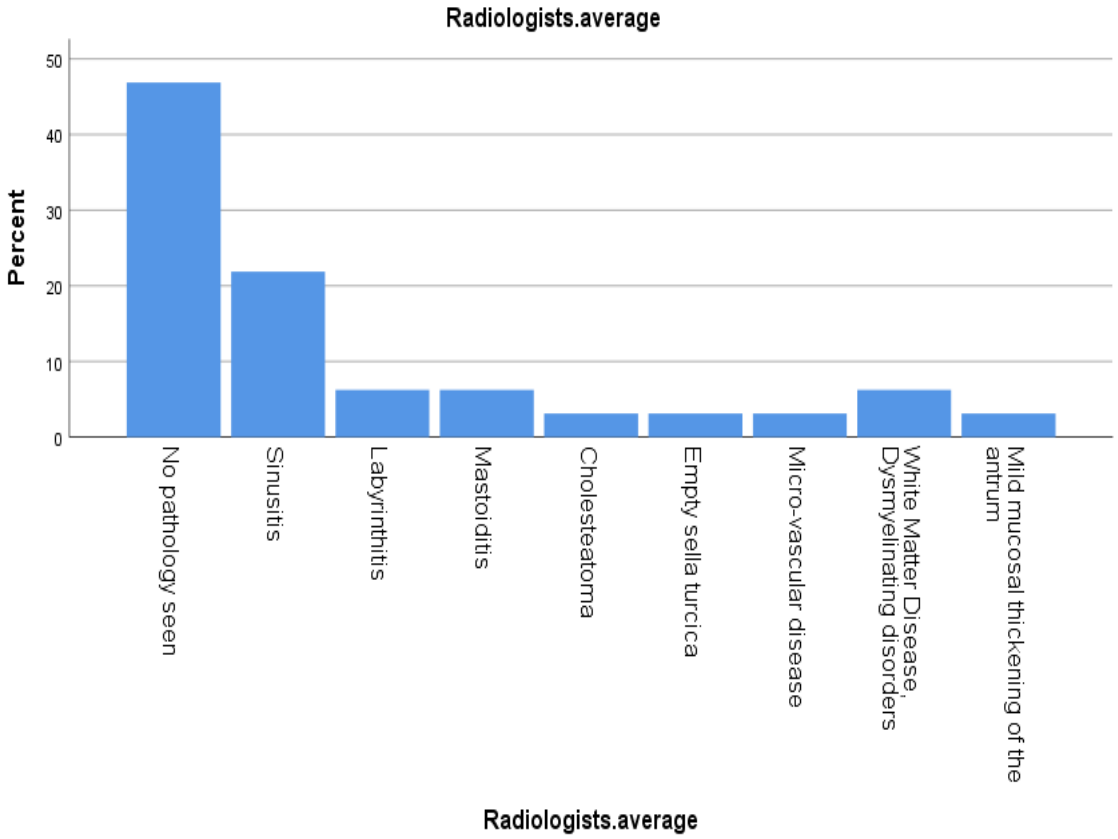

Figure 14. A bar chart depicting the frequency and percentage of pathologies identified on the diagnostic MR images.

The following MR images depict the diseases that have been diagnosed (Figs. 15-27):

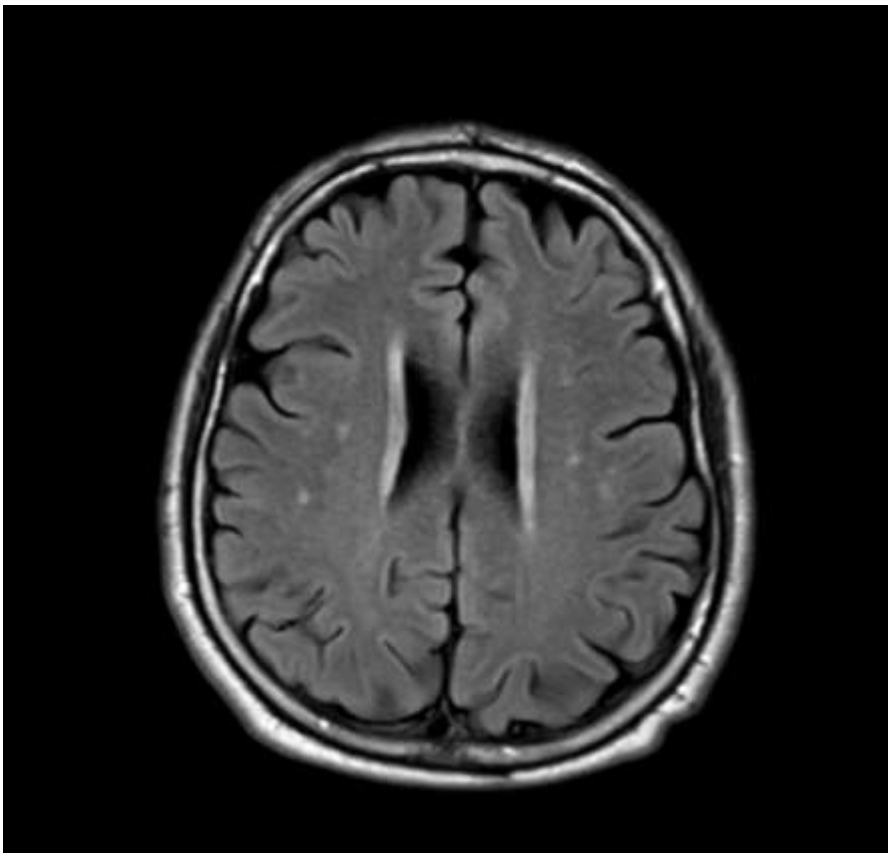

Figure 15. Axial MRI FLAIR-long TR image for patient number 1 shows mild microvascular disease. Small-vessel disease progression on brain MRI, the image shows pencil-thin lining on white-matter lesions at baseline. Large confluence extended into deep white-matter lesions at. And shows a punctate white-matter lesion at baseline, and a confluent white-matter lesion appeared on the same regions.

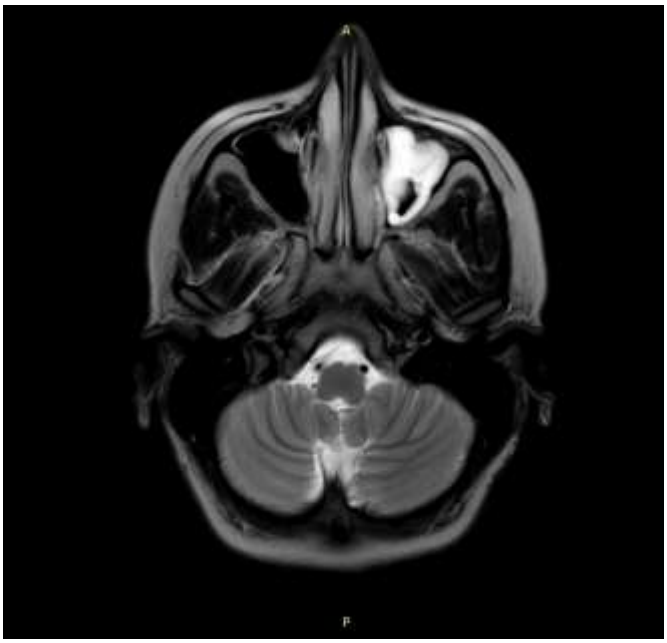

Figure 16. Axial MRI brain T2W-MV image for patient number 10 shows left maxillary sinusitis that appear hyperintense and partial opacification of left antrum.

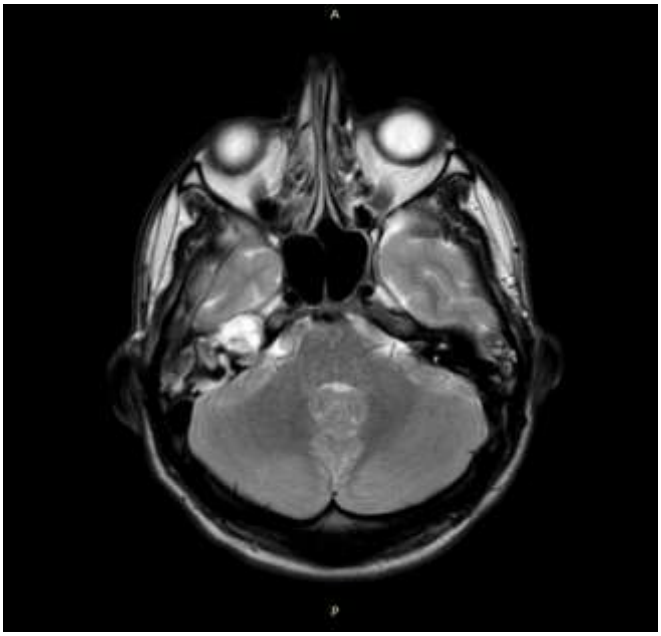

Figure 17. Axial MRI brain T2W-TSE image for patient number 9 shows Cholesteatoma and mild left mastoiditis.

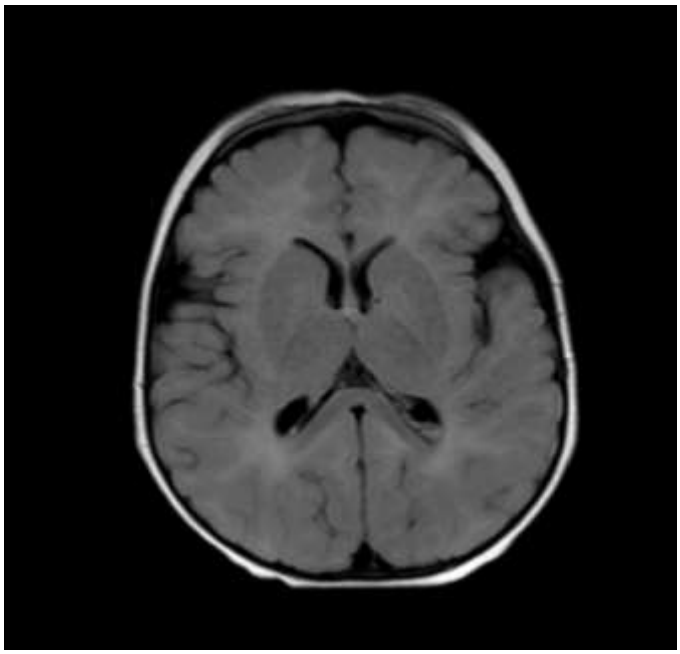

Figure 18. Axial MRI brain and temporal FLAIR-long TR image for patient number 8 shows dysmyelinating disorders.

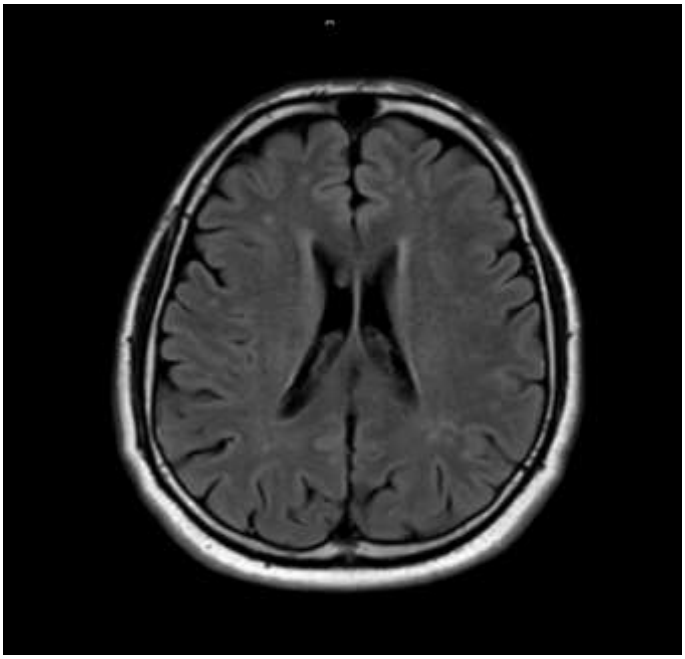

Figure 19. Axial MRI brain-IAC FLAIR-long TR image for patient number 12 shows microvascular disease.

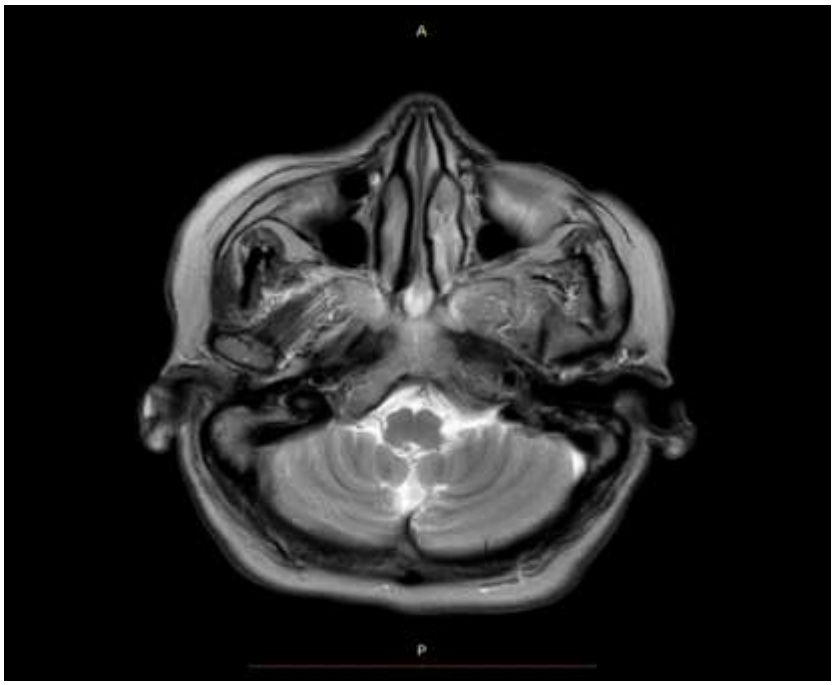

Figure 20. Axial MRI brain T2W-MV image for patient number 14 shows diploic mastoid, microvascular changes, midbrain, pons, left cerebellar peduncle, and left occipital lobe acute ischemic insults.

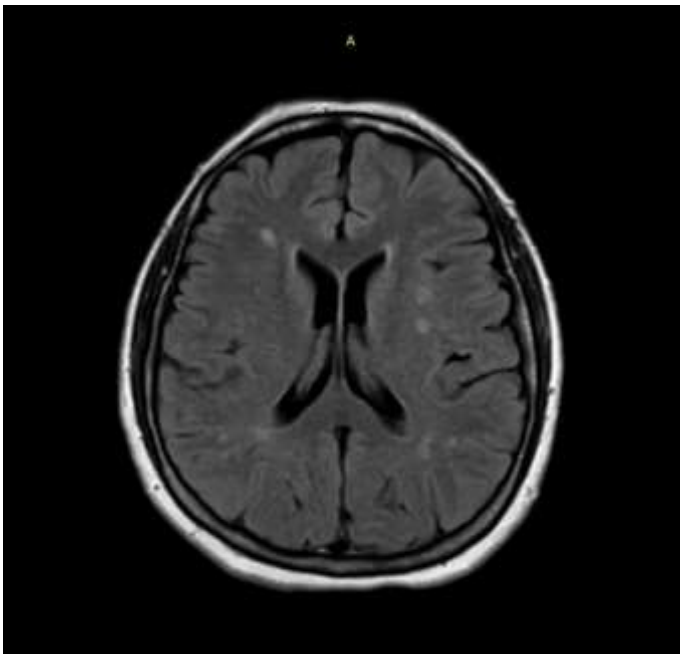

Figure 21. MRI brain-IAC FLAIR-long TR axial image for patient number 17 shows labyrinthitis ossificans , non-specific white matter disease.

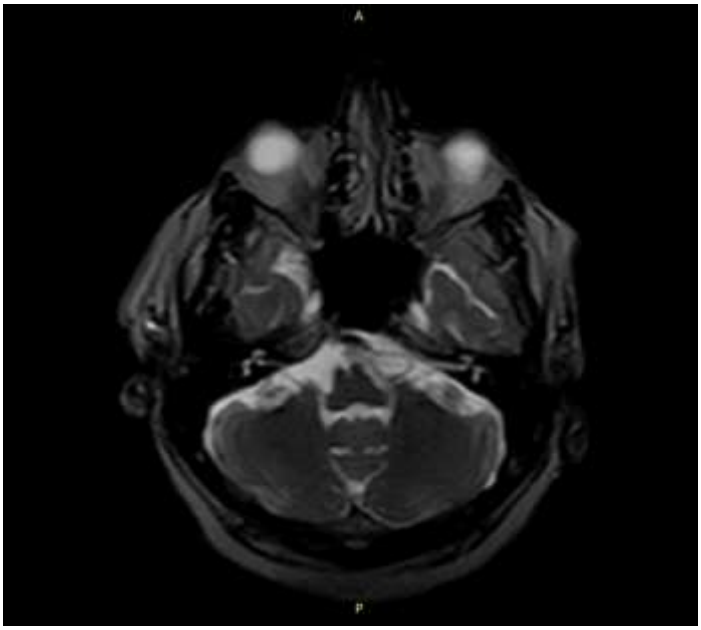

Figure 22. Axial MRI brain T2W image for patient number 18 shows tortuous basilar artery.

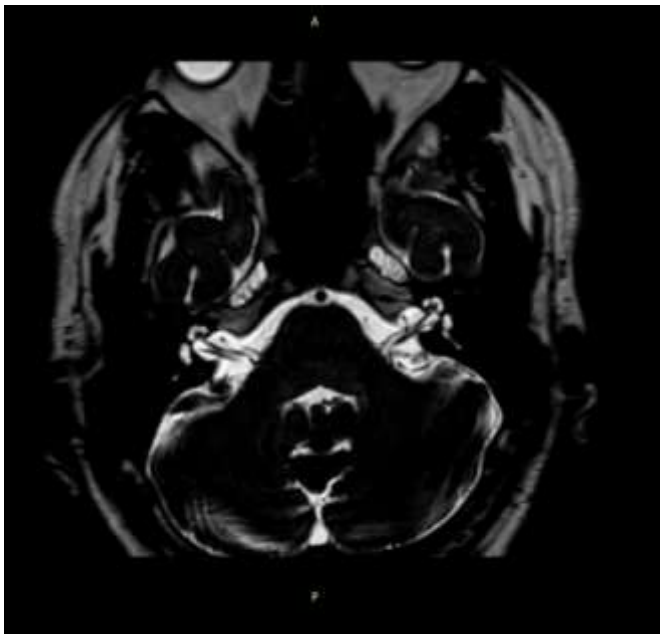

Figure 23. Axial MRI brain-IAC T2W-3D-DRIVE image for patient number 7 shows patulous IAC.

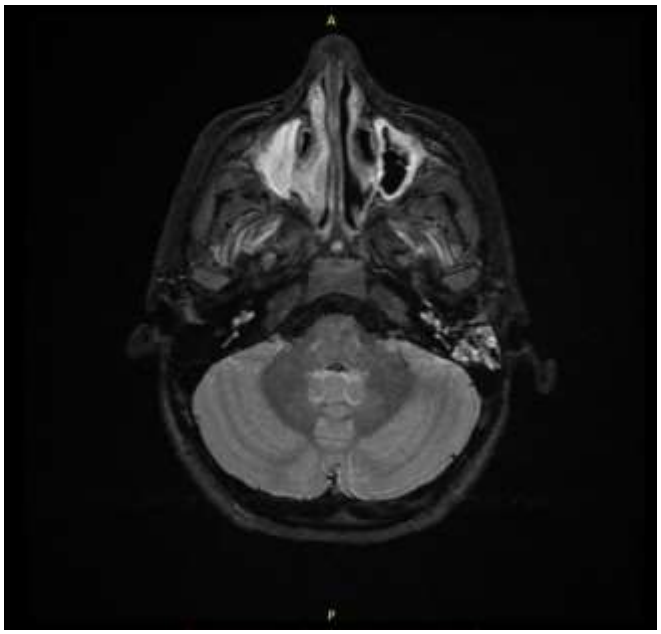

Figure 24. Axial MRI mastoid STIR (Thin) image for patient number 31 shows left mastoiditis, otitis, sinusitis.

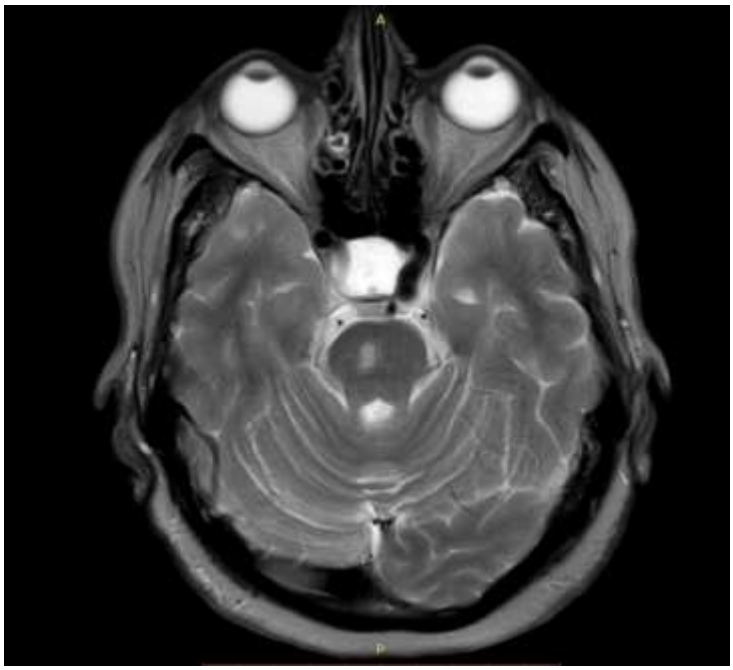

Figure 25. Axial MRI brain and cervical T2W-MV image for patient number 44 shows brain stem old infarction.

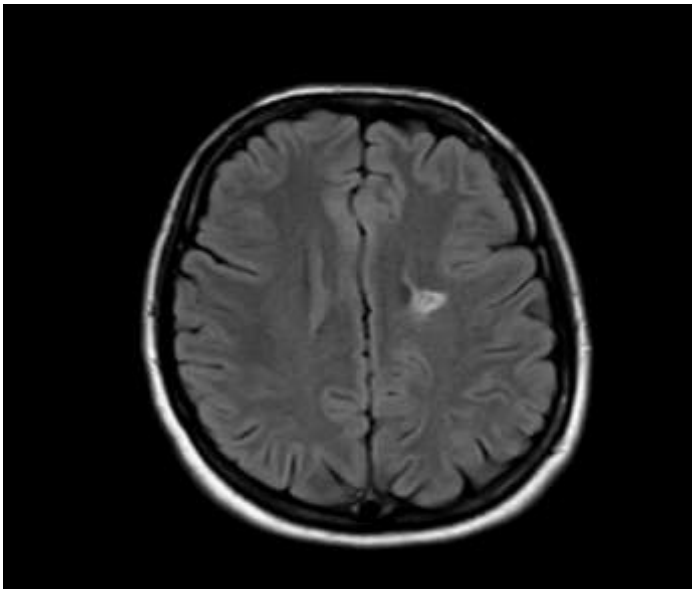

Figure 26. Axial MRI brain and orbit with contrast FLAIR-long TR image for patient number 45 shows old liquefied insult in the left corona radiata.

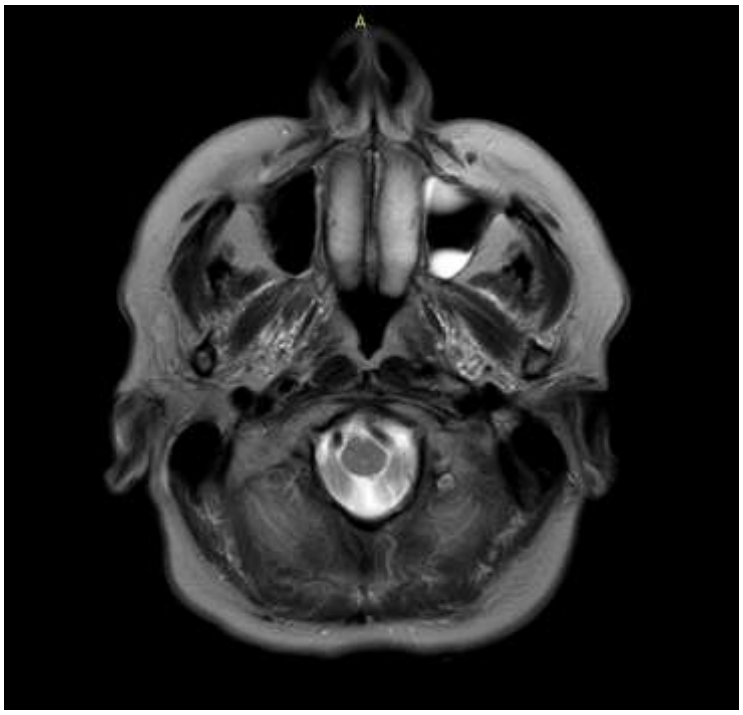

Figure 27. Axial MRI brain T2W-MV image for patient number 16 shows mild mucosal thickening of the antrum.

The three observers carried out six measurements of the VCN diameters. The measurement results are shown in Table 10. Another set of measurements was made and displayed in Table 20 to compare the VCN measurements between normal and abnormal cases, and the comparison was done using a bar chart (Figures 42, 43, 44, 45).

Table 10: Diameter measurements' of the VCN.

Measurements	LRN	LLN	RDMAX	RDMIN	LDMAX	LDMIN
Mean	19.04	19.08	1.74	1.09	1.76	1.07
Std. Deviation	2.24	2.86	0.38	0.25	0.39	0.29
Minimum	13.00	10.03	1.01	0.66	0.61	0.20
Maximum	23.77	24.47	2.61	1.76	2.59	1.99

There are 7 cases in the sample for which the observers were unable to perform nerve measurements because performing the measurement is not applicable due to the following reasons:

1. Patients; Anonymous0003, Anonymous0004, Anonymous0005, Anonymous0009, Anonymous00047, Anonymous00049: The IAC protocol was not followed, missing the appropriate sequence.
2. Patient; Anonymous00026: Motion artifact, the nerve edges not detectable.

In this study, 49 patients underwent an MRI scan, and radiologists performed a six distinct measurements of the VCN for 42 of them, whereas 7 patients had no measurements taken due to the previously indicated reasons. The average nerve length, cross sectional area, cross sectional area for positive cases, and cross sectional area for negative instances were then measured; the findings are shown in Table 20.

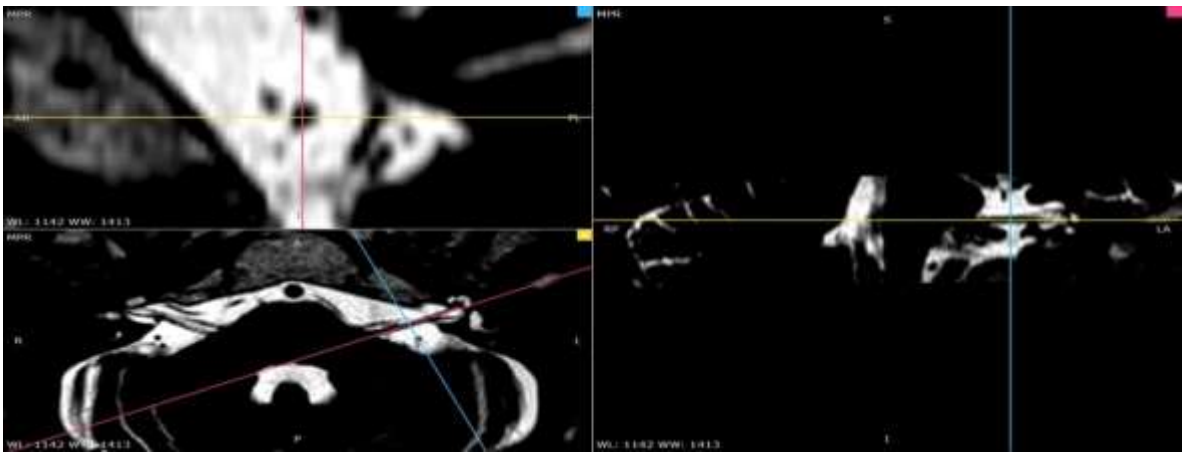

Figure 28. MPR MRI images for patient number 1 shows the axis of measurement in parasagittal orientation which is perpendicular to the long axis of the internal auditory canal.

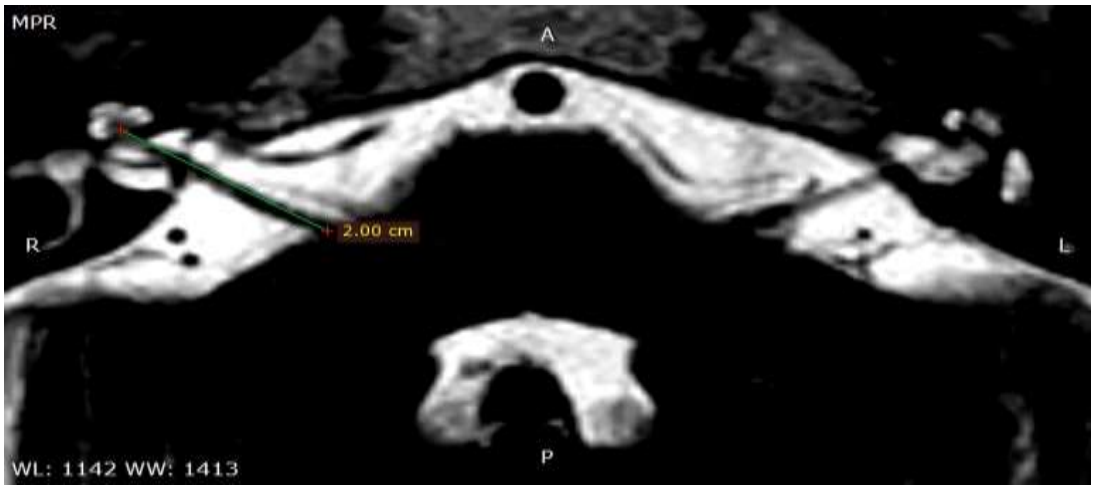

(A)

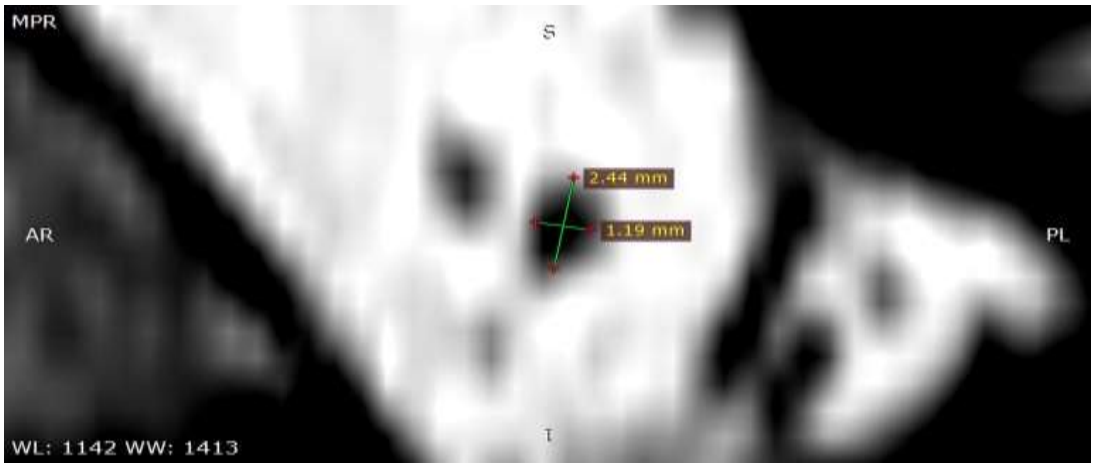

(B)

Figure 29. 3D DRIVE images for patient 1. (A) shows the right side VCN length measurement of 2cm, and (B) shows the left side DMAX of VCN (2.44mm) and DMIN (1.19mm).

4.4 Phantom Result for SNR and CNR

Figure 30 shows the GE Healthcare MRI water phantom images of the sequences, from which we measured SNR and CNR. Table 11 show the SNR values for different GE Healthcare sequences that used in imaging phantom (TLT Head Sphere Phantom for GE Closed MRI).

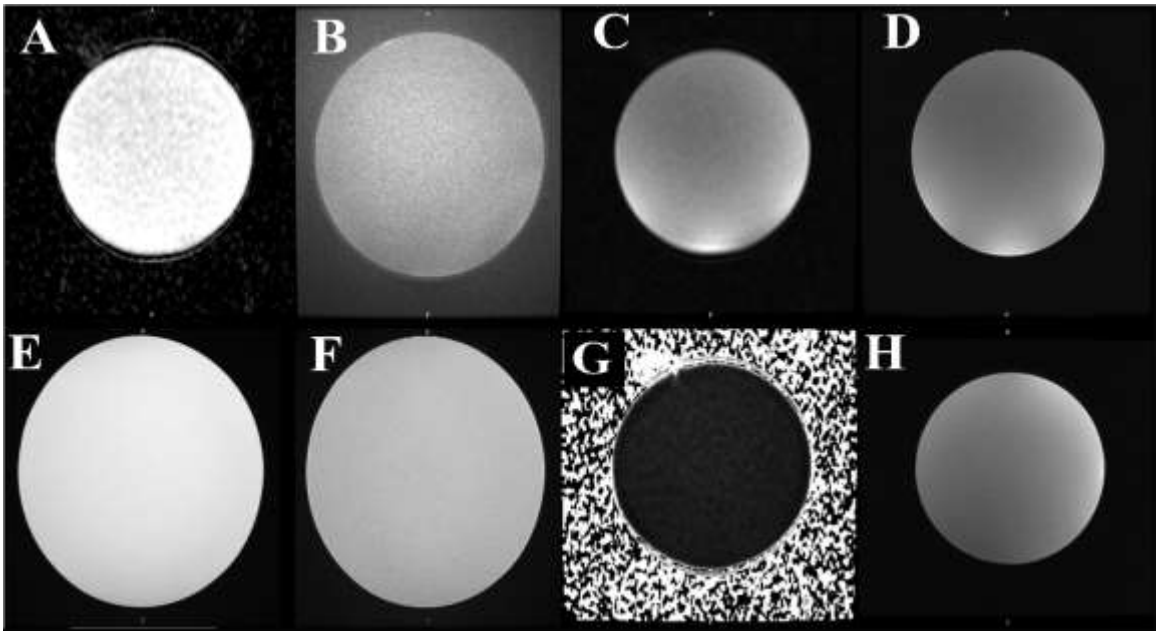

Figure 30. GE Healthcare MRI water phantom images of the sequences, from which we measured SNR and CNR. A: Apparent Diffusion Coefficient (ADC), B: 3D FIESTA A-C CAI 0.6mm, C: DWI b1000 (2MM), D: T2 FLAIR 5mm, E: T1 FSE 2.5mm, F: T2 FRFSE 2.5mm, G: Exponential Apparent Diffusion Coefficient**,** H: STIR 2.5mm.

Table 11: Phantom SNR measurements for GE Healthcare sequences.

GE Sequence	SNR (in dB unit)
STIR	55.17
ADC	27.83
DWI-2mm	59.21
EADC	10.62
Coronal-T1-FSE-Thin	85.97
Axial-T2-FLAIR	45.81
Coronal-T2-FSE-Thin	47.23
3D-FIESTA	32

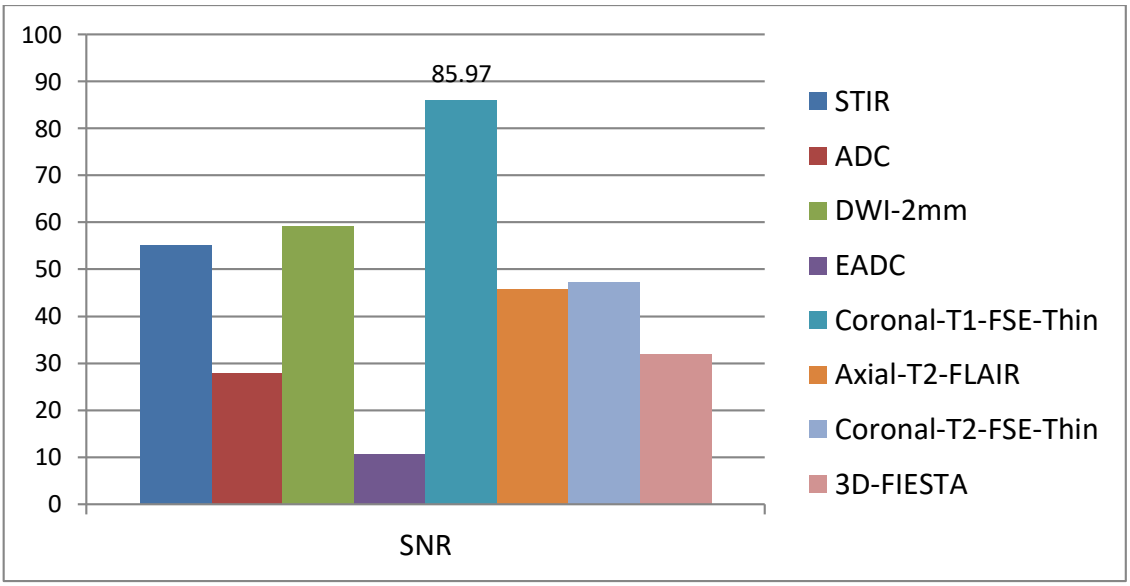

Figure 31. A bar chart for GE sequences shows the result of SNR in Phantom.

SNR for phantom, (Philips MRI Phantom Bottle 3000 cc) was also measured for Philips sequences as shown in Table 12. Figure 32 shows the Philips Healthcare MRI water phantom images of IAC sequences, from which we measured SNR and CNR.

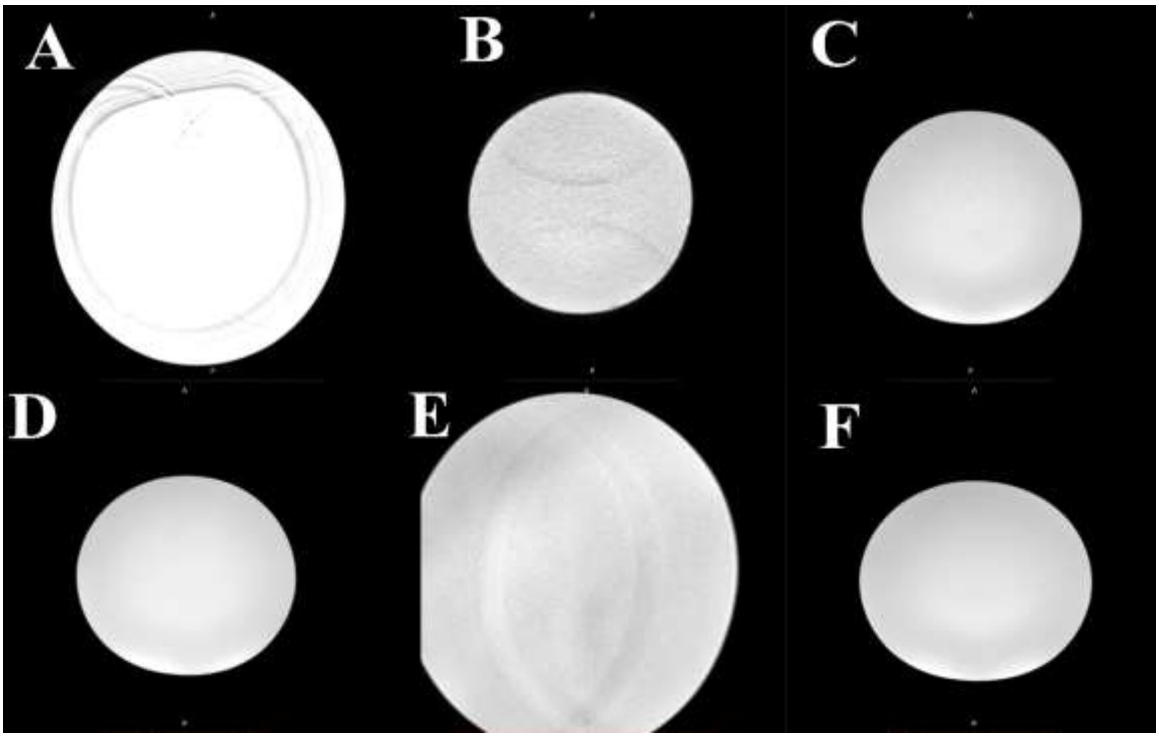

Figure 32. Philips Healthcare MRI water phantom images of IAC sequences, from which we measured SNR and CNR. A: B_FFE_150 Slices, B: DWI, C: FLAIR, D: T1W_SE, E: T2W_3D_DRIVE, F: T2W_FFE.

Table 12: SNR measurements for Philips Healthcare sequences in Phantom.

Philips healthcare sequences	SNR (in dB unit)
T1W-SE	154.16
FLAIR-Long TR	129.06
T2W-3D-DRIVE	53.12
B-FFE-150 slices	38.12
DWI-2mm	20.79
T2W-FFE	162.97

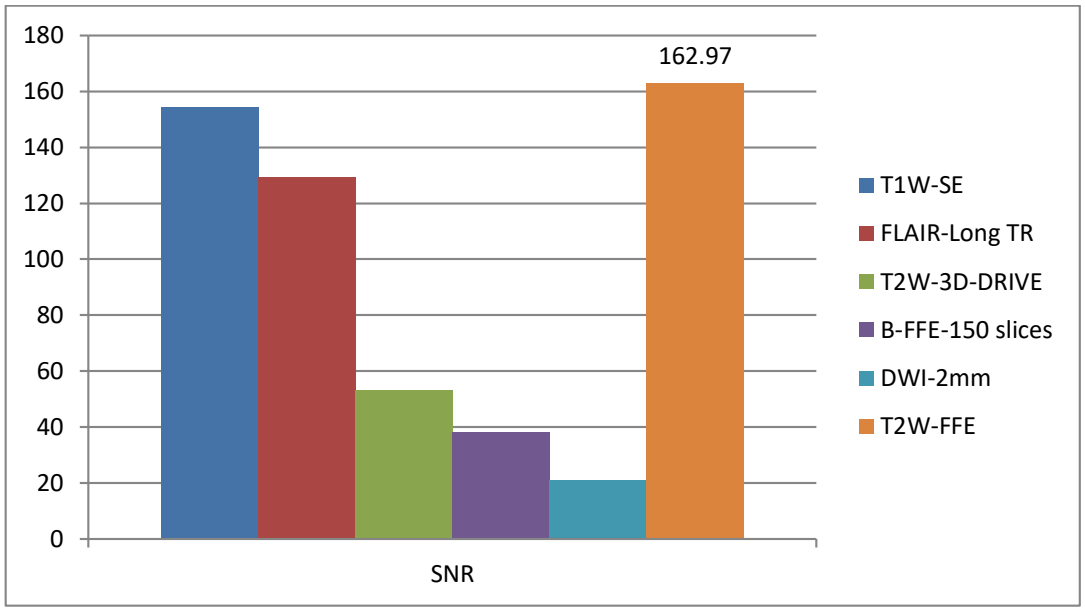

Figure 33. A bar chart depicting the SNR value in dB unit of the linked Philips Healthcare sequences in Phantom.

Phantom CNR results for GE Healthcare sequences in Table 13 shows the CNR for the different sequences that used.

Table 13: CNR measurements for GE Healthcare sequences in Phantom.

GE Healthcare Sequence	CNR (in dB unit)
STIR	28.16
ADC	0.34
DWI-2mm	6.99
EADC	0.03
Coronal-T1-FSE-Thin	5.18
Axial-T2-FLAIR	6.68
Coronal-T2-FSE-Thin	1.2
3D-FIESTA	0.48

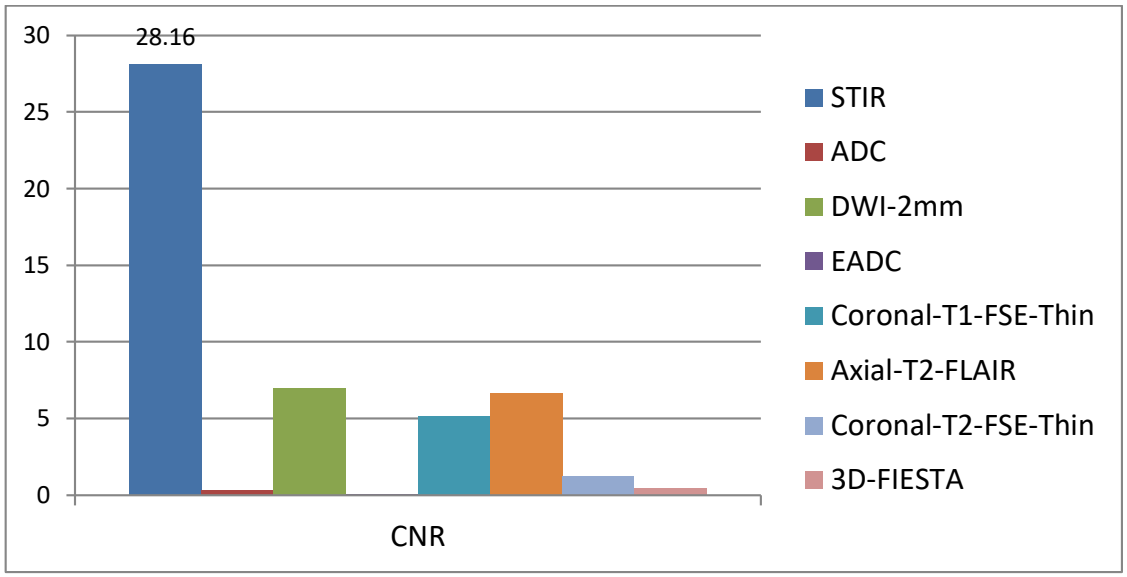

Figure 34. A bar chart for GE Healthcare sequences show the result of CNR in dB in Phantom.

Phantom CNR findings in Philips Healthcare are shown in Table 14 along with the various sequences utilized to image the phantom.

Table 14: CNR results for Philips Healthcare sequences in Phantom.

Philips Healthcare sequences	CNR
T1W-SE	12.56
FLAIR-Long TR	27.59
T2W-3D-DRIVE	0.8
B-FFE-150 slices	12.88
DWI-2mm	11.3
T2W-FFE	7.76

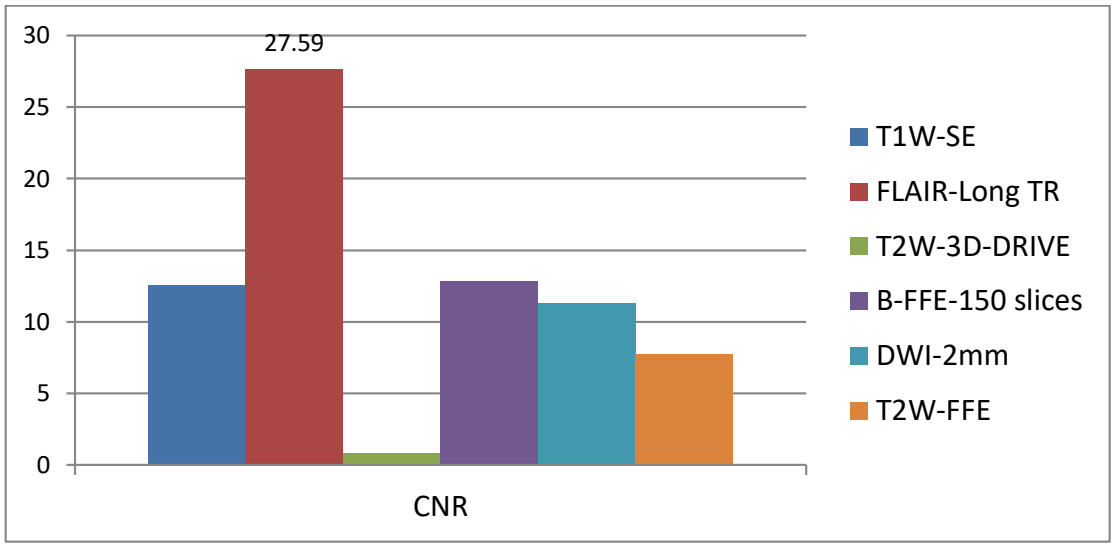

Figure 35. A bar chart show the CNR value of the linked Philips Healthcare sequences in Phantom.

4.5 MR Images SNR and CNR Results for GE Healthcare and Philips Healthcare

For 18 individuals, an MRI examination was performed using a GE scanner whereas the remaining 31 patients were examined using a Philips Healthcare MRI scanner. SNR and CNR values (in dB unit) for tissues were measured for each of the sequences utilized in both types of scanners to examine the sample in order to evaluate the quality of the MRI images. The values of central tendency were measured and examined, and the mean, standard deviation, maximum value, and minimum value were obtained as findings.

4.5.1 GE Healthcare SNR and CNR Result

For GE Healthcare sequences, the SNR and CNR quality metrics of the MRI images of all sequences used for IAC imaging were assessed. The mean SNR value, standard deviation (SD), minimum value, and maximum value were all calculated, as shown in the Table 15.

Table 15: SNR results for GE Healthcare sequences in Vivo.

GE Sequence	Mean	SD	Minimum	Maximum
T1W_SE	4.88	2.49	2.44	7.24
STIR	3.81	2.25	1.6	11.82
ADC	2.54	1.24	0.71	6.49
3D_FIESTA	11.21	7.59	4.23	37.48
DWI 2MM	4.27	1.92	1.1	9.83
CorT1FSE (Thin)	3.86	2.41	1.12	9.85
CorT2FSE (Thin)	2.91	1.59	0.95	5.78
AX T2 FLAIR	4.65	0.98	3.41	5.7

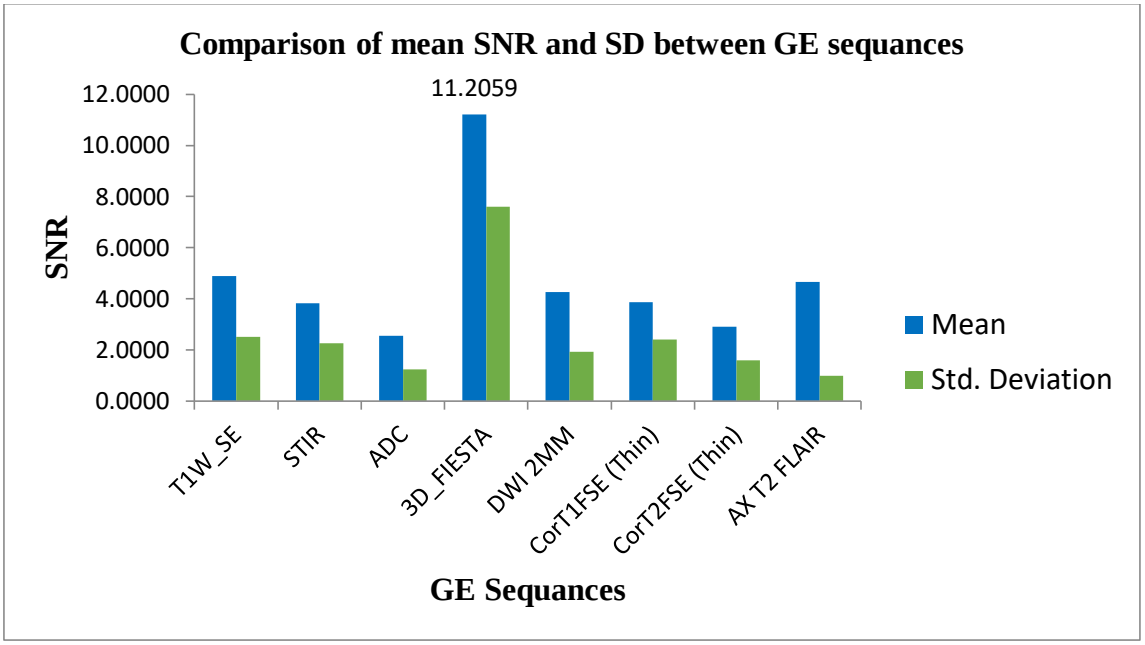

Figure 36. A bar chart analyze the SNR (in dB unit) mean and standard deviation (Std. Deviation) results for each GE Healthcare imaging sequences in Vivo.

The findings indicate that the CorT2FSE (Thin) relay exhibits the highest mean value, measuring at 161.32 dB. Conversely, the ADC relay demonstrates the lowest CNR value, measuring at 2.01 dB. In addition to the calculated CNR mean. Table 16 presents the

corresponding standard deviation (SD), maximum value, and minimum value for all utilized GE Healthcare sequences.

Table 16: CNR results for GE Healthcare sequences in Vivo.

GE Healthcare Sequence	Mean (dB)	SD	Minimum	Maximum
T1W_SE	46.77	5.35	43.43	52.94
STIR	57.71	60.17	3.01	205.26
ADC	2.01	2.59	0.38	10.95
3D_FIESTA	51.44	60.19	0.14	202.56
DWI 2MM	83.90	108.95	6.94	402.76
CorT1FSE (Thin)	45.93	26.49	17.91	125.44
CorT2FSE (Thin)	161.32	99.62	2.19	346.76
AX T2 FLAIR	48.64	43.30	14.83	124.56

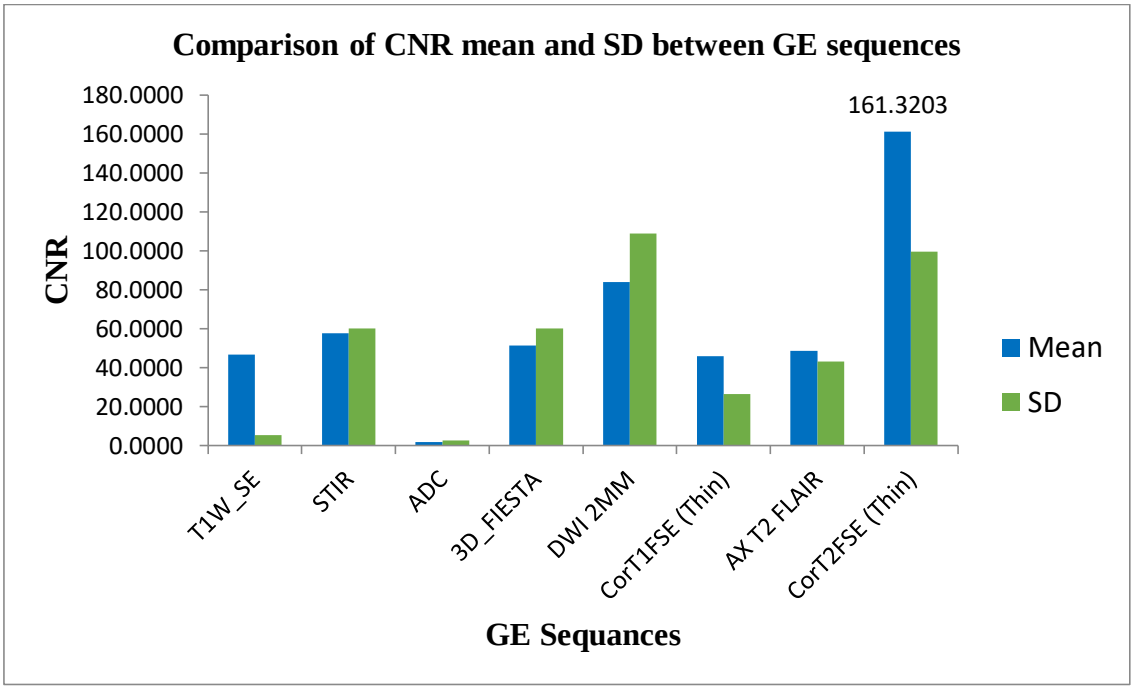

Figure 37. A bar chart shows the CNR mean and standard deviation (SD) results in decibel (dB) scale for each GE Healthcare imaging sequences in Vivo.

4.5.2 Philips Healthcare SNR and CNR Result

The mean SNR value, standard deviation (SD), minimum value, and maximum value of the Philips sequences were computed and are presented in Table 17. The T1W_FFE imaging sequence has the highest average value among the imaging sequences, with an SNR value of 17.36 dB. On the other hand, the DWI 2MM imaging sequence demonstrates the lowest SNR value is 3.04 dB.

Table 17: SNR results in dB unit of Philips Healthcare sequences in Vivo.

Philips Healthcare sequence	Mean (dB)	SD (dB)	Minimum (dB)	Maximum (dB)
T2W_TSE	3.38	1.68	1.33	7.02
T1W_SE	8.63	8.34	2.03	33.08
3D_BRAIN_View_T2	4.78	0.93	3.39	6.32
FLAIR_LongTR	4.13	1.81	0.94	9.46
T2W_3D_DRIVE	5.35	2.31	2.39	11.3
B_FFE_150 Slices	4.58	2.17	2.32	10.42
DWI 2MM	3.04	1.98	0.94	10.14
Post gadoliniumT1	6.24	3.89	1.83	9.18
T2W_FFE	6.09	3.75	0.71	12.87
T2W_MV	6.79	3.11	1.37	11.79
T1W_FFE	17.36	13.21	8.02	26.7
FIESTA	10.03		10.03	10.03

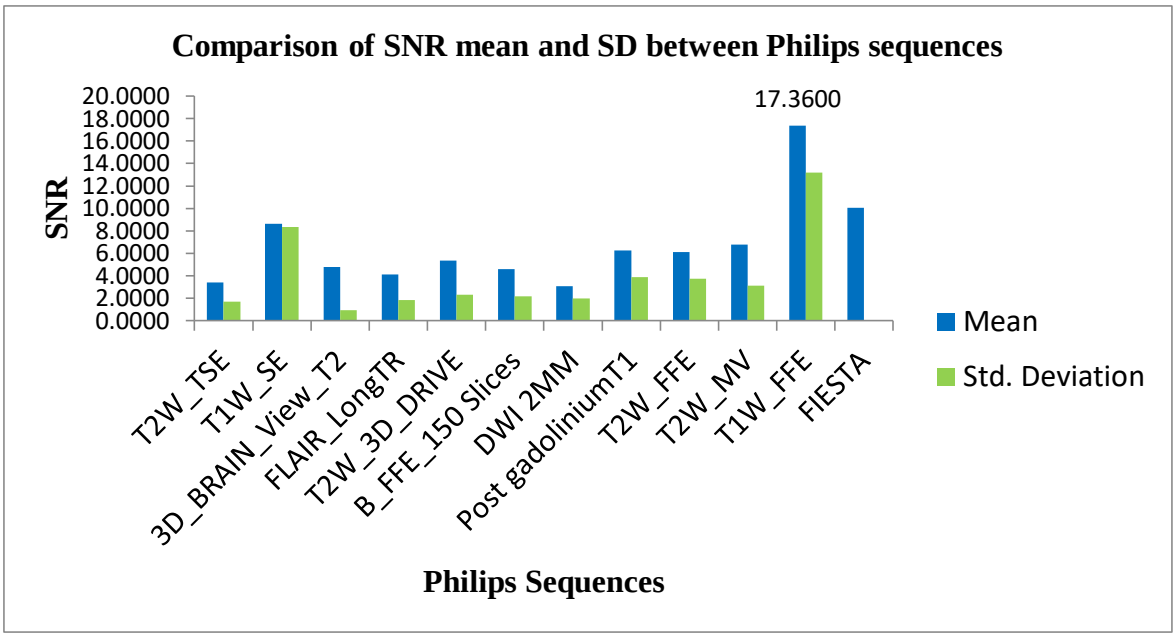

Figure 38. A bar chart analyze the SNR mean and standard deviation (Std. Deviation) results for each Philips imaging sequences in Vivo.

The results suggest that the FIESTA relay demonstrates the highest mean value, with a measurement of 322.26 dB. In contrast, the 3D_BRAIN_View_T2 relay exhibits the lowest contrast-to-noise ratio (CNR) value, measuring at 53.63 dB. In addition to the mean derived for the CNR. Table 18 displays the matching standard deviation (SD), maximum value, and minimum value for all the Philips Healthcare sequences that were utilized.

Table 18: CNR results of Philips Healthcare sequences in Vivo.

Philips Healthcare Sequences	Mean (dB)	SD (dB)	Minimum (dB)	Maximum (dB)
T2W_TSE	109.24	82.47	32.69	289.76
T1W_SE	138.12	164.91	8.3	893.32
3D_BRAIN_View_T2	53.63	54.49	1.66	165.99
FLAIR_LongTR	68.16	48.30	0.96	169.55
T2W_3D_DRIVE	88.78	157.39	2.34	700.38
B_FFE_150 Slices	112.06	203.19	0.95	787
DWI 2MM	199.16	149.76	0.46	596.74
Post gadoliniumT1	71.60	75.13	12.27	189.39
T2W_FFE	157.89	157.62	4.43	572.99
T2W_MV	205.42	140.70	2.56	545.11
T1W_FFE	133.27	150.64	0.94	277.07
FIESTA	322.26	109.9	244.55	399.97

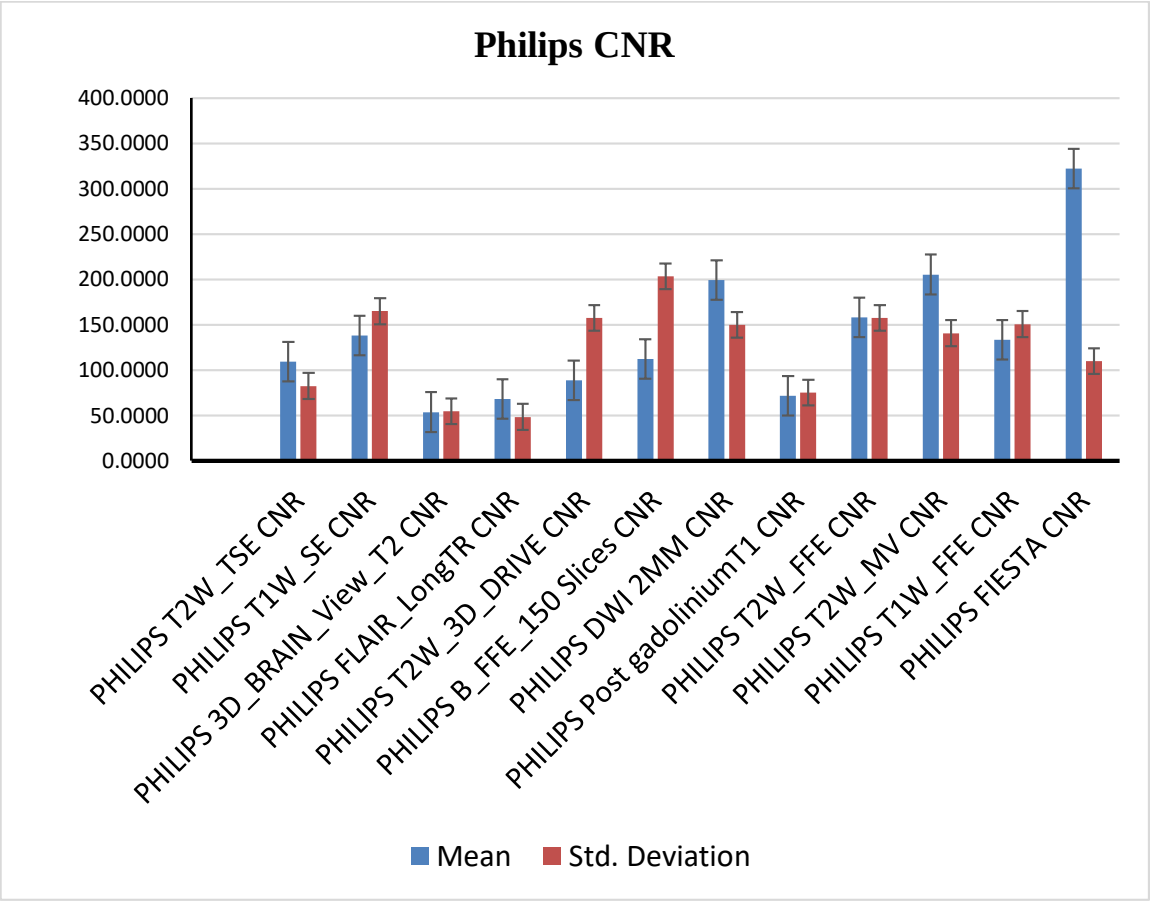

Figure 39. A bar chart shows the CNR mean and standard deviation (Std. Deviation) results in dB unit for each Philips Healthcare imaging sequences in Vivo.

4.5.3 Differences in the SNR and CNR of GE Healthcare and Philips Healthcare Sequences

Once signal-to-noise ratio (SNR) and contrast-to-noise ratio (CNR) values were acquired for all sequences utilized in imaging the sample. A comparative bar chart was generated to assess the variations in image quality between GE and Philips Healthcare machines. The shown bar chart (Figure 40) illustrates the differences in imaging sequences utilized by both machines, as determined by the mean values of the CNR and SNR (in dB unit).

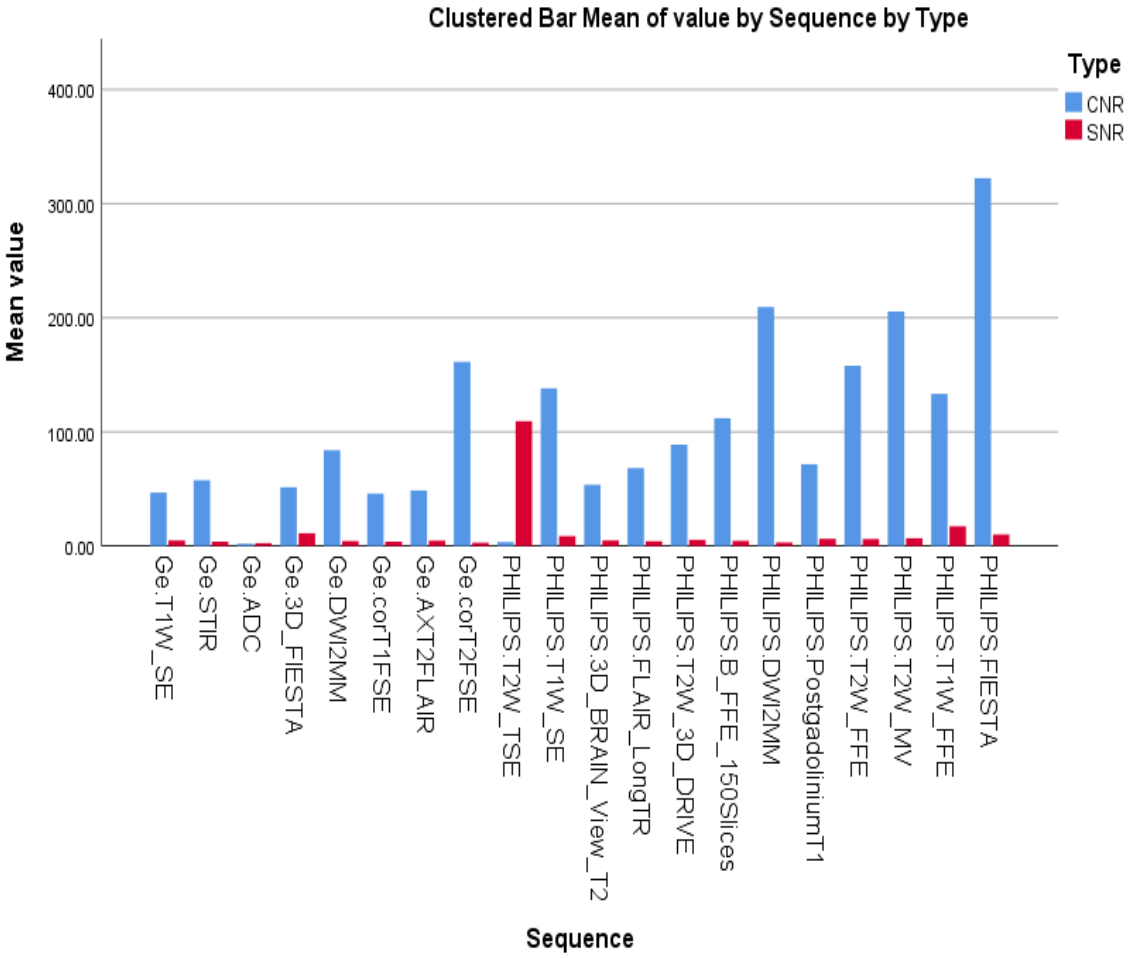

Figure 40. A bar chart shows the GE Healthcare and Philips Healthcare sequences SNR mean value and CNR mean value. This bar chart shows that the FIESTA Philips Healthcare sequence demonstrates the highest mean value of CNR, while the T2W_TSE Philips Healthcare sequence demonstrates the highest SNR value in Vivo.

An another comparative bar chart was generated to assess the variations in the image quality between GE Healthcare and Philips Healthcare machines. So this bar chart (Figure 41) illustrates the differences in imaging sequences utilized by both machines, as determined by the maximum values of the CNR and SNR.

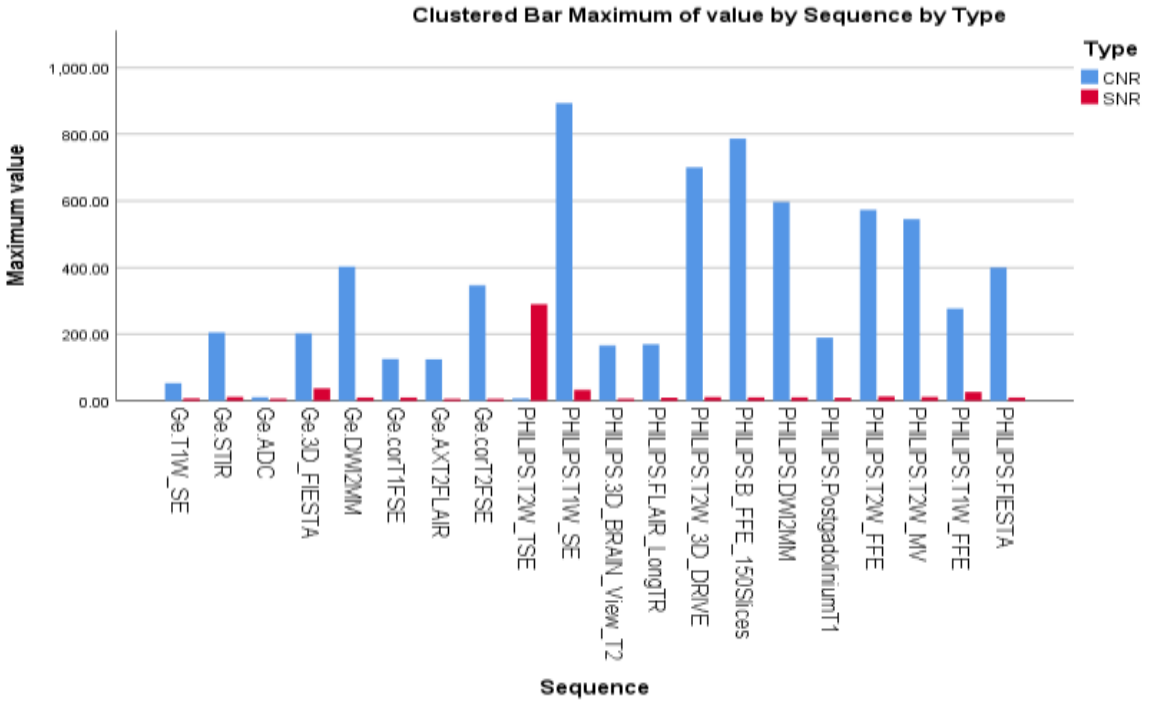

Figure 41. A bar chart shows the GE Healthcare and Philips Healthcare sequences SNR and CNR maximum values (in dB unit). This bar chart shows that the T1W-SE Philips Healthcare sequence demonstrates the highest maximum value of CNR, while the T2W_TSE Philips Healthcare sequence demonstrates the highest SNR maximum value in Vivo.

Chapter 5. Discussion

Because of its importance for the diagnosis of cranial nerves and central nervous system, magnetic resonance imaging has become one of the primary diagnostic procedures for individuals suffering from vertigo symptoms or who have an uncertain history of the vestibular disease. Many healthcare institutions have called for the direct use of MRI in these circumstances in order to acquire an etiological diagnosis, specialized therapy, and proper healthcare budget management.

The aim of this study is to examine the superiority of MRI over vestibular function tests (VNG/PTA) at diagnosing the cause of the disease and to compare its results with those of vestibular (VNG/PTA) exams on patients to recognize if MRI can be used in combined with or in place of vestibular function tests like VNG to diagnose these patients. And also to determine the appropriate examination that meets the need to diagnose the causes of diseases and reveal the final diagnosis of the disease in patients whose clinical examination or medical history shows limited indication of peripheral or central vertigo.

Another objective of this study is to determine the image quality of the different MRI sequences used by the two vendors by quantifying the image quality metrics (IQM), including SNR and CNR, and making a comparison between the quality metrics of different sequences.

The study included an evaluation of all aspects related to the MRI examination of the VCN, as it included the radiologist's evaluation of MRI images for the purpose of diagnosis and then performing multiple measurements of the VCN diameters. In addition to studying the

image quality of all the MRI exam sequences that were performed in all MRI examinations, these measurements of quality indicators included all imaging sequences and all vendors (GE Healthcare and Philips Healthcare) that were used for imaging in our study. Previous studies only focused on one of the aspects mentioned above. Some of them did on radiologists' investigations of diseases; some of them studied the diameter or length of the VCN; and others dealt with evaluating the image quality of some MRI sequences and making a comparison between them.

This research method differs from previous research in that it relied on selecting a sample from patients who all had abnormal VNG/PTA tests, as the results of VNG/PTA contained peripheral or central vestibular diseases.

The three radiologists' reading values have a mean of 1.28, a range of 1.71, a variation of 0.84, a minimum value of 0.61, and a maximum value of 2.33. The statistical analysis is depicted in Table 5. The consistency between observers 1 and 2 equals 0.79, which is good agreement and inter-observer reliability. There is no agreement between observer 1 and observer 2 with observer 3 because the correlation coefficients are 0.26 and 0.31, respectively. The conformity among observers was calculated, and the consistency or reliability equaled 0.573, this value lies in the range between 0.40 to 0.59 indicating fair inter-rater agreement, or conformity. The interclass correlation coefficient (ICC) is shown in Table 8.

The findings of this study reflect the finding of fair reliability between the three observers in diagnosing MRI images for the entire group of 49 patients, with an ICC value of 0.573. The estimated ICC value of 0.573 agrees with Cicchetti's (1994) interpretation of values ranging

from 0.40 to 0.59 indicating fair inter-rater agreement. The diagnostic results of the MRI examinations were positive in 15 patients (30.6% of the sample) and negative in 17 patients (34.7%).

The diagnostic findings obtained from magnetic resonance (MR) images of 32 patients who underwent vestibular function assessments (VNG/PTA) reveal the presence of various disorders, as presented in Table 9. Out of the total of 32 cases, 53.1 percent were found to have various diseases. These diseases included sinusitis (21.1 %), labyrinthitis (6.3 %), mastoiditis (6.3 %), cholesteatoma (3.1 %), empty sella turcica (3.1 %), microvascular disease (3.1 %), white matter disease and dysmyelinating disorders (6.3 %), and mild mucosal thickening of the antrum (3.1 %).

The results of the vestibular function tests (VNG and PTA) showed central vestibular dysfunction in 58.8% and peripheral vestibular dysfunction in 41.2% (Table 19). According to earlier research, VNG is a helpful test that assists in 75% of diagnoses of the vestibular disorders (Moideen et al., 2023). Vestibular function examinations are performed to identify damage to the inner ear or brain nerves (Kamath et al., 2015). In the current study, however, the MRI results of 15 samples out of 32 patients whose vestibular function test results suggested the presence of disease were normal.

Table 19: VNG - diagnosis * radiologists diagnosis crosstabulation.

VNG - Diagnosis	Percent % within: VNG – Diagnosis. Radiologist Average.	MRI Diagnosis								
		Sinusitis	Labyrinthitis	Mastoiditis	Cholesteatoma	Empty sella turcica	Micro – vascular disease	White matter disease	Antrum mucosal thickening	Total
Central Vestibular Dysfunction	Count	3	2	0	1	1	1	1	1	10
	Within VNG	30.00%	20.00%	0.00%	10.00%	10.00%	10.00%	10.00%	10.00%	100.00%
	Within Radiologists	42.90%	100.00%	0.00%	100.00%	100.00%	100.00%	50.00%	100.00%	58.80%
Peripheral Vestibular Dysfunction	Count	4	0	2	0	0	0	1	0	7
	Within VNG	57.10%	0.00%	28.60%	0.00%	0.00%	0.00%	14.30%	0.00%	100.00%
	Within Radiologists	57.10%	0.00%	100.00%	0.00%	0.00%	0.00%	50.00%	0.00%	41.20%
Total	Count	7	2	2	1	1	1	2	1	17
	Within VNG	41.20%	11.80%	11.80%	5.90%	5.90%	5.90%	11.80%	5.90%	100.00%
	Within Radiologists	100.00%	100.00%	100.00%	100.00%	100.00%	100.00%	100.00%	100.00%	100.00%

In our study, the results of vestibular function test revealed that 10 patients (58%) were diagnosed with central vestibular dysfunction. Further analysis comparing these results with MR examinations indicated that these central disorders were characterized by specific conditions in each patient. Specifically, sinusitis was observed in 3 patients (30% of central vestibular disorders for vestibular function test (VNG/PTA)), labyrinthitis in 2 patients (20.0%), cholesteatoma in one patient (10%), empty sella turcica in one patient (10%), micro-vascular disease in one patient (10%), white matter disease and dysmyelinating disorders in one patient (10%), and mild mucosal thickening of the antrum in one patient (10%).

The vestibular function examination results for 7 patients (41.2%) revealed the presence of a peripheral vestibular disorder, whereas their final MR imaging results revealed the presence of sinusitis in 4 patients (57.1% of peripheral vestibular disorders for vestibular function test (VNG/PTA)), mastoiditis in 2 patients (28.6%), and white matter disease and dysmyelinating disorders in one patient (14.3%).

A total of seven individuals were diagnosed with sinusitis, with three of them exhibiting central vestibular dysfunction based on the results of vestibular function tests. The remaining four patients displayed peripheral vestibular dysfunction. Prior research has shown that MRI test results assured the presence of sinusitis at a rate of 26.6% from the total sample of patients whom diagnosed with positive VNG tests (Kadri et al., 2019). Previous research, on the other hand, has indicated that MRI has a high potential for diagnostic certainty and reproducibility (Chua et al., 2021).

Two patients were diagnosed with labyrinthitis in this study, as previous research found that IAC imaging using MRI sequences such as FLAIR, T2-weighted, T1-weighted with enhancement, and high resolution T2-weighted had a sensitivity of 87% and a specificity of 100% for detecting labyrinthitis (Benson et al., 2020). While vestibular function testing were able to detect these two cases of labyrinthitis, the results revealed central dysfunction, despite the fact that earlier research had defined labyrinthitis as a peripheral illness at VNG test (Kamath et al., 2015).

Platzek et al. (2014) conducted a study that showed that multiparametric MRI exhibits a notable level of sensitivity and diagnostic accuracy when employed for the evaluation of suspected mastoiditis (Platzek et al., 2014). In contrast, our findings indicate that mastoiditis cases are identified based on the results of MRI examinations, whereas vestibular function tests reveal the presence of peripheral vestibular dysfunction.

The presence of cholesteatoma, as indicated by MRI, has been associated with central vestibular impairment in a single case. Prior research has demonstrated that MRI exhibits a sensitivity ranging from 91% to 94%, specificity ranging from 88% to 100%, and accuracy ranging from 92% to 95% when evaluating recurrent lesions (Durisin et al., 2010),(Gouda et al., 2018), (Foti et al., 2019). A prior study identified many MRI sequences that are valuable for the diagnosis of cholesteatomas, including DWI, T1-weighted, and T2-weighted imaging (Benson et al., 2020).

The vestibular function test (VNG/PTA) characterized the empty sella turcica disease as a central vestibular dysfunction in one clinical condition and as a peripheral vestibular

dysfunction in another. This demonstrates that the vestibular function test (VNG/PTA) could not distinguish whether the empty sella turcica disease was a central or peripheral source of the vestibular dysfunction. A previous study, on the other hand, indicated that the importance of the MRI finding of the empty sella turcica can be evaluated by combining clinical and imaging findings (Asokan et al., 2021).

The vestibular function test (VNG/PTA) results revealed that the two patients with microvascular disease had central vestibular dysfunction, whereas the other condition was peripheral auditory dysfunction. This is the same diagnosis as the two individuals whose MRIs revealed white matter disease and dysmyelinating diseases and vestibular function test (VNG/PTA) unable to determine if these diseases are central or peripheral causes for vestibular dysfunction. As reported in previous studies, the MRI can detect abnormalities in white mater (Datar et al., 2018). The latest advancements in MRI technology have enabled clinical neuroimaging and distinguishing various cerebrovascular diseases (Li et al., 2023).

Measurements of the affected nerve and comparisons with normal diameters are crucial to assess the thickening or atrophy of nerves in specific illnesses. These measurements also help determine the reference diameter value of VCN. Three radiologists' VCN diameter values for 3D FIESTA or 3D DRIVE measurements at 1.5T were provided in this study. Furthermore, there was a strong association between the cross sectional area (CSA) computed from the reconstructed sagittal MR images on the patient's MR images and the actual mean diameter (Table 20).

Table 20: Measurements of the nerve length, cross sectional area, cross sectional area for positive cases, and cross sectional area for negative cases.

		Nerve length in mm	CSA for all cases in mm^2	CSA for positive cases in mm^2	CSA for negative cases in mm^2
N	Valid	42	42	21	21
	Missing	7	7	28	28
Mean		19.02	1.50	1.58	1.43
Std. Deviation		2.83	0.47	0.49	0.45
Variance		7.99	0.22	0.24	0.21
Minimum		6.38	0.63	0.63	0.65
Maximum		23.77	2.67	2.67	2.28

Many institutions should be able to assess VCN diameter using 3D-DRIVE because it is often used in clinical practice. Furthermore, gadolinium contrast agents are not needed for assessing nerve diameter on 3D-DRIVE non-contrast, which permits the evaluation of VCN in patients with a history of allergies or impaired renal function without running the risk of nephrogenic systemic fibrosis (NSF). The VCN length was measured by three observers from the orifice of the porus acusticus internus to the termination of the cochlear nerve. The mean values for VCN length were 19.02mm (Figure 42), cross sectional area 1.50mm^2 (Figure 43), cross sectional area for positive cases 1.58mm^2 (Figure 44), and cross sectional area for negative instances 1.43mm^2 (Figure 45). A previous study, on the other hand, found that the CSA value for CN is 1.07±0.30 mm^2, which is less than in our study. The CSA of the VCN was higher than the CSA of the CN because the CN is a branch of the VCN. Our study and the previous one are comparable, but ours measured the CSA of the VCN and theirs measured the CSA of the CN. (Nakamichi et al., 2013).

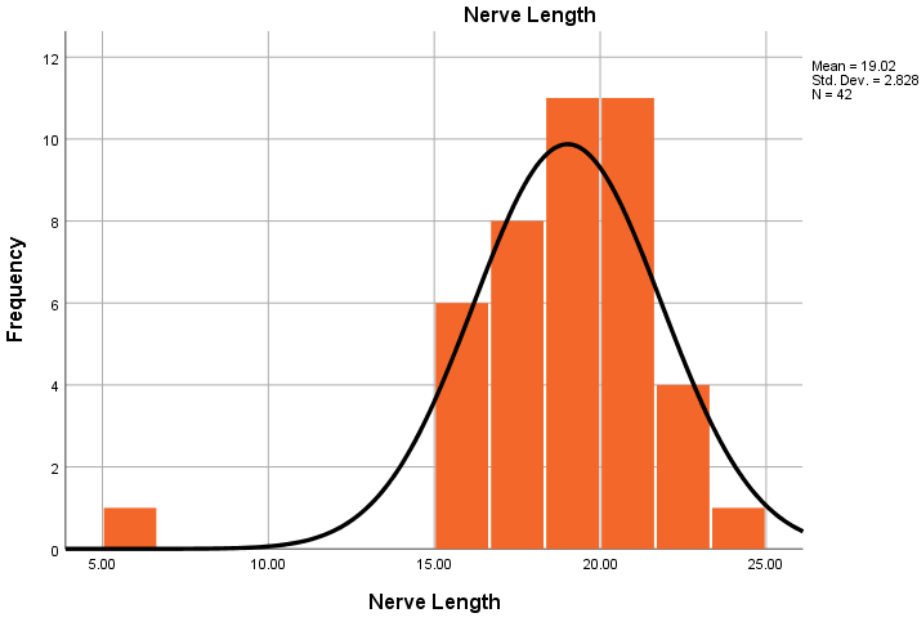

Figure 42. A bar chart displays the sample's nerve length data.

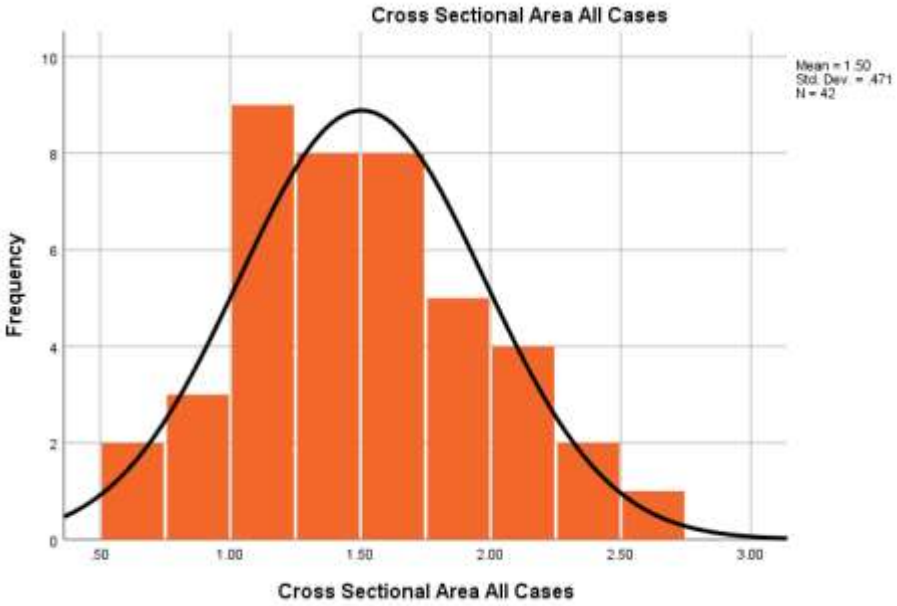

Figure 43. A bar chart displays the sample's cross sectional area (CSA) data.

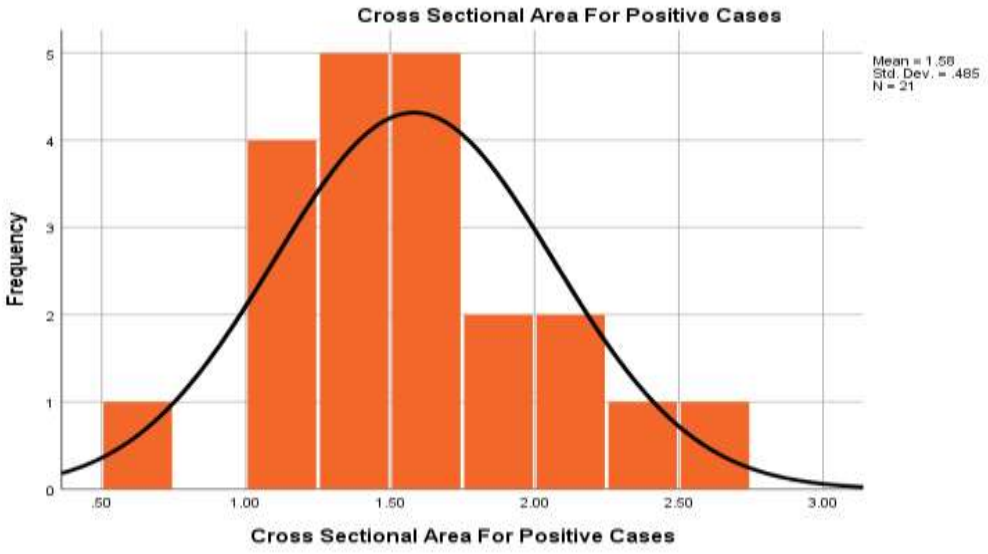

Figure 44. A bar chart displays the sample's CSA for positive cases data.

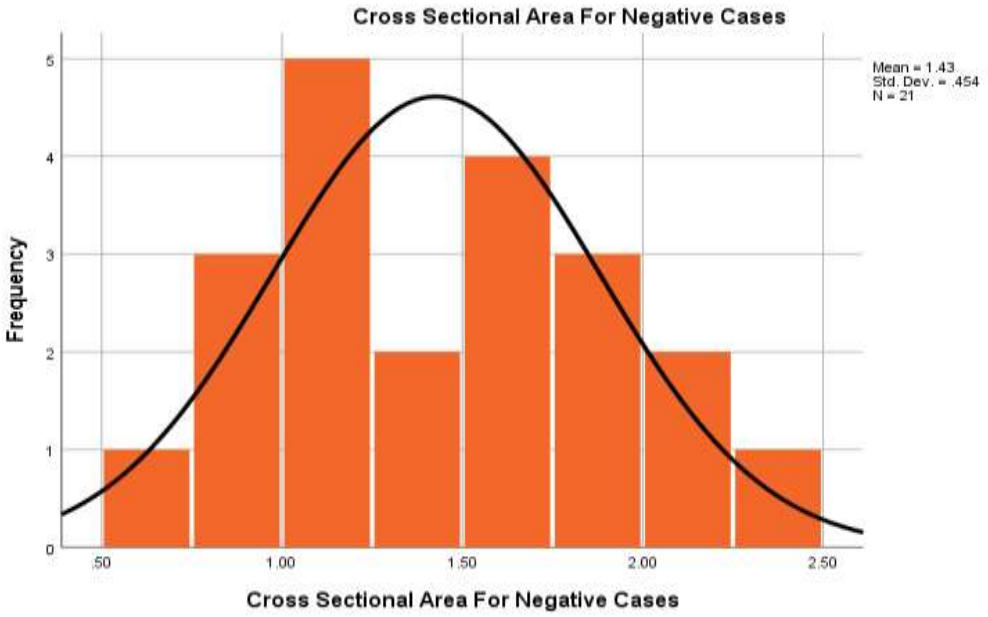

Figure 45. A bar chart displays the sample's CSA for negative cases data.

When compared to ears with normal hearing, Taydaş et al. identified a reduced cochlear nerve (CN) surface area in patients with idiopathic hearing loss and loss owing to a connexin26 gene mutation (TAYDAŞ & İNAN, 2019). In this study, we found that cases with positive test results had a higher CSA of the VCN than negative instances, which are healthy ones. Patients with microvascular disease had the highest CSA of 1.89mm², followed by those with right side infarction at 1.88mm², as shown in Figure 46.

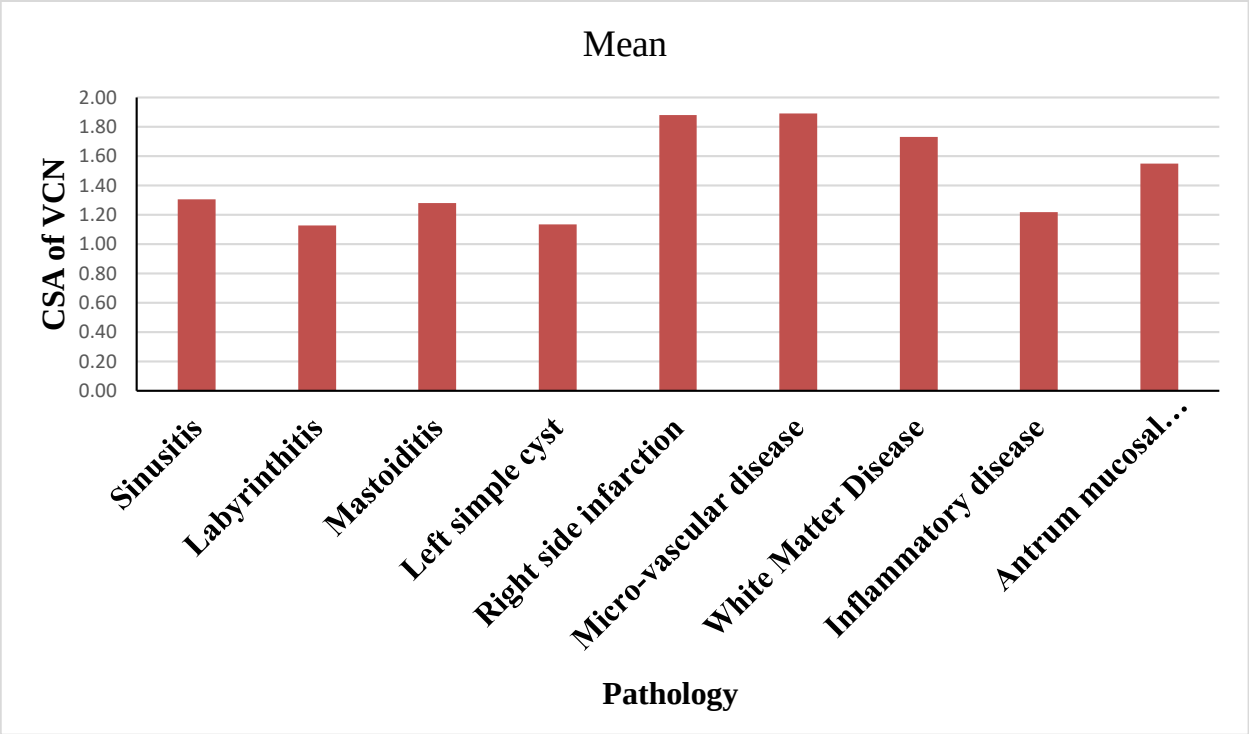

Figure 46. Displays the CSA measurements of the VCN in MR images of patients.

To determine the image quality of the different MRI sequences used by the two vendors (GE Healthcare/ Philips Healthcare) by quantifying the image quality metrics (IQM), including SNR and CNR for different sequences used in imaging the patients. The measured SNR and CNR for brain tissues from MR imaging obtained by GE Healthcare and Philips Healthcare

that use different coils were different form sequence to another as shown in the result. SNR depicts the relationship between the true and anticipated images.

In this study, an evaluation of GE Healthcare sequences in comparison with Philips Healthcare sequences was performed in a water phantom using the same sequences used for imaging the patients. All examinations were performed using GE MEDICAL SYSTEMS - Brivo MR355 1.5T MRI. In a water phantom (TLT Head Sphere Phantom for GE Closed MRI) study, the imaging parameters of the 3D-FIESTA sequence were TR of 7 ms, TE of 250 ms, slice thickness (ST) of 1mm, FOV of 20cm, flip angle of 65, and matrix size of 320 X 320. Imaging parameters for T2-FSE used the following parameters: TR 3173ms; TE 95ms; ST 2.5mm; slice gab 0.3mm; FOV 18 cm; flip angle 160; matrix size 288X280.

All examinations were performed using Philips Medical Systems -Ingenia 1.5T MRI. In a water phantom (Philips MRI Phantom Bottle 3000 cc) study, imaging parameters of the T2-FFE sequence were TR of 3000–5000ms, TE of 100ms, slice thickness (ST) of 5mm, FOV of 230mm, flip angle 90, and matrix size 560X560. Imaging parameters for B_FFE used the following parameters: TR 7.1ms; TE 3.5ms; ST 1.1mm; slice gab 0.5mm; FOV 160mm; flip angle 60; matrix size 380X380.

As defined in this study methodology, the SNR in patients' MRI exams was defined as the signal intensity (SI) of the average signal in a limited region of interest (ROI) of VCN tissue within the merged images divided by noise or the standard deviation (SD) of image differences from the same ROI. In addition, the CNR was defined in patients' MRI

examinations as the signal intensity SI(n) of the nerve area (n) minus the SI(b) of the brain region (b) divided by background noise.

The research inspected the quality indicators for the scanned phantom on GE Healthcare. The coronal-T1-FSE-Thin sequence had the highest SNR value, at 85.97 decibel (dB), while T2-FSE-Thin and 3D-FIESTA were 47.23 dB and 32 dB, respectively as shown in Table 11, and the STIR sequence had the highest CNR value, at 28.16 dB, while coronal T2-FSE-Thin was 1.2 dB as Table 13. illustrates. The quality metrics for the imaged phantoms utilized in Philips Healthcare have a higher SNR value for T2-FFE, which is 162.97dB, and a value of 38.12 dB for B-FFE-150 slices "Table 12"; in contrast, FLAIR-Long TR has the highest CNR value, which is 27.59 dB , see Table 14. for details.

The study's findings suggest that when the 3D-FIESTA sequence was utilized for vivo imaging, the GE Healthcare MRI had the best signal-to-noise ratio (SNR), with an SNR value of 11.21 dB "Table 15". The T2-FSE sequence, on the other hand, generated the highest contrast-to-noise ratio (CNR) result, measuring 161.32 dB as shown in Table 16. With an SNR of 17.36 dB, the Philips Healthcare MRI scanner produced the greatest signal-to-noise ratio (SNR) rating when using the T1-FFE sequence, as Table 13. illustrates.. The FIESTA sequence, on the other hand, has the highest contrast-to-noise ratio (CNR) rating, measuring 322.26 dB, refer to Table 14. for details.

The phantom SNR values were compared to those obtained from patients (in vivo). Figure 47 illustrates the findings, which indicate that SNR measurements for patients (in vivo) utilizing the same sequences are lower than those for the phantom. Figure 48 also compares

the CNR values for phantoms and people (in vivo), as well as the results obtained when imaging with GE Healthcare MRI equipment and Philips Healthcare MRI equipment. Table 21 shows SNR and CNR measurements for GE Healthcare phantoms and patients, while Table 22 shows SNR and CNR values for Philips Healthcare which corresponds to the same sequences done for both phantoms and patients.

Table 21: The SNR and CNR measurements obtained from the phantom and from the patients (in vivo) by using GE Healthcare MRI.

Sequence IQM	GE Healthcare in vivo		GE Healthcare phantom	
	SNR (dB)	CNR (dB)	SNR (dB)	CNR (dB)
Cor T1FSE (Thin)	3.86	45.93	85.97	5.18
STIR	3.81	57.71	55.17	28.16
ADC	2.54	2.01	27.83	0.34
3D_FIESTA	11.21	51.44	31.99	0.48
DWI 2MM	4.27	83.90	59.21	6.99
Cor T2FSE (Thin)	2.91	161.32	47.23	1.19

Table 22: The SNR and CNR measurements obtained from the phantom and from the patients (in vivo) by using Philips Healthcare MRI.

Sequence IQM	Philips Healthcare in vivo		Philips Healthcare phantom	
	SNR (dB)	CNR (dB)	SNR (dB)	CNR (dB)
T1W_SE	8.63	138.12	154.16	12.56
FLAIR_LongTR	4.13	68.16	129.06	27.59
T2W_3D_DRIVE	5.35	88.78	53.12	0.79
B_FFE_150 Slices	4.58	112.06	38.12	12.88
DWI 2MM	3.04	325.82	20.79	11.03
T1W_FFE	17.36	133.27	162.97	7.76

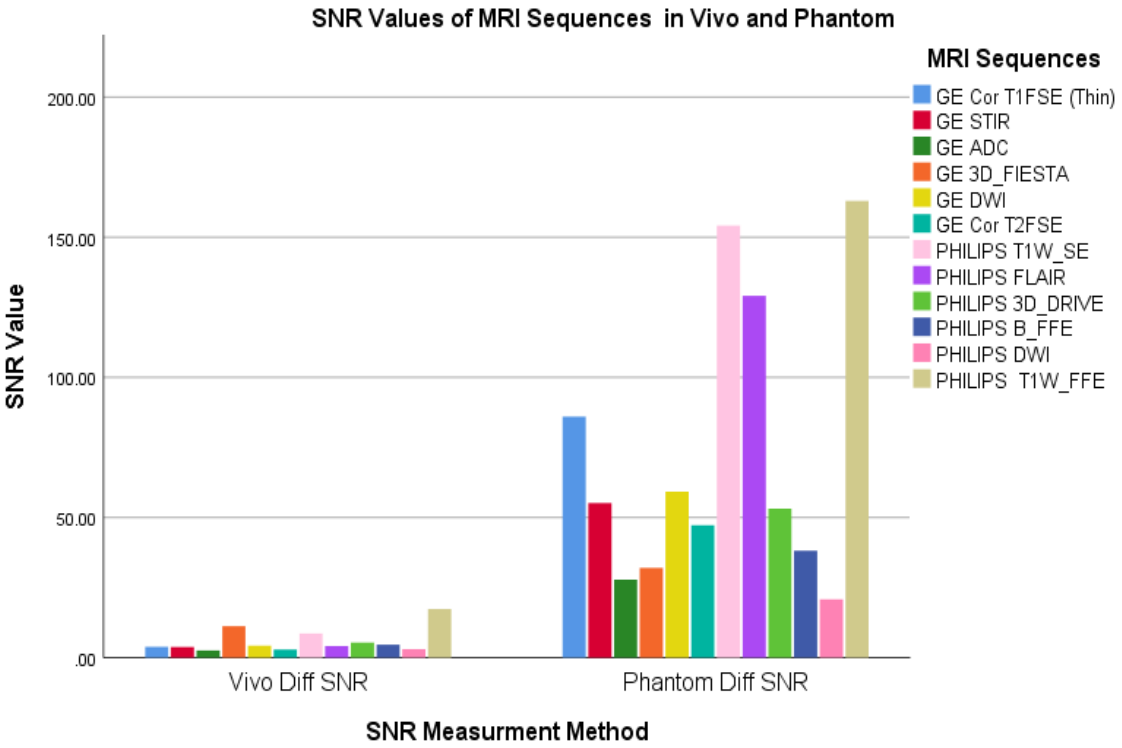

Figure 47. The bar chart illustrates the SNR measurements acquired from the phantom and patients (in vivo) utilizing the difference method in measuring SNR.

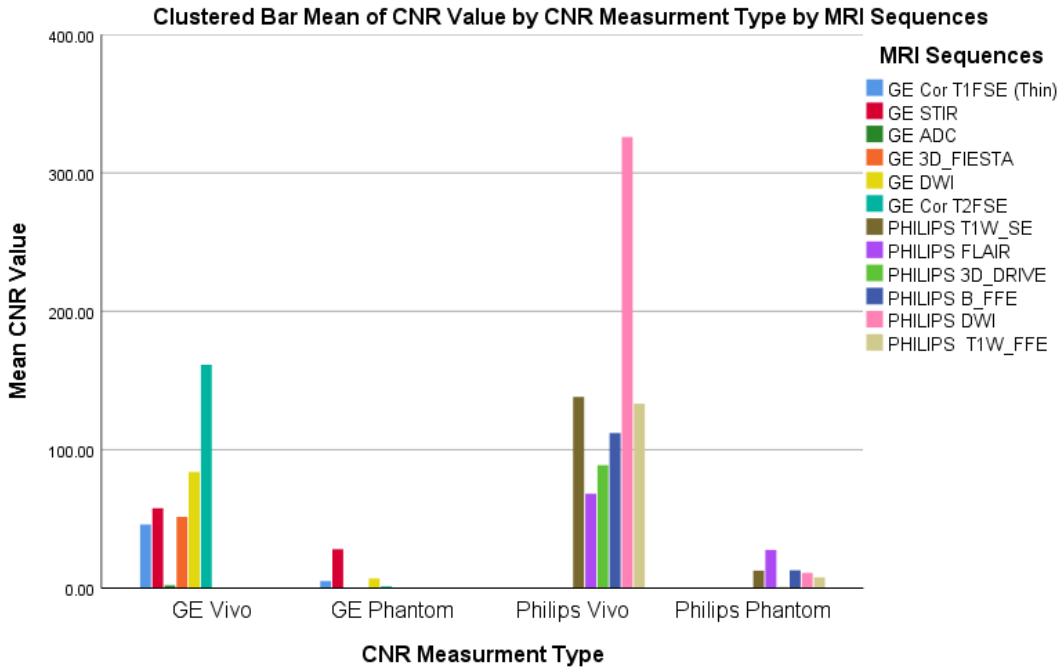

Figure 48. The bar chart illustrates the CNR measurements (in dB unit) acquired from the phantom and patients (in vivo) utilizing GE Healthcare and Philips Healthcare devises.

The contrast-to-noise ratio (CNR) of an image is influenced by both intrinsic and extrinsic characteristics. However, when T2-weighted imaging is utilized, the CNR tends to increase. It is important to note that T2-weighted imaging does have a drawback in that it typically exhibits poorer signal-to-noise ratio (SNR). In contrast, the SNR is influenced by several factors, including the repetition time (TR), echo time (TE), magnetic field strength, number of signal averages (NSA), coil type, receiving bandwidth, and voxel volume (Westbrook & Talbot, 2018). This requires future studies to compare the SNR of the imaging sequences used to image IAC, taking into account the factors that affect it, and that we could not control these parameters, since this study is retrospective.

The inner ear and VCN disease identification is improved by the heavily T2-weighted signals that are acquired through the use of fast spin-echo or gradient-echo sequences (Casselman et al., 1993), (Hermans et al., 1997), (Allen et al., 1996). Magnetic susceptibility can be detected in a 3D constructive interference in steady state (CISS) FIESTA GE Healthcare sequence, particularly in the temporal bone region where tiny soft tissue structures connect with the surrounding bone and ear. The DERIVE sequence's several closely spaced 90-degree refocusing pulses make it less susceptible to the local magnetic field's inhomogeneity (Iwayama et al., 1999), (Naganawa et al., 1996), (Mamata et al., 1998).

In this study the better sequences for getting a high SNR and CNR in Philips Healthcare were TI –FFE and FIESTA respectively, but in GE Healthcare MRI the better sequences for getting a high SNR and CNR were 3D FIESTA and T2-FSE respectively. Also the previous study reported that the T2-FSE sequence has high resolution and is helpful in the assessment of IAC because it utilizes the intrinsic tissue contrast of the fluid-filled IAC and membranous labyrinth (Davidson, 2001). Another previous study reported that the 3D DRIVE imaging technique exhibits superiority over the 3D balanced fast field echo (B-FFE) method for assessing the anatomical features within the inner ear (Jung et al., 2007).

The viewing of minute structures in the inner ear is made possible by the 3D-FSE's high-resolution, highly T2-weighted contrast. Moreover, CSF flow artifacts which are noticeable on the 2D-FSE are diminished by the 3DFSE procedure (Bassi et al., 1990). The 3DFSE sequence's comparatively lengthy scan time is a drawback. In order to force the remaining transverse magnetization back toward the longitudinal axis, a series of recovery pulses are

applied at the conclusion of the echo train in the 3D-DRIVE, which is based on a 3DFSE sequence (Oshio et al., 1998).

When compared to 3D-FSE, 3D-DRIVE can produce high-resolution, heavily T2-weighted images with a shorter scan time. It can also produce detailed reconstructed images of the inner ear or IAC, such as maximum intensity projection (MIP) images, with a shorter scan time. These images improve our comprehension of inner ear anatomy and the assessment of cochlear implantation. Visualizing the relationships between the cranial nerves and vessels at the IAC is made possible by the 3D-DRIVE sequences, which is beneficial for diagnosing neurovascular compression. The reduction of CSF signal intensity, particularly in the basilar artery, is a disadvantage of 3D-DRIVE sequencing (Nakashima et al., 2002).

5.1 Results of Hypothesis of the Study

Hypothesis: The diagnosis and assessment of vestibulocochlear nerve in patients with vestibular disorders whom had magnetic resonance imaging (MRI), more accurate and effective than the diagnosis with just videonystagmography (VNG) test, and pure-tone audiometry (PTA) tests.

To test the hypothesis, the interclass correlation coefficient (ICC) test was used to examine the consistency or repeatability between the observers diagnoses of the MRI images of the participants in this study, and the result was that the consistency or repeatability equaled 0.573, as shown in Table 8, and this result value was in the range of 0.40 to 0.59, indicating fair inter-rater agreement. That is, there are no significant differences in the three radiologists'

diagnoses of the MRI examination information provided. Table 9 and Figure 14 indicate the diseases diagnosed and their percentages.

Table 19 shows the findings of another analytical statistical examination, the crosstabulation test for vestibular function tests (VNG/PTA) and MRI radiologist diagnosis. The results of this test are explained by the results of the vestibular function tests (VNG and PTA), which demonstrated that 58.8% of people had central vestibular dysfunction and 41.2% had peripheral vestibular dysfunction. The diagnostic results of the diseases obtained from the patients' MRI images were compared to the results of the vestibular function tests (VNG and PTA) examinations, and the results revealed that the hearing function tests could determine whether the patient had a peripheral or central problem, whereas the MRI could determine the type of disease. It was used in conjunction with VNG examinations because VNG alone could not ascertaine the diagnoses of the nerve disorders in patients with vestibular disorders. So the diagnosis and assessment of vestibulocochlear nerve in patients with vestibular disorders whom had Magnetic Resonance Imaging (MRI), more accurate and effective than the diagnosis with just videonystagmography (VNG) test, and Pure-Tone Audiometry (PTA) tests.

Magnetic resonance imaging (MRI) can be used to measure the vestibulocochlear nerve and its branches in patients with vestibular disorders. As illustrated in Tables 10 and 20, these measurements can reveal a lot about the nerve. This is critical for determining which disorders impact the vestibulocochlear nerve (VCN). The measurements for the normal (negative) and abnormal (positive) samples were compared using Figures 42, 43, 44, and 45.

However, nerve measures are not available in vestibular functional tests (VNG/PTA). As a result, MRI is thought to be superior in this sector.

Tables 15 and 16 and Figures 36 and 37 provide SNR and CNR measurements for all cases on the GE Healthcare systems, as well as for all imaging sequences used. SNR and CNR measurements were also taken for all instances imaged on Philips Healthcare systems, as well as for all imaging sequences used. As seen in Tables 17 and 18, as well as Figures 38 and 39, the contrasts between them are depicted in Figure 40. The findings of the SNR and CNR measures vary between vendors, as did the results of the measurements for the imaging sequences employed for one patient. A future study is needed to find the ideal sequence parameter to offer a high diagnostic value for the vestibulocochlear nerve in each vendor or manufacturer that performs the best sequence for imaging IAC.

5.2 Study Limitations

One limitation of the present study is its reliance on a retrospective sample of medical cases, which prevented any adjustments to the imaging protocols used. The collection of a substantial quantity of samples was hindered due to the criteria for sample selection, specifically that patients must have undergone both an MRI and an vestibular function test (VNG/PTA) evaluation. Furthermore, the study sample consisted exclusively of individuals whom have positive results of the vestibular function tests (VNG/PTA) evaluation, hence limiting our ability to assess the sensitivity and specificity of MRI in comparison to the vestibular function tests (VNG/PTA).

5.3 Future Research

Future studies, including larger sample size to quantify SNR and CNR, including correlation between two acquisitions of the same MRI sequence with different parameters. In addition to having the opportunity to study the specificity and sensitivity of MRI and vestibular function tests among the different vestibular disorders and the other intracranial diseases, which may affect the results of VNG and other vestibular function tests.

Chapter 6. Conclusion

This study addressed the diverse role of MRI in the diagnosis of vestibulocochlear nerve diseases, and aimed to reveal the effectiveness of MRI as a diagnostic tool compared with vestibulometric tests mainly VNG result, and other allied vestibular tests as PTA, through a detailed analysis of the radiologist's diagnostic report and vestibulocochlear nerve diameter measurements. This study focused on evaluating the image quality of different MRI sequences of two different vendors, using image quality metrics (IQM) such as signal-to-noise ratio (SNR) and contrast-to-noise ratio (CNR).

The radiologist's diagnostic report including VCN diameter measurements' highlighted the importance of MRI in detecting and characterizing vestibulocochlear nerve disease. Comparison of MRI and vestibule-metric tests results provided valuable insight into the complementarity of these diagnostic modalities and highlighted the importance of a comprehensive and integrated approach for accurate diagnosis. Videonystagmography (VNG) remains a crucial tool within the etiologic diagnosis of patients complaining of vertigo, even within the post-MRI period.

In summary, this study contributes to the existing body of knowledge by providing a comprehensive examination of the role of MRI in the diagnosis of vestibulocochlear nerve diseases. Integrating radiologist reports of vestibulocochlear nerve diameters' measurements indicated that parasagittal high resolution T2 weighted (DRIVE, CISS, and FIESTA) MRI could be used to measure the vestibulocochlear nerve.

VCN thickness in patients, who had positive MRI results, is significantly thicker in cross-sectional surface area of the vestibulocochlear nerve than patients with normal diagnoses, and MRI is indisputably the examination of choice for recognizing the morphology, characteristic, classification and topography of VCN disorders. In addition, the most MRI diagnosed disorders matched the central vestibular dysfunction on VNG test results.

Vestibular function tests are still a crucial tool for screening and the initial diagnosis tool of vestibular disorders; however, they are restricted to some extent in a whole contribution to the diagnosis disease etiology of such patients. Because of these perceptions, we ought to re-evaluate the diagnostic significance of VNG, and reestablish it to its legitimate put within the schedule demonstrative evaluation of vertigo and unsteadiness.

The results of this research will impact both clinical practice and continued efforts to advance imaging technology, ultimately benefiting patients through improved diagnostic accuracy and quality of treatment. The results showed measured SNR by estimating the foreground and background of all output sequences. These results may have important implications for future comparisons of different conventional and parallel image reconstruction methods used in different clinical and methodological studies.

We found that better sequences for getting high SNR and CNR in Philips were TI –FFE and FIESTA respectively, and in GE Healthcare MRI the sequences that had highest SNR and CNR were 3D FIESTA and T2-FSE respectively, providing comparable image quality along with excellent diagnostic capabilities for radiologists.

T2-FSE sequences have high resolution which is helpful in assessment of IAC, and that 3D DRIVE exhibits superiority over B-FFE for assessing anatomical features of the inner ear and demonstrates relationships between the cranial nerves and vessels at IAC and diagnosing neurovascular compression . Viewing of minute structures in the inner ear is made possible by 3D-FSE's high-resolution, highly T2-weighted contrast. When compared to 3D-FSE, 3D-DRIVE can produce high-resolution, heavily T2-W images with a shorter scan time. These images improve comprehension of inner ear anatomy and the assessment of vestibulocochlear pathology.

Accordingly the following sequences: T1-weighted, T2 weighted, DWI, FLAIR, DRIVE, CISS, and FIESTA sequences are required to be comprehend in MRI protocols in order to manifest different anatomical structures and pathologies of vestibulocochlear nerve and other surrounding soft tissue. Performing these sequences, confirm the vestibular function test results and differentiating vestibular disorders from other pathologies.

References

Allen, R. W., Harnsberger, H. R., Shelton, C., King, B., Bell, D., Miller, R., Parkin, J., Apfelbaum, R., & Parker, D. (1996). Low-cost high-resolution fast spin-echo MR of acoustic schwannoma: an alternative to enhanced conventional spin-echo MR? *American journal of neuroradiology, 17*(7), 1205-1210.

Asokan, M., Avantsa, R., & Anchan, A. (2021). MRI Evaluation of Patients with Empty Sella--A Retrospective Study KS Hegde Medical Academy, Mangalore. *Journal of Evolution of Medical and Dental Sciences, 10*(34), 2879-2884.

Bassi, P., Piazza, P., Cusmano, F., Menozzi, R., Gandolfi, A., & Zini, C. (1990). MR cisternography of the cerebello-pontine angle and internal auditory canal in diagnosis of intracanalicular acoustic neuroma. *Neuroradiology, 31*, 486-491.

Benoudiba, F., Toulgoat, F., & Sarrazin, J.-L. (2013). The vestibulocochlear nerve (VIII). *Diagnostic and interventional imaging, 94*(10), 1043-1050.

Benson, J. C., Carlson, M. L., & Lane, J. I. (2020). MRI of the internal auditory canal, labyrinth, and middle ear: how we do it. *Radiology, 297*(2), 252-265.

Casselman, J. W., Kuhweide, R., Deimling, M., Ampe, W., Dehaene, I., & Meeus, L. (1993). Constructive interference in steady state-3DFT MR imaging of the inner ear and cerebellopontine angle. *American journal of neuroradiology, 14*(1), 47-57.

Casselman, J. W., Offeciers, F. E., Govaerts, P. J., Kuhweide, R., Geldof, H., Somers, T., & D'Hont, G. (1997). Aplasia and hypoplasia of the vestibulocochlear nerve: diagnosis with MR imaging. *Radiology, 202*(3), 773-781.

Chua, E., Navaratnam, A. V., St Leger, D., Lam, V., Unadkat, S., & Weller, A. (2021). Comparison of MRI and CT in the evaluation of unilateral maxillary sinus opacification. *Radiology Research and Practice, 2021*.

Ciftci, E., Anik, Y., Arslan, A., Akansel, G., Sarisoy, T., & Demirci, A. (2004). Driven equilibrium (drive) MR imaging of the cranial nerves V–VIII: comparison with the T2-weighted 3D TSE sequence. *European journal of radiology, 51*(3), 234-240.

Dalaqua, M., Nascimento, F. B. P. d., Miura, L. K., Reis, F., Garcia, M. R. T., & Barbosa Júnior, A. A. (2021). Magnetic resonance imaging of the cranial nerves in congenital, traumatic, and vascular diseases: a pictorial essay. *Radiologia Brasileira, 54*, 185-192.

Datar, R., Prasad, A. N., Tay, K. Y., Rupar, C. A., Ohorodnyk, P., Miller, M., & Prasad, C. (2018). Magnetic resonance imaging in the diagnosis of white matter signal abnormalities. *The Neuroradiology Journal, 31*(4), 362-371.

Davidson, H. C. (2001). Imaging evaluation of sensorineural hearing loss. Seminars in Ultrasound, CT and MRI,

De Foer, B., Kenis, C., Van Melkebeke, D., Vercruysse, J.-P., Somers, T., Pouillon, M., Offeciers, E., & Casselman, J. W. (2010). Pathology of the vestibulocochlear nerve. *European journal of radiology, 74*(2), 349-358.

Durisin, M., Bartling, S., Arnoldner, C., Ende, M., Prokein, J., Lesinski-Schiedat, A., Lanfermann, H., Lenarz, T., & Stöver, T. (2010). Cochlear osteoneogenesis after meningitis in cochlear implant patients: a retrospective analysis. *Otology & Neurotology, 31*(7), 1072-1078.

El Sadik, A., & Shaaban, M. (2017). The relationship between the dimensions of the internal auditory canal and the anomalies of the vestibulocochlear nerve. *Folia morphologica, 76*(2), 178-185.

Erkoç, M. F., Imamoglu, H., Okur, A., Gumus, C., & Dogan, M. (2012). Normative size evaluation of IAC with MRI: review of 3786 patients. *Folia morphologica, 71*(4), 217-220.

Fife, T., Tusa, R., Furman, J., Zee, D. S., Frohman, E., Baloh, R., Hain, T., Goebel, J., Demer, J., & Eviatar, L. (2000). Assessment: vestibular testing techniques in adults and children: report of the Therapeutics and Technology Assessment Subcommittee of the American Academy of Neurology. *Neurology*, *55*(10), 1431-1441.

Foti, G., Beltramello, A., Minerva, G., Catania, M., Guerriero, M., Albanese, S., & Carbognin, G. (2019). Identification of residual–recurrent cholesteatoma in operated ears: diagnostic accuracy of dual-energy CT and MRI. *La radiologia medica*, *124*, 478-486.

Frotscher, M. (2005). *Duus' topical diagnosis in neurology: anatomy, physiology, signs, symptoms*. Thieme.

Gheorghe, L., Negru, D., Cobzeanu, M. D., Palade, O. D., Botnariu, E. G., Cobzeanu, B. M., & Cobzeanu, M.-L. (2022). The Diagnostic Accuracy of Pure-Tone Audiometry Screening Protocols for Vestibular Schwannoma in Patients with Asymmetrical Hearing Loss—A Systematic Review and Meta-Analysis. *Diagnostics*, *12*(11), 2776.

Gouda, M., Nasr, W. F., Abd Elbary, M. E.-S., & Razek, M. M. (2018). MRI as an alternative to second look mastoid surgery. *Indian Journal of Otolaryngology and Head & Neck Surgery*, *70*, 410-414.

Heine, C., Kingebiel, R., & Lehmann, R. (2002). Three-dimensional MR visualization of the intracisternal course of the cranial nerves V–VIII by virtual cisternoscopy. *Acta Radiologica*, *43*(3), 242-248.

Henneberger, A., Ertl-Wagner, B., Reiser, M., Gürkov, R., & Flatz, W. (2017). Morphometric evaluation of facial and vestibulocochlear nerves using magnetic resonance imaging: comparison of Menière's disease ears with normal hearing ears. *European Archives of Oto-Rhino-Laryngology*, *274*, 3029-3039.

Hermans, R., der Goten, A. V., Foer, B. D., & Baert, A. (1997). MRI screening for acoustic neuroma without gadolinium: value of 3DFT-CISS sequence. *Neuroradiology, 39*, 593-598.

Iwayama, E., Naganawa, S., Ito, T., Fukatsu, H., Ikeda, M., Ishigaki, T., & Ichinose, N. (1999). High-resolution MR cisternography of the cerebellopontine angle: 2D versus 3D fast spin-echo sequences. *American journal of neuroradiology, 20*(5), 889-895.

Jung, N. Y., Moon, W.-J., Lee, M. H., & Chung, E. C. (2007). Magnetic resonance cisternography: comparison between 3-dimensional driven equilibrium with sensitivity encoding and 3-dimensional balanced fast-field echo sequences with sensitivity encoding. *Journal of computer assisted tomography, 31*(4), 588-591.

Kadri, İ., Söylemez, E., Yilmaz, N., & Eshraghi, A. A. (2019). Association Between Chronic Rhinosinusitis and The Vestibular System. *ENT updates, 9*(2), 133-137.

Kamath, M. P., Shenoy, S. V., Sreedharan, S., Bhojwani, K., Mammen, S. S., & Majeed, N. A. (2015). Role of electronystagmography in balance disorders: A clinical study. *Indian Journal of Otology, 21*(3), 201-208.

Khan, S., & Chang, R. (2013). Anatomy of the vestibular system: a review. *NeuroRehabilitation, 32*(3), 437-443.

Kim, H.-S., Kim, D.-I., Chung, I.-H., Lee, W.-S., & Kim, K.-Y. (1998). Topographical relationship of the facial and vestibulocochlear nerves in the subarachnoid space and internal auditory canal. *American journal of neuroradiology, 19*(6), 1155-1161.

Lanfermann, H., Raab, P., Kretschmann, H.-J., & Weinrich, W. (2019). Cranial neuroimaging and clinical neuroanatomy: atlas of MR imaging and computed tomography. *(No Title)*.

Li, X., Su, F., Yuan, Q., Chen, Y., Liu, C.-Y., & Fan, Y. (2023). Advances in differential diagnosis of cerebrovascular diseases in magnetic resonance imaging: a narrative review. *Quantitative Imaging in Medicine and Surgery, 13*(4), 2713.

Magnotta, V. A., Friedman, L., & BIRN, F. (2006). Measurement of signal-to-noise and contrast-to-noise in the fBIRN multicenter imaging study. *Journal of digital imaging, 19*, 140-147.

Mamata, Y., Muro, I., Matsumae, M., Komiya, T., Toyama, H., Tsugane, R., & Sato, O. (1998). Magnetic resonance cisternography for visualization of intracisternal fine structures. *Journal of neurosurgery, 88*(4), 670-678.

McCaslin, D. L. (2019). *Electronystagmography and Videonystagmography (Eng/Vng)*. Plural Publishing.

Moideen, A., Konkimalla, A., Tyagi, A. K., Varshney, S., Kumar, A., Jat, B., Prasath, R., & Yadav, M. C. (2023). Cross-Sectional Analysis of Videonystagmography (VNG) Findings in Balance Disorders. *Cureus, 15*(2).

Mumenthaler, M., Mattle, H., & Taub, E. (2006). The neurological examination. *Fundamentals of Neurology. Stuttgart: Georg Thieme Verlag*, 36.

Naganawa, S., Yamakawa, K., Fukatsu, H., Ishigaki, T., Nakashima, T., Sugimoto, H., Aoki, I., Miyazaki, M., & Takai, H. (1996). High-resolution T2-weighted MR imaging of the inner ear using a long echo-train-length 3D fast spin-echo sequence. *European radiology, 6*, 369-374.

Naguib, N. N., Hey, C., Shaaban, M. S., Elabd, A. M., Hassan, H. H., Gruber-Rouh, T., Kaltenbach, B., Harth, M., Ackermann, H., & Stöver, T. (2017). Assessment of the cochlear nerve to facial nerve size ratio using MR multiplanar reconstruction of the internal auditory canal in patients presenting with acquired long-standing hearing loss. *The British journal of radiology, 90*(1073), 20160870.

Nakamichi, R., Yamazaki, M., Ikeda, M., Isoda, H., Kawai, H., Sone, M., Nakashima, T., & Naganawa, S. (2013). Establishing normal diameter range of the cochlear and facial nerves with 3D-CISS at 3T. *Magnetic Resonance in Medical Sciences, 12*(4), 241-247.

Nakashima, K., Morikawa, M., Ishimaru, H., Ochi, M., Kabasawa, H., & Hayashi, K. (2002). Three-dimensional fast recovery fast spin-echo imaging of the inner ear and the vestibulocochlear nerve. *European radiology*, *12*, 2776-2780.

Netter, F.H., Atlas of neuroanatomy and neurophysiology. 2002.

Oshio, K., Williamson, D., Winalski, C., Miyamoto, S., Kosugi, S., & Suzuki, K. (1998). Fast recovery RARE for knee imaging. Proceedings of the sixth scientific meeting of ISMRM,

Platzek, I., Kitzler, H. H., Gudziol, V., Laniado, M., & Hahn, G. (2014). Magnetic resonance imaging in acute mastoiditis. *Acta Radiologica Short Reports*, *3*(2), 2047981614523415.

Pyykkö, I., Zou, J., Gürkov, R., Naganawa, S., & Nakashima, T. (2019). Imaging of temporal bone. *Vestibular Disorders, 82*, 12-31.

Reeder, S. B. (2007). Measurement of signal-to-noise ratio and parallel imaging. In *Parallel imaging in clinical MR applications* (pp. 49-61). Springer.

Sakata, M., Harada, K., Shirase, R., Kumagai, A., & Ogasawara, M. (2005). High-resolution MRI of the Labyrinth: Optimization of Scan Parameters with 3D-FSE. *Japanese Journal of Radiological Technology, 61*(7), 1040-1045.

Schulze, M., Reimann, K., Seeger, A., Klose, U., Ernemann, U., & Hauser, T. (2017). Improvement in imaging common temporal bone pathologies at 3 T MRI: small structures benefit from a small field of view. *Clinical Radiology, 72*(3), 267. e261-267. e212.

Shaabani, M. (2022). Hearing and Vestibular Testing in Menière's Disease.

Sheth, S., Branstetter IV, B. F., & Escott, E. J. (2009). Appearance of normal cranial nerves on steady-state free precession MR images. *Radiographics*, *29*(4), 1045-1055.

Simplification, H. A. (2006). Office of the Secretary 45 CFR Parts 160 and 164.

Steckner, M. C., Liu, B., & Ying, L. (2009). A new single acquisition, two-image difference method for determining MR image SNR. *Medical physics*, *36*(2), 662-671.

Strupp, M., Dlugaiczyk, J., Ertl-Wagner, B. B., Rujescu, D., Westhofen, M., & Dieterich, M. (2020). Vestibular disorders: diagnosis, new classification and treatment. *Deutsches Ärzteblatt International*, *117*(17), 300.

Swartz, J. D. (2008). Pathology of the vestibulocochlear nerve. *Neuroimaging Clinics of North America*, *18*(2), 321-346.

TAYDAŞ, O., & İNAN, H. C. (2019). Evaluation of Cochlear Nerve Scale with MRI in Patients with Idiopathic Unilateral Sensorineural Hearing Loss. *Sakarya Tıp Dergisi*, *9*(4), 639-643.

Toga, A. W. (2015). *Brain mapping: An encyclopedic reference*. Academic Press.

Westbrook, C. (2016). *MRI at a Glance*. John Wiley & Sons.

Westbrook, C., & Talbot, J. (2018). *MRI in Practice*. John Wiley & Sons.

Wu, W., Wu, F., Liu, D., Zheng, C., Kong, X., Shu, S., Li, D., Kong, X., & Wang, L. (2020). Visualization of the morphology and pathology of the peripheral branches of the cranial nerves using three-dimensional high-resolution high-contrast magnetic resonance neurography. *European journal of radiology, 132*, 109137.

List of Appendixes

Appendix 1: IRB Approval Letter

Arab American University- Palestine
Deanship of Scientific Research
IRB committee
Tel: 04-241-8888, ext 1196
E-mail: irb.aaup@aaup.edu

الجامعة العربية الامريكية فلسطين
عمادة البحث العلمي
لجنة اخلاقيات البحث العلمي
تلفون: 1196 ext 04-241-8888
البريد الالكتروني: irb.aaup@aaup.edu

IRB Approval Letter

Study Title: MRI Assessment of vestibulocochlear nerve disease diagnosed by Videonystagmography (VNG), and Pure-Tone Audiometry (PTA) Tests.

Submitted by: Mohammad Abdul khalik Abul Fattah Abdul Ghani

Date received: 22nd Jan 2023

Date reviewed: 15th Feb 2023

Date approved: 4th March 2023

Your Study titled "MRI Assessment of Vestibulocochlear nerve disease Diagnosed by Videonystagmography (VNG), and Pure-Tone Audiometry (PTA) Tests." With archived number **2023 /A /38 /N** was reviewed by the Arab American University IRB committee and was approved on 4th March 2023.

Reham Khalaf-Nazzal, MD, PhD
IRB committee chairman
Arab American University of Palestine

General Conditions:

1. Valid for 5 months from date of approval.
2. It is important to inform the committee with any modification of the approved study protocol.
3. The committee appreciates a copy of the research when accomplished.

Appendix 2: Letter to Health Care Providor

Arab American University
Ramallah Site

الجامعة العربية الأمريكية
موقع رام الله

January 17, 2023

To : Dr. Shadi Shalabi.

The Faculty of Graduate Studies at the Arab American University of Palestine certifies that **Mr. Mohammad Abdul Khalik Abdul Ghani** holding a student No. **(202112985)** is a student enrolled in the Masters of In Computed Tomography and MRI Sciences. Mr. Abdul Ghani is currently working on his master thesis entitled:

"MRI Assessment of Vestibulocochlear nerve disease Diagnosed by Videonystagmography (VNG), and Pure-Tone Audiometry (PTA) Tests., under the supervisors of Dr. Samer Mhanna And Dr. Jonathan McNulty

We appreciate your kind cooperation to Mr. Abdul Ghani help him obtain the necessary information needed for the study, noting that the information will be used for the purpose of research only and will de dealt with the utmost confidentiality.

This certificate was given upon his request.

Dean of Graduate Studies

Dr. Nouar Qutob

Appendix 3: Consented Data Usage Agreement

Arab American University
Scientific Research Deanship
Ethical Review Committee

الجامعة العربية الأمريكية
عمادة البحث العلمي
لجنة اخلاقيات البحث العلمي

Data Usage Agreement DUA

AAUP-IRB Code No.: 2023\A\38\N
AAUP-IRB Date: 4th March 2023

DATA USE AGREEMENT FOR LIMITED DATA SETS

This Data Use Agreement ("Agreement"), effective as of **Sunday, March 26, 2023** ("Effective Date"), is entered into by and between **Mohammed Abdalghani** ("Recipient") and **Dr. Shadi Shalabi** ("Covered Entity"). The purpose of this Agreement is to provide Recipient with access to a Limited Data Set ("LDS") for use in the following titled research project: **MRI Assessment of Vestibulocochlear nerve disease Diagnosed by Videonystagmography (VNG), and Pure-Tone Audiometry (PTA) Tests.** (Project Name) under the direct supervision of **Mohammed Abdalghani** (Principal Investigator) in accord with the HIPAA Regulations.

1. Definitions. Unless otherwise specified in this Agreement, all capitalized terms used in this Agreement not otherwise defined have the meaning established for purposes of the "HIPAA Regulations" codified at Title 45 parts 160 through 164 of the United States Code of Federal Regulations, as amended from time to time.

2. Preparation of the LDS. Covered Entity shall prepare and furnish to Recipient a LDS in accord with the HIPAA Regulations. **NOTICE: This agreement is valid only if the Data do not include any of the following "Prohibited Identifiers": Names; postal address information other than town, cities, states and zip codes; telephone and fax numbers; email addresses, URLs and IP addresses; social security numbers; certificate and license numbers; vehicle identification numbers; device identifiers and serial numbers; biometric identifiers (such as voice and fingerprints); and full face photographs or comparable images.**

3. Minimum Necessary Data Fields in the LDS. In preparing the LDS, Covered Entity or its Business Associate shall include the data fields specified by the parties from time to time, which are the minimum necessary to accomplish the purposes set forth in Section 5 of this Agreement.

4. Responsibilities of Recipient.

   Recipient agrees to:

   a. Use or disclose the LDS only as permitted by this Agreement or as required by law;

   b. Use appropriate safeguards to prevent use or disclosure of the LDS other than as permitted by this Agreement or required by law;

   c. Report to Covered Entity any use or disclosure of the LDS of which it becomes aware that is not permitted by this Agreement or required by law, including the presence of prohibited identifiers in the LDS;

d. Require any of its subcontractors or agents that receive or have access to the LDS to agree to the same restrictions and conditions on the use and/or disclosure of the LDS that apply to Recipient under this Agreement; and

e. Not use the information in the LDS, alone or in combination to identify or contact the individuals who are data subjects.

5. Permitted Uses and Disclosures of the LDS. Recipient may use and/or disclose the LDS only for the Research described in this Agreement or as required by law.

6. Term and Termination.

a. Term. The term of this Agreement shall commence as of the Effective Date and terminate 5 years from Effective Date. Should the Recipient desire to keep the LDS for a longer period, a justification in writing should be made to the Covered Entity.

b. Termination by Recipient. Recipient may terminate this agreement at any time by notifying the Covered Entity and returning or destroying the LDS.

c. Termination by Covered Entity. Covered Entity may terminate this agreement at any time by providing thirty (30) days prior written notice to Recipient.

d. For Breach. Covered Entity shall provide written notice to Recipient within ten (10) days of any determination that Recipient has breached a material term of this Agreement. Covered Entity shall afford Recipient an opportunity to cure said alleged material breach upon mutually agreeable terms. Failure to agree on mutually agreeable terms for cure within thirty (30) days shall be grounds for the immediate termination of this Agreement by Covered Entity.

e. Effect of Termination. Sections 1, 4, 5, 6(e) and 7 of this Agreement shall survive any termination of this Agreement under subsections c or d.

7. Miscellaneous.

a. Change in Law. The parties agree to negotiate in good faith to amend this Agreement to comport with changes in federal law that materially alter either or both parties' obligations under this Agreement. Provided however, that if the parties are unable to agree to mutually acceptable amendment(s) by the compliance date of the change in applicable law or regulations, either Party may terminate this Agreement as provided in section 6.

b. Construction of Terms. The terms of this Agreement shall be construed to give effect to applicable federal interpretative guidance regarding the HIPAA Regulations.

c. No Third Party Beneficiaries. Nothing in this Agreement shall confer upon any person other than the parties and their respective successors or assigns, any rights, remedies, obligations, or liabilities whatsoever.

d. Counterparts. This Agreement may be executed in one or more counterparts, each of which shall be deemed an original, but all of which together shall constitute one and the same instrument.

IN WITNESS WHEREOF, each of the undersigned has caused this Agreement to be duly executed in its name and on its behalf.

COVERED ENTITY

By: _____

Print Name: Dr. Shadi Shalabi

Print Title: Doctor

RECIPIENT

By: _____

Print Name: Mohammed Abdalghani

Print Title: Investigator

ملخص الدراسة

الأهداف والغايات

الغرض من هذه الدراسة هو دراسة دور وحساسية التصوير بالرنين المغناطيسي في تشخيص الاضطرابات الدهليزية، ومقارنة التصوير بالرنين المغناطيسي مع اختبار الوظيفة الدهليزية بما في ذلك اختبار قياس السمع ذو النغمة النقية، الذي له نتائج إيجابية وتم تشخيصه بواسطة اختبار الاضطراب الدهليزي.

تحديد جودة الصورة لتتابعات التصوير بالرنين المغناطيسي المستخدمة من قبل مقدمي الاجهزة الطبية عن طريق قياس جودة الصورة، بما في ذلك نسبة الإشارة إلى الضوضاء و نسبة التباين إلى الضوضاء وإجراء مقارنة بين التتابعات المختلفة.

المنهجية

شملت العينة 49 مريضاً تتراوح أعمارهم بين 7 - 77 سنة، 20 ذكراً و 29 أنثى. وقد خضع 32 مريضا لاختبارات الوظيفة الدهليزية، وكانت جميع نتائج الفحوصات المذكورة إيجابية, حيث قام ثلاثة من أخصائيي الأشعة بقراءة الفحوصات الإشعاعية لفحص التصوير بالرنين المغناطيسي للمرضى . بالإضافة إلى تسجيل قياسات قطر العصب الدهليزي. و تم حساب مقياس إحصائي للمتوسط، والانحراف المعياري، والمدى. التقارير التشخيصية للعصب الدهليزي القوقعي المحسوبة بواسطة الإرتباط داخل الفئة لجميع نتائج البيانات. تم قياس طول العصب القوقعي على تتابعات الصدى الميداني السريع والمتوازن والتصوير السريع باستخدام اكتساب الحالة الثابتة في كلا

الجانبين على الصورة المحورية، وتم قياس أقطارعلى الصورة السهمية المعاد تنسيقها والمتكونة من تتابع الزمن الأول الموزون للتوازن الموجه ثلاثي الابعاد لحساب مساحة المقطع العرضي.

تم إجراء قياس نسبة الإشارة إلى الضوضاء بطريقة الفرق لكل من الجسم الحي والوهمية، في حين تم حساب نسبة التباين إلى الضوضاء عن طريق تقدير نسبة متوسط الإشارة إلى الانحراف المعياري للخلفية التي تمثل الضوضاء.

نتائج تشخيص أطباء أخصائيي الأشعة:

أظهرت تقارير أخصائيي الأشعة وجود أمراض مختلفة في فحص التصوير بالرنين المغناطيسي، والتي تشكل 53.1% من جميع الحالات. و أظهرت نتائج اختبارات الوظيفة الدهليزية أن 58.8% بان لديهم خلل في العصب الدهليزي المركزي، و41.2% لديهم خلل في العصب الدهليزي الفرعي.

كانت القيم المتوسطة طول العصب الدهليزي هي 19.0187 ملم. متوسط المساحة المقطعية لجميع المرضى، الحالات الإيجابية، الحالات السلبية كانت 1.5044 ملم²، 1.5819 ملم²، 1.4271 ملم²، على التوالي.

قياس نسبة الإشارة إلى الضوضاء و نسبة التباين إلى الضوضاء في قياسات الفانتوم لتتابعات شركة جي اي GE ، يتمتع التتابع الإكليلي في الزمن الثاني الموزون للصدى سريع الدوران ذو السمك الرفيع بأعلى قيمة لنسبة الإشارة إلى الضوضاء 85.97 ديسيبل، و الإكليلي في الزمن الثاني الموزون للصدى سريع الدوران الراسي لديه أعلى قيمة نسبة التباين إلى الضوضاء 161.3203. وشركة فيليبس شركة فيليبس قيمة أعلى لنسبة الإشارة إلى الضوضاء للزمن

الثاني الموزون في صدى المجال السريع ، وهي 162.97 ديسيبل، وانتعاش الانعكاس المخفف بالسوائل ذو زمن صدى طويل لديه أعلى قيمة نسبة التباين إلى الضوضاء وهي 27.59 ديسيبل.

في الجسم الحي، تشير نتائج الدراسة إلى أنه عندما تم استخدام تتابع التصوير السريع باستخدام اكتساب الحالة الثابتة ثلاثي الابعاد، كان لدى شركة جي اي أفضل نسبة إشارة إلى ضوضاء، مع قيمة بلغت 11.206 ديسيبل. من ناحية أخرى، أنتج تتابع الزمن الثاني الموزون ل صدى الدوران السريع أعلى نتيجة لنسبة التباين إلى الضوضاء، بقياس 161.32 ديسيبل. مع نسبة نسبة الإشارة إلى الضوضاء بلغت 17.36 ديسيبل، و أنتج جهاز التصوير بالرنين المغناطيسي من شركة فيليبس أعلى تصنيف لنسبة الإشارة إلى الضوضاء عند استخدام تتابع الزمن الاول الموزون لصدى المجال السريع، وسجل التصوير السريع باستخدام اكتساب الحالة الثابتة أعلى قيمة لنسبة التباين إلى الضوضاء تبلغ 322.2625 ديسيبل.

خاتمة

تشير الدراسة إلى أنه يمكن استخدام التصوير بالرنين المغناطيسي عالي الدقة الزمن الثاني الموزون باستخدام التتابعات (التصوير السريع باستخدام اكتساب الحالة الثابتة, التوازن المدفوع, و التدخل البناء في الحالة المستقرة) لقياس العصب القوقعي، وهو أكثر سمكا في المرضى الذين لديهم نتائج إيجابية للتصوير بالرنين المغناطيسي. التصوير بالرنين المغناطيسي هو الفحص المفضل للتعرف على اضطرابات العصب الدهليزي، ومعظم الاضطرابات المشخصة تتطابق مع الخلل الدهليزي المركزي في نتائج اختبار. وجدت الدراسة أن التتابعات ذات نسبة الإشارة إلى الضوضاء ونسبة الإشارة إلى الضوضاء العالية في شركة فيليبس وشركة جي قدمت جودة صورة قابلة للمقارنة

وقدرات تشخيصية ممتازة. يعد فهم هذه التتابعات أمرًا بالغ الأهمية لتقييم نتائج اختبار الوظيفة الدهليزية والتمييز بين الاضطرابات الدهليزية. ويظل تصوير الرأرأة بالفيديو أداة حاسمة في التشخيص المسبب للمرضى الذين يشكون من الدوار، حتى خلال فترة ما بعد التصوير بالرنين المغناطيسي.

كانت التتابعات التي تحتوي على نسبة الإشارة إلى الضوضاء و نسبة التباين الى الضوضاء عالية في شركة فيليبس هي تتابع الزمن الاول الموزون لصدى المجال السريع التصوير السريع باستخدام اكتساب الحالة الثابتة على التوالي، ولكن في شركة جي اي كانت التتابع ات الأفضل للحصول على نسبة نسبة الإشارة إلى الضوضاء ونسبة التباين الى الضوضاء عالية هي التصوير السريع باستخدام اكتساب الحالة الثابتة ثلاثي الابعاد و الزمن الثاني الموزون لصدى التدور السريع وعلى التوالي.